Professional Report 125 v. 1.1

# $^{40}AR/^{39}AR$ AND U-PB GEOCHRONOLOGY OF CRETACEOUS–PALEOCENE IGNEOUS ROCKS AND CENOZOIC STRATA OF NORTHWESTERN COOK INLET, ALASKA: LINKAGES BETWEEN ARC MAGMATISM, COOLING, FAULTING, AND FOREARC SUBSIDENCE

Robert J. Gillis, Marwan A. Wartes, Trystan M. Herriott, David L. LePain, Jeff A. Benowitz, Alicja Wypych, Raymond A. Donelick, Paul B. O'Sullivan, and Paul W. Layer

Published by
STATE OF ALASKA
DEPARTMENT OF NATURAL RESOURCES
DIVISION OF GEOLOGICAL & GEOPHYSICAL SURVEYS
2022

**Cover.** One of the numerous thick, reworked tephra beds that characterizes the upper sub-unit of the West Foreland Formation (Twfu). Detrital zircon U-Pb maximum depositional ages of tephra beds analyzed from throughout most of the formation provide chronologic constraints for West Foreland deposition and deformation. View looking southeast down-dip toward the Cook Inlet from the Straight Creek area.

# $^{40}AR/^{39}AR$ AND U-PB GEOCHRONOLOGY OF CRETACEOUS–PALEOCENE IGNEOUS ROCKS AND CENOZOIC STRATA OF NORTHWESTERN COOK INLET, ALASKA: LINKAGES BETWEEN ARC MAGMATISM, COOLING, FAULTING, AND FOREARC SUBSIDENCE

Robert J. Gillis, Marwan A. Wartes, Trystan M. Herriott, David L. LePain, Jeff A. Benowitz, Alicja Wypych, Raymond A. Donelick, Paul B. O'Sullivan, and Paul W. Layer

Professional Report 125 v. 1.1

State of Alaska
Department of Natural Resources
Division of Geological & Geophysical Surveys

**STATE OF ALASKA**
Mike Dunleavy, Governor

**DEPARTMENT OF NATURAL RESOURCES**
Corri A. Feige, Commissioner

**DIVISION OF GEOLOGICAL & GEOPHYSICAL SURVEYS**
Steve Masterman, State Geologist and Director

Publications produced by the Division of Geological & Geophysical Surveys (DGGS) are available for free download from the DGGS website (dggs.alaska.gov). Publications on hard-copy or digital media can be examined or purchased in the Fairbanks office:

Alaska Division of Geological & Geophysical Surveys
3354 College Rd., Fairbanks, Alaska 99709-3707
Phone: (907) 451-5010 Fax (907) 451-5050
dggspubs@alaska.gov | dggs.alaska.gov

**DGGS publications are also available at:**
Alaska State Library,
Historical Collections & Talking Book Center
395 Whittier Street
Juneau, Alaska 99811

Alaska Resource Library and Information Services (ARLIS)
3150 C Street, Suite 100
Anchorage, Alaska 99503

**Suggested citation:**
Gillis, R.J., Wartes, M.A., Herriott, T.M., LePain, D.L., Benowitz, J.A., Wypych, Alicja, Donelick, R.A., O'Sullivan, P.B., and Layer, P.W., 2022, $^{40}Ar/^{39}Ar$ and U-Pb geochronology of Cretaceous-Paleocene igneous rocks and Cenozoic strata of northwestern Cook Inlet, Alaska: Linkages between arc magmatism, cooling, faulting, and forearc subsidence: Alaska Division of Geological & Geophysical Surveys Professional Report 125 v. 1.1, 78 p. https://doi.org/10.14509/30554

# Contents

# Figures

## Tables



## Appendices

Appendices are available to download in digital format from doi.org/10.14509/30554.

# $^{40}$AR/$^{39}$AR AND U-PB GEOCHRONOLOGY OF CRETACEOUS–PALEOCENE IGNEOUS ROCKS AND CENOZOIC STRATA OF NORTHWESTERN COOK INLET, ALASKA: LINKAGES BETWEEN ARC MAGMATISM, COOLING, FAULTING, AND FOREARC SUBSIDENCE

Robert J. Gillis[1], Marwan A. Wartes[1], Trystan M. Herriott[1], David L. LePain[1], Jeff A. Benowitz[2], Alicja Wypych[1], Raymond A. Donelick[3], Paul B. O'Sullivan[3,4], and Paul W. Layer[2,5]

## Abstract

This report presents results from 53 $^{40}$Ar/$^{39}$Ar and 51 U–Pb analyses of 73 sedimentary, intrusive, and volcanic rock samples collected in the south-central Tyonek Quadrangle of southern Alaska. These data provide new age control and provenance information for igneous and sedimentary rock units throughout the study area—some of which lack prior geochronologic age assignments. The samples were collected in concert with new geologic mapping of approximately 900 square miles encompassing parts of the Late Cretaceous–Paleogene magmatic arc and Cenozoic forearc basin in south-central Alaska. Detailed stratigraphic studies of the entire Cenozoic succession were undertaken at the same time. The widespread exposures of forearc strata in the map area are surface correlatives to hydrocarbon-hosting and commercially producing units in the adjacent subsurface of Cook Inlet basin to the southeast. The results inform structural and depositional models for the Cook Inlet forearc basin that are leveraged to assess tectonic events affecting the continental margin. Intrusive crystallization dates and geochemistry of igneous rocks define episodes of arc magmatism in the region at ca. 84–78 Ma, ca. 74–71 Ma, ca. 69–65 Ma, and ca. 62–57 Ma. Mafic and intermediate volcanics with arc to intra-plate signatures are restricted to a period of reduced arc magmatism from about 57 to 47 Ma. Bedrock cooling from approximately 550˚C to below 150˚C occurred monotonically, but at varying rates. The cooling trends are consistent with thermal conduction after shallow melt emplacement followed by structurally controlled cooling during the early Paleocene. New dates of reworked tephras from Cenozoic forearc strata constrain the depositional age of the West Foreland Formation at a maximum of ca. 47 Ma to ca. 38 Ma. The dates bracket renewed arc volcanism and middle Eocene syntectonic sedimentation at the western basin margin. More sparsely dated Tyonek and Beluga formations produced zircon U–Pb maximum depositional dates of ca. 15.3–15.2 Ma, and ca. 11.2–9.7 Ma, respectively. These dates are used to anchor a large existing palynologic dataset from the area. New and previously published palynologic results indicate that the oldest Hemlock Conglomerate extends to middle Eocene and thus is partially contemporaneous with West Foreland deposition. Sediment accumulation rates calculated from dated stratigraphic intervals and revised stratigraphic age ranges of the West Foreland Formation and Hemlock Conglomerate suggest a pronounced decrease in basin subsidence during Hemlock deposition followed by an order of magnitude increase in sediment accumulation rates by the middle Miocene. Conglomerate clast dates and

[1]Alaska Division of Geological & Geophysical Surveys, 3354 College Rd., Fairbanks, Alaska 99709-3707.
[2]Geophysical Institute and Geochronology Laboratory, University of Alaska Fairbanks, Fairbanks, AK 99775
[3]Apatite to Zircon, INc., 1075 Matson Road, Viola, Idaho 83872
[4]GeoSep Services, 1521 Pine Cone Road, Moscow, ID 83843
[5]College of Natural Sciences and Mathematics, University of Alaska Fairbanks, PO Box 755940, Fairbanks, AK 99775

detrital grains from reworked tephras provide additional insights into sediment provenance that help refine a depositional model for the Paleogene basin margin. The results highlight the transition from high-gradient, small-catchment alluvial systems sourced from the structurally exhumed arc to a mature, trunk fluvial network distributing a mixed sediment load from proximal arc and distal basement sources during a period of low basin accommodation. Dextral faults extending for nearly 250 km from the upper Cook Inlet to the Matanuska Valley constituted a linked structural system from late Paleocene to middle Eocene that created transtensional depocenters at major fault step-overs along the northwestern and northern margins of the forearc basin. Orogen-parallel extension of the arc region directly to the north is a mechanical consequence of an eastward increase in strike-slip displacement along the fault system. The resulting normal faults produced conduits for magmas sourced from a depleted mantle reservoir during a lull in arc magmatism, and likely facilitated subsidence in the Susitna successor basin. Paleocene to Eocene initiation of dextral strike-slip faults and extension of the arc region supports models for Paleogene oroclinal bending of Alaska.

## INTRODUCTION

The Cook Inlet forearc basin (CIB) is the second largest petroleum province in Alaska and the principal source of natural gas to the most populous region of the state—having produced nearly 8.0 trillion cubic feet of gas and 1.3 billion barrels of oil since production began in 1961 (Stanley and others, 2011). Many of the hydrocarbon fields are offshore, and much of what is understood about the producing stratigraphy and structural traps comes from subsurface data. Only a small fraction of these data has found its way into the public domain. The western margin of upper Cook Inlet (fig. 1) is the only location in the basin where all the stratigraphic units that compose the petroliferous Cenozoic succession (fig. 2) are exposed together at the surface. The strata are cut by regional-scale faults that often juxtapose the Cenozoic forearc basin fill against arc intrusive and extrusive rocks (fig. 3). Therefore, the region is important for understanding the stratigraphic architecture, structural framework, and Cenozoic evolution of the basin margin. This report presents 104 new geochronologic dates (tables 1–3) from intrusive, extrusive, and clastic sedimentary rocks exposed at the northwestern basin margin that refine the igneous, structural, and depositional history of the area.

Although this region of the basin margin has been the focus of several geologic studies since the 1960s (e.g., Barnes, 1966; Adkison and others, 1975a; Flores and others, 1994), many facets of the stratigraphic and structural systems remain poorly resolved. For instance, early mapping was hindered by a nascent understanding of the Cenozoic stratigraphy. Extensive Quaternary cover and dense vegetation often obscure stratigraphic and structural relations in all but a few large drainages (e.g., Barnes, 1966; Detterman and others, 1976a; Magoon and others, 1976). Inadequate stratigraphic age control and subsurface type sections defined in wells near the basin axis (Calderwood and Fackler, 1972) continue to result in disagreement about the identity of litho-

**Figure 1, page 3. A.** Regional geologic map of the upper Cook Inlet forearc adapted from Wilson and others (2012), highlighting geologic and physiographic features discussed in the text. Jurassic–Paleocene granitoids of the Neacola and Tordrillo mountains that compose part of the western Alaska Range, and Talkeetna Mountains to the northwest of the Cook Inlet forearc basin together form the exhumed roots of Cenozoic and older magmatic arcs. Jurassic—Cretaceous strata of the Kenai–Chugach Mountains represent shortened and uplifted marine rocks of the accretionary wedge that bracket the forearc basin to the east. The distribution and extent of structures on the northwestern periphery of the basin represent new interpretations from recent geologic bedrock and subsurface mapping. **B.** Schematic cross section of the upper Cook Inlet area modified from Trop and Ridgway (2007) depicting the tectonic elements and terrane associations of the forearc. CGF=Capps Glacier fault, LCF=Lake Clark fault, MGS-M=Middle Ground Shoal-Moquawkie structural trend, BRFS=Border Ranges fault system, CF=Contact fault.

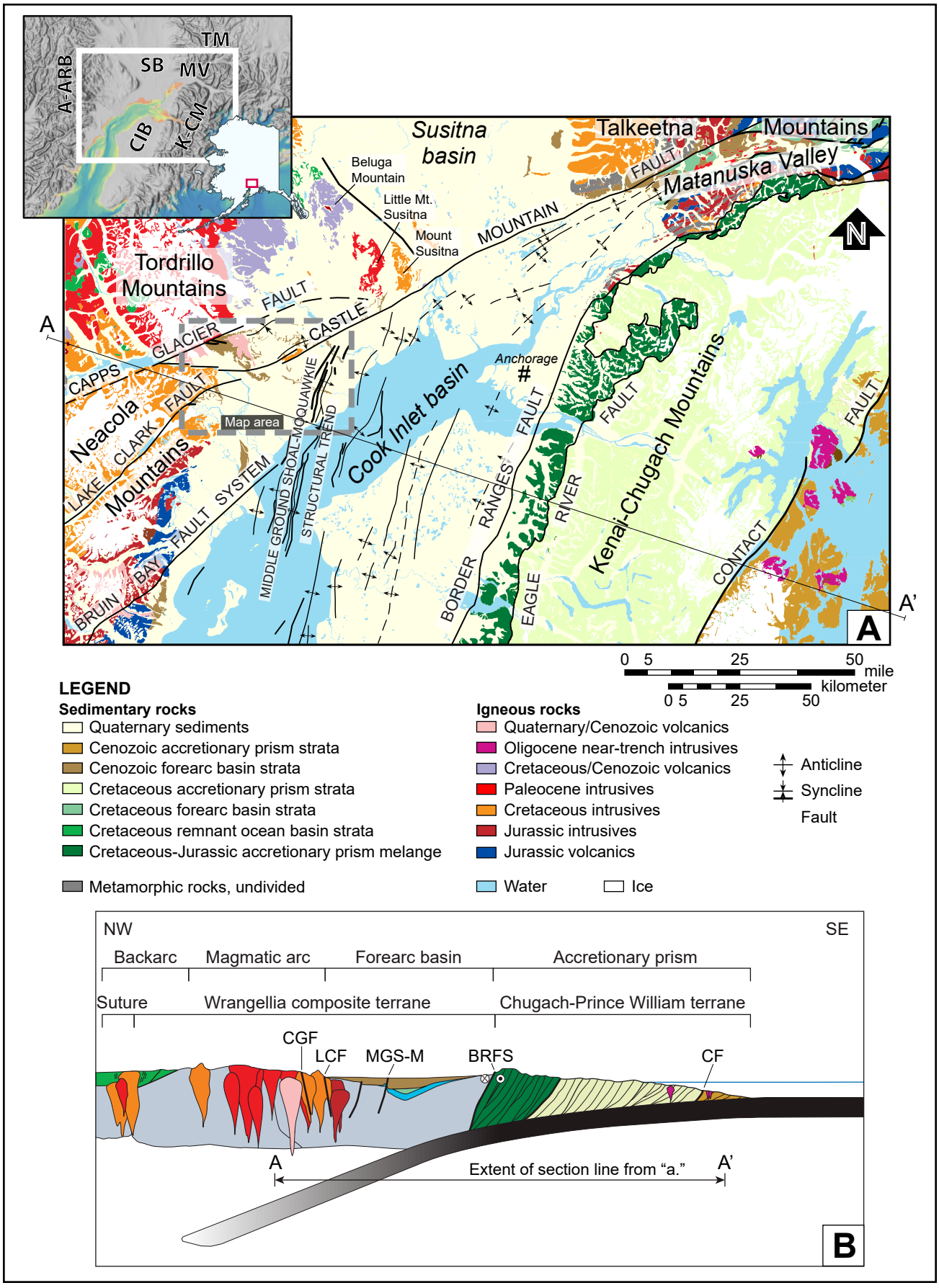
TM
SB
MV
A-ARB
CIB
K-CM
Susitna basin
Talkeetna Mountains
FAULT
Matanuska Valley
Beluga Mountain
Little Mt. Susitna
Mount Susitna
MOUNTAIN
N
Tordrillo Mountains
FAULT
CASTLE
GLACIER
A
CAPPS
FAULT
Neacola Mountains
CLARK
LAKE
FAULT SYSTEM
Map area
MIDDLE GROUND SHOAL-MOQUAWKIE
STRUCTURAL TREND
Cook Inlet basin
Anchorage
#
FAULT
RANGES
RIVER
BORDER
EAGLE
FAULT
Kenai-Chugach Mountains
FAULT
CONTACT
BRUIN BAY FAULT
A'
A
0 5 25 50 mile
0 5 25 50 kilometer
LEGEND
Sedimentary rocks
Quaternary sediments
Cenozoic accretionary prism strata
Cenozoic forearc basin strata
Cretaceous accretionary prism strata
Cretaceous forearc basin strata
Cretaceous remnant ocean basin strata
Cretaceous-Jurassic accretionary prism melange
Metamorphic rocks, undivided
Igneous rocks
Quaternary/Cenozoic volcanics
Oligocene near-trench intrusives
Cretaceous/Cenozoic volcanics
Paleocene intrusives
Cretaceous intrusives
Jurassic intrusives
Jurassic volcanics
Water
Ice
Anticline
Syncline
Fault
NW
SE
Backarc
Magmatic arc
Forearc basin
Accretionary prism
Suture
Wrangellia composite terrane
Chugach-Prince William terrane
CGF
LCF
MGS-M
BRFS
CF
A
Extent of section line from "a."
A'
B

stratigraphic units exposed near the basin margin (e.g., Adkison and others, 1975a; Detterman and others, 1976a; Magoon and others, 1976; Wilson and others, 2012).

Age constraints for the Cenozoic stratigraphy are based principally on paleobotanical assemblages (e.g., Wolfe and others, 1966; Adkison and others, 1975a, 1975b; Wolfe and Tanai, 1980; Reinink-Smith and Leopold, 2005) and often proprietary palynomorph assemblages in wells (e.g., Atlantic Richfield Company [ARCO], unpublished data; Zippi palynology database, unpublished). Therefore, this stratigraphy is most commonly considered in terms of chronostratigraphic units defined by privately held biostratigraphic data (fig. 2). More recently, a large palynology dataset from the western Cook Inlet and Kenai Peninsula (Zippi and Loveland, 2012; Zippi and others, 2021) and geochronologic datasets from outcrop samples collected from both sides of the basin (Dallegge and Layer, 2004; Haeussler and others, 2009; Finzel and others, 2015, 2016; Finzel and Enkelmann, 2017), have improved lithostratigraphic age constraints at the basin margins.

The Alaska Division of Geological & Geophysical Surveys (DGGS), in collaboration with the Alaska Division of Oil and Gas (DOG), carried out approximately 900 square miles of new 1:63,360-scale geologic mapping in the south-central Tyonek Quadrangle in an effort to address these challenges and construct more robust linkages between the surface geology exposed on the northwestern margin and producing regions of the basin. This geologic mapping aimed to refine or revise the stratigraphic and structural framework of the region (Gillis and others, in preparation). Related topical studies, including detailed analyses of the stratigraphy and sediment composition (see LePain and others, 2013; Helmold and others, 2018) were also conducted in locations that enhanced the understanding of the regional geology. This geochronologic report is a companion to the new bedrock geologic mapping to be presented in Gillis and others (in preparation) and in preliminary poster form by Gillis and others (2017) (see fig. 4 for a simplified representation). The integration of these data with geologic mapping, basin analysis, and existing geochronologic and biostratigraphic datasets provides new insights about early basin subsidence with respect to developing structures; spatial and temporal relationships of mappable stratigraphic units along the basin margin; and episodes of arc plutonism, volcanism, and subsequent bedrock cooling.

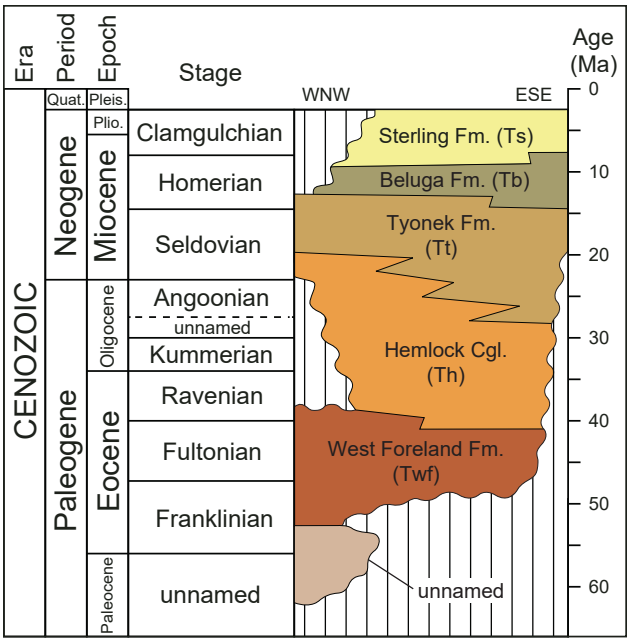


**Figure 2.** Chronostratigraphic chart for the upper Cook Inlet basin (adapted from Swenson, 2001; Helmold and others, 2018), which is based principally on proprietary industry data. The "Unnamed" Paleocene—Eocene unit has not been identified in outcrop but has been picked as Chickaloon Formation in some wells (American Stratigraphic Company, unpublished) based on undisclosed criteria.

## GEOLOGIC OVERVIEW

Cook Inlet estuary overlies an Early Jurassic to modern forearc basin situated above the presently subducting Pacific plate and completes a classic forearc trinity (e.g., Dickinson, 1995) that includes the magmatic arc to the northwest and accretionary prism to the southeast (fig. 1B). Inboard of the forearc basin, intrusive and extrusive rocks record multiple partially to largely superposed episodes of arc magmatism that range in age from Late Triassic/Early Jurassic to modern and constitute the Alaska and Aleutian

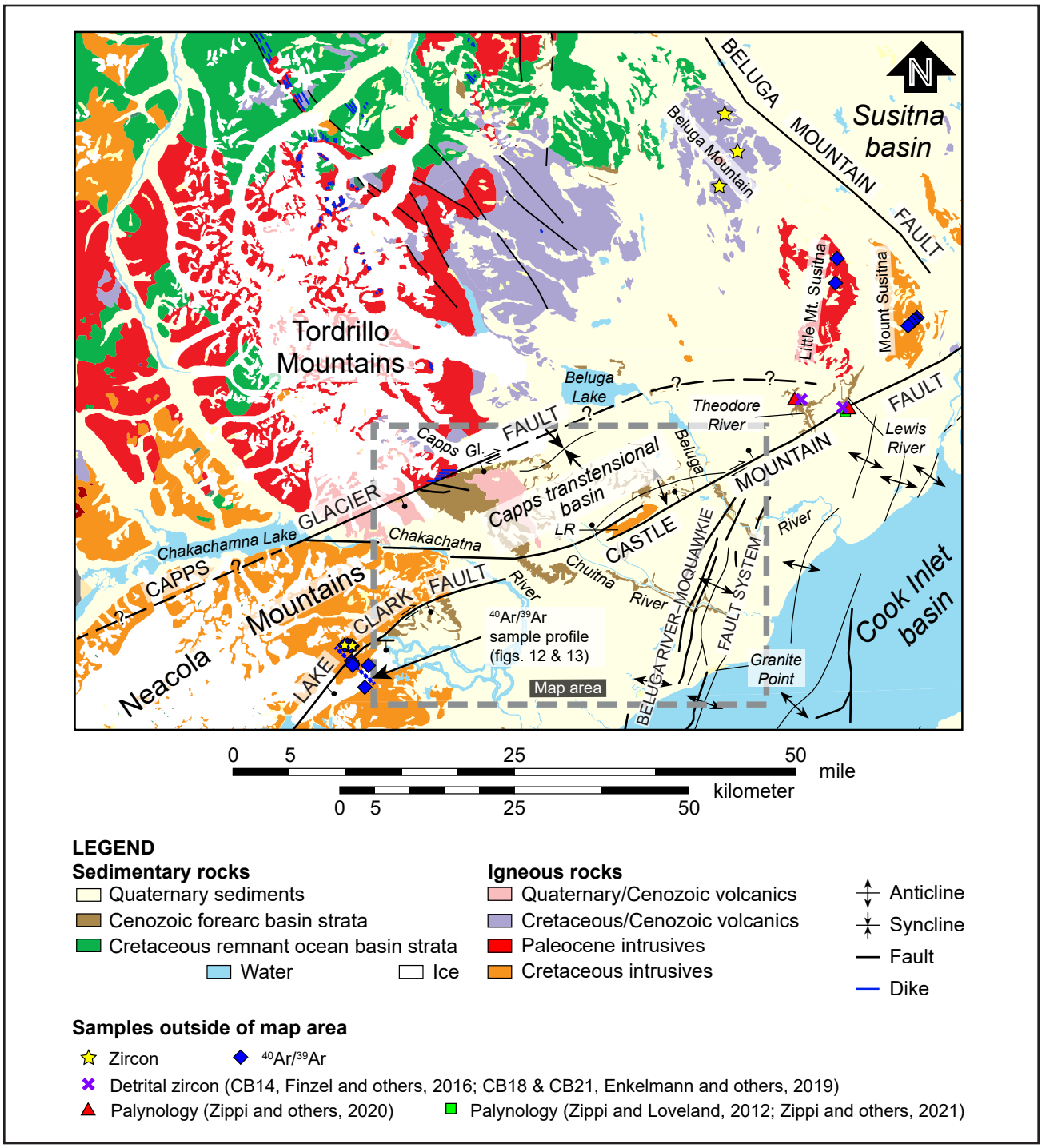


**Figure 3.** Geologic map of greater study area with respect to new geologic mapping (gray dashed box), highlighting major structures that deform the arc-forearc margin, and showing sample locations outside of the map area. LR = Lone Ridge.

Ranges (fig. 1; the Alaska–Aleutian Range batholith of Reed and Lanphere (1973). Trenchward of the basin is the large emergent accretionary prism that forms the Chugach and Kenai Mountains (Chugach-Prince William terrane; fig. 1). The forearc basin and magmatic arcs are constructed on Wrangellia composite terrane crust (fig. 1B) that progressively accreted from east to west against continental North America during the Late Jurassic/Early Cretaceous to Late Cretaceous closure of a remnant ocean basin

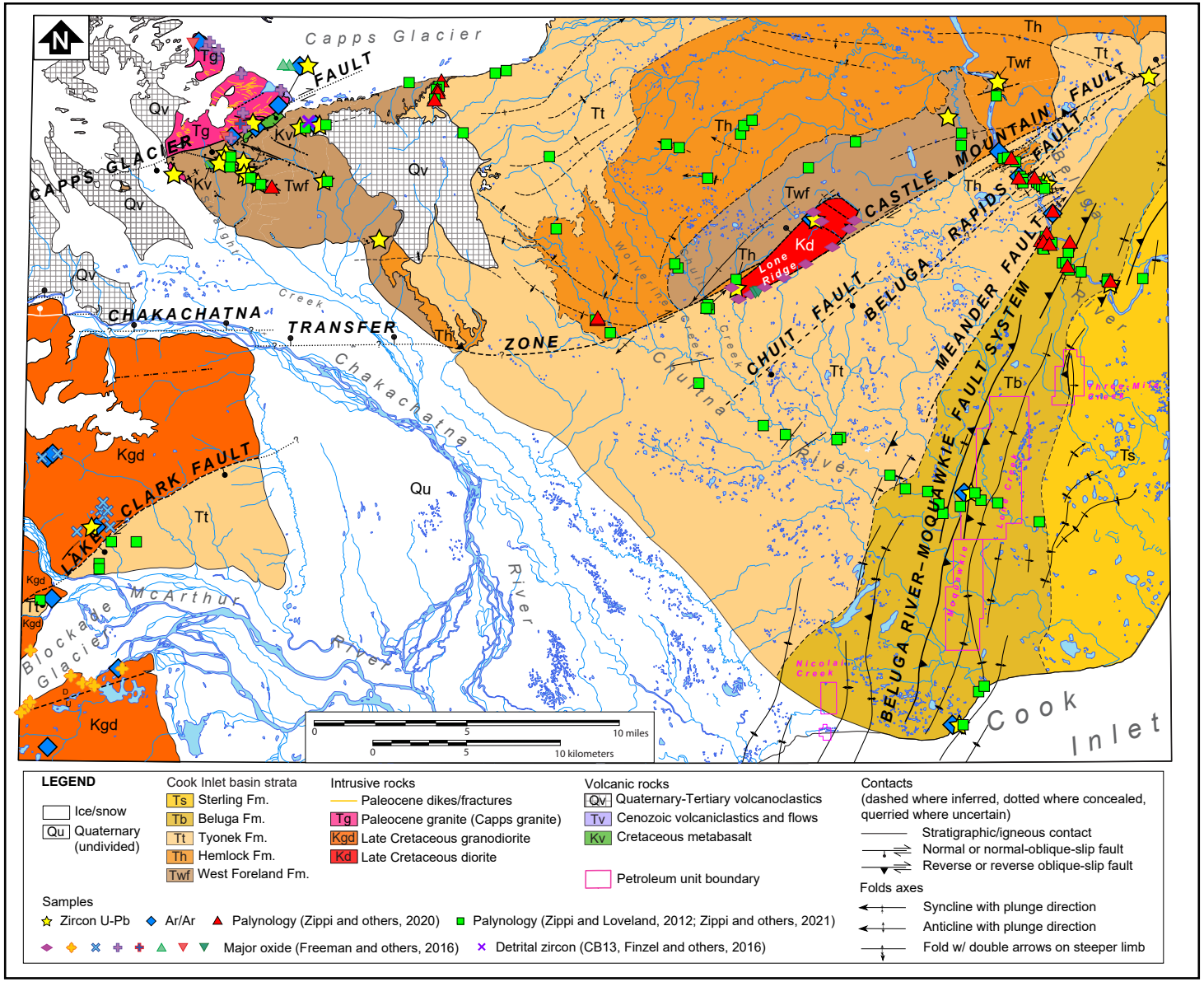


**Figure 4.** Simplified geologic map of the south-central Tyonek Quadrangle (simplified from Gillis and others, in preparation) highlighting sample locations for zircon U-Pb (yellow stars), $^{40}Ar/^{39}Ar$ (blue diamonds), and palynology (red triangles [Zippi and others, 2021], green squares [Zippi and Loveland, 2012]) analyses. Refer to appendix J for major oxide sample numbers, locations and descriptions. Refer to figures 11 and 12 for explanation of major oxide classification symbols. See figures 1 and 2 for map area location.

(Ridgway and other, 2002; Hampton and others, 2010). The Cook Inlet forearc basin contains over 10,700 m of chiefly marine Mesozoic strata and an additional 7,600 m of dominantly terrestrial Cenozoic clastic rocks (Calderwood and Fackler, 1972; Kirschner and Lyon, 1973; Boss and others, 1976; LePain and others, 2013). An abrupt change from marine to terrestrial deposition is marked by a widespread angular unconformity near the basin margins that separates Mesozoic from Cenozoic rocks and exposes tilted Jurassic volcanic arc and forearc basin strata (Detterman and Hartsock, 1966; Boss and others, 1976; Magoon and Claypool, 1981; Trop, 2008; Shellenbaum and others, 2010; Gregersen and Shellenbaum, 2016). Reinitiation of CIB subsidence during the Paleocene(?) commenced at modest rates that appear to have episodically increased through the Pliocene (Finzel and others, 2011), with local intra-basin unconformities separating some units (Calderwood and Fackler, 1972; Boss and others, 1976; Swenson, 2001; LePain and others, 2013). These Cenozoic nonmarine rocks are currently the most economically important in the basin, as they host nearly all commercial oil reservoirs and all gas reservoirs (Stanley and others, 2011). The Cenozoic stratigraphy also includes abundant coal seams that are the chief source of biogenic gas produced in upper Cook Inlet fields (Claypool and others, 1980). Cenozoic alluvial and fluvial strata filling the basin are thought to be time-transgressive (Swenson, 2001), recording erosional unroofing of the Early Jurassic to Paleocene magmatic arcs (Kirschner and Lyon, 1973; Hudson, 1986; Helmold and others, 2018), with sediment contributions from distal metamorphic basement terranes and the accretionary prism after the middle to late Paleogene (Kirschner and Lyon, 1973; Rawlinson, 1984; Finzel and others, 2015; 2016; Finzel and Enkelmann, 2017; Helmold and others, 2018).

## Cook Inlet Forearc Basin Structure

The forearc domains of Cook Inlet are separated by regional-scale oblique-slip faults that often define the physiographic boundaries of the basin (figs. 1 and 3), but their role in controlling long-term basin subsidence remains poorly resolved. To the southeast of the CIB and south of the Matanuska Valley, the Border Ranges fault system (BRFS; Pavlis, 1982; Pavlis and Roeske, 2007) separates an emergent accretionary wedge composed of Jurassic through Eocene strata from the Mesozoic and Cenozoic forearc basin. Dextral slip estimates for the fault system based on potential piercing points and sediment provenance range from about 600 to as much as 2,000 km, ostensibly transporting the accretionary prism from a position as distant as southern Vancouver Island since the Late Cretaceous (Cowan, 2003; Roeske and others, 2003). A recent controversial model based on the interpretation of detrital zircon results raises the possibility for up to 3,200 km of dextral transport (Garver and Davidson, 2015). Motion along known segments of the fault system ceased by approximately 50 Ma (Haeussler and others, 2003; Roeske and others, 2003), although Cowan (2003) and Garver and Davidson (2015) speculate that lateral transport of the prism along unidentified strands may have continued through the Paleogene.

## Northwest Side of the Basin

The northwest side of the forearc basin is structurally separated from the Jurassic through Paleocene arcs by the Bruin Bay fault system (BBFS) and Castle Mountain, Lake Clark, and Capps Glacier faults (figs. 1 and 3). The sinistral, transpressional BBFS separates the Jurassic arc from its forearc basin for up to 450 km from the upper Alaska Peninsula to upper Cook Inlet (Detterman and Hartsock, 1966; Magoon and others, 1976). Estimates of sinistral displacement on the fault system range from less than 19 km to 65 km, with 3 to 5 km of reverse throw (Detterman and Hartsock, 1966; Detterman and Reed, 1980; Betka and others, 2017). Recent work demonstrates that the Bruin Bay and associated faults had a polyphase slip history. Notably, despite the longevity of the forearc and juxtaposition of Jurassic arc and forearc strata across the fault system, most activity along this structure may have coincided with renewed forearc subsidence during the Paleogene (Betka

and others, 2017).

The northern and northwestern structural boundaries of the basin are complex and defined by several discontinuous oblique-slip faults, including the Castle Mountain, Lake Clark, and Capps Glacier faults (figs. 1 and 3; Magoon and others, 1976; Gillis and others, 2017). These faults are widely considered to be dextral transpressional (Detterman and others, 1976a, 1976b; Magoon and others, 1976; Trop and others, 2003; Gillis and others, 2009). This region is unique, as it is the only location along the margin where the forearc basin steps arc-ward of the BBFS (e.g., Magoon and others, 1976). A principal structure in upper Cook Inlet is the Castle Mountain fault (CMF; figs. 1 and 3), which may have offset the Jurassic arc and BBFS right-laterally by as much as 130 km since Late Jurassic to the Paleogene (Hackett, 1976; Trop and others, 2005). The CMF is best expressed as the structural boundary between the Talkeetna Mountains and exhumed Matanuska segment of the forearc basin to the northeast of upper Cook Inlet (fig. 1A). In that area, bedrock cross-cutting relations indicate that its motion was mainly dextral strike-slip from perhaps the Late Cretaceous until the late Oligocene or early Miocene (Grantz, 1965). Most contraction on the CMF occurred after the early Miocene, resulting in an estimated 1.5 to nearly 5 km of throw (Grantz, 1965; Detterman and others, 1976b; Fuchs, 1980; Bruhn and Pavlis, 1981; Fuchs, 2019; Terhune and others, 2019). The CMF is transpressional in the Holocene, with minimum estimates of dextral slip at 0.3–3.0 mm/yr (Detterman and others, 1974; Bruhn, 1978; Haeussler and others, 2002; Willis and others, 2007; Koehler and others, 2012). However, there has been no discernable Holocene activity on the CMF southwest of Mount Susitna (figs. 1 and 3). Although a prominent fault scarp defines the southeast edge of the Lone Ridge diorite (fig. 4), the fault does not appear to cut the surrounding upper Pleistocene glacial deposits (Schmoll and Yelle, 1987; Koehler and Reger, 2011). Thus, it was proposed that Quaternary slip along the CMF is instead transferred to north-northeast striking prospective folds in the Cook Inlet subsurface (Haeussler and others, 2000; Haeussler and Saltus, 2011). The Lake Clark fault (LCF) has long been considered the southwestward continuation of the CMF (figs. 1 and 3; e.g., Grantz, 1966; Haeussler and Saltus, 2011), but with a maximum lateral slip magnitude no greater than 5 to 26 km and with little to 1000 m of reverse throw since the Oligocene (Ivanhoe, 1962; Plafker and others, 1975; Detterman and others, 1976a; Haeussler and Saltus, 2005). The LCF has been arbitrarily mapped as the CMF northeast of the Beluga River where the Bruin Bay fault intersects the structure (Detterman and others, 1976a; Magoon and others, 1976); new inch-to-mile mapping conducted as part of a broad study that includes this report instead interprets them as two distinct structures (figs. 3 and 4; Gillis and others, 2017; in preparation). Reconnaissance structural investigations along the LCF suggest a complicated slip history that records both transpression and transtension (Caine and others, 2017).

The northernmost and least studied basin margin structure is the Capps Glacier fault (CGF; figs. 3 and 4). Early reconnaissance work cited similarities to the nearby LCF and a probable dextral-reverse slip history for the structure (Gillis and others, 2009). However, a more recent and thorough study of this region of the forearc basin indicates that the northern embayment of the basin was controlled by extensional and transtensional tectonics during the Paleogene followed by post-Oligocene dextral reverse reactivation (Gillis and others, 2017; in preparation). The magnitude of dextral slip on the CGF is poorly resolved but is limited by the approximately 40 km length of the sub-basin at the step-over between the CGF and the dextral CMF to the southeast (figs. 3 and 4).

## Westside Cenozoic Stratigraphy and Age Constraints

The Cenozoic basin fill in upper Cook Inlet includes the West Foreland Formation, Hemlock Conglomerate, Tyonek Formation, Beluga Formation, and Sterling Formation (fig. 2). These five units constitute the Kenai Group as defined by

Calderwood and Fackler (1972). Boss and others (1976) redefined the Kenai Group to include only the latter four formations based in part on the presence of thick coals and paucity of volcanogenic material; the West Foreland generally lacks significant coal and is characterized by abundant tephras, bentonite, and volcaniclastic intervals (Boss and others, 1976; Wolfe and Tanai, 1980; LePain and others, 2013). An un-named Paleocene terrestrial unit is penetrated locally in some Cook Inlet and Susitna basin wells (Swenson and others, 2001; LePain and others, 2013; Stanley and others, 2013) and may be correlative to outcrops in the Talkeetna Mountains and Matanuska Valley to the northwest and west, respectively (Trop and Ridgway, 1999; Donaghy, 2012; Kortyna and others, 2013; Sunderlin and others, 2014). Stratigraphic age constraints on individual units are generally poor and are principally defined by plant macrofossils (Wolfe and others, 1966; Wolfe and Tanai, 1980). Often these age constraints are based on unpublished proprietary palynologic datasets. However, some geochronologic age control is available in the central and eastern parts of the basin on the Kenai Peninsula (Triplehorn and others, 1977; Turner and others, 1980; Dallegge and Layer, 2004) and on the west side between Capps Glacier and the Cook Inlet coast (Finzel and others, 2015, 2016; Finzel and Enkelmann, 2017; Enkelmann and others, 2019). The entire succession is generally considered to be Eocene to Pliocene (Swenson, 2001; Zippi and Loveland, 2012; Zippi palynology dataset, unpublished). Subsidence marked by West Foreland deposition is proposed to have begun in late Paleocene (Magoon and others, 1976 [based on unpublished data from J.A. Wolfe]) through middle Eocene (Finzel and others, 2016). The following discussion briefly summarizes key characteristics of each of the Cenozoic units prior to presenting the new age data.

### West Foreland Formation (Twf)

The West Foreland Formation in outcrop on the northwest side of the basin is cut by the CGF (fig 4; Gillis and others, 2017). Stratigraphic thickening with respect to structures and strata that bury fault tips indicate that deformation along this part of the margin was concurrent with West Foreland deposition (Gillis and others, 2017). Nearly the entire approximately 1000 m-thick West Foreland succession is exposed between Straight Creek and Capps Glacier (fig 4), with mappable lithofacies that allow subdivision into informal lower, middle, and upper subunits (fig. 5; LePain and others, 2013). The lower West Foreland is dominated by conglomerate composed chiefly of volcanic clasts but lacks primary volcanic strata. However, the abundance of poorly sorted volcaniclastic sandstone and reworked tephras increases up-section, making the middle and upper subunits amenable to detailed geochronologic work. Lithofacies associations suggest a proximal alluvial fan setting that evolved to distal fan deposition in a structurally subsiding basin (LePain and others, 2013). The lower subunit rests unconformably on Late Cretaceous metabasalt, and locally on late Paleocene granite between Capps Glacier and Straight Creek (fig. 4). The upper West Foreland Formation is gradationally or unconformably overlain by a very thin (less than 10 m) Hemlock Conglomerate near Capps Glacier, and a relatively thick succession (several hundred meters) near Lone Ridge (fig. 4). Early age assignments based on sparse paleobotany and a single palynologic sample placed the age of the West Foreland Formation as Paleocene to Eocene. More recent zircon U–Pb data for the West Foreland Formation indicate a middle Eocene age based on one unpublished ca. 43 Ma age (no uncertainty provided) from a tephra collected near Capps Glacier (Haeussler and others, 2013) and a single 44.2 ± 0.8 Ma grain age (1σ error) from a nearby detrital sample (Finzel and others, 2016).

### Hemlock Conglomerate (Th)

The Hemlock Conglomerate is commonly believed to be absent at the surface in upper Cook Inlet (Adkison and others, 1975a; Magoon and others, 1976), although Boss and others (1976) and Wolfe and Tanai (1980) suggest that throughout the basin the Hemlock Conglomerate might simply represent a conglomeratic unit that composes the

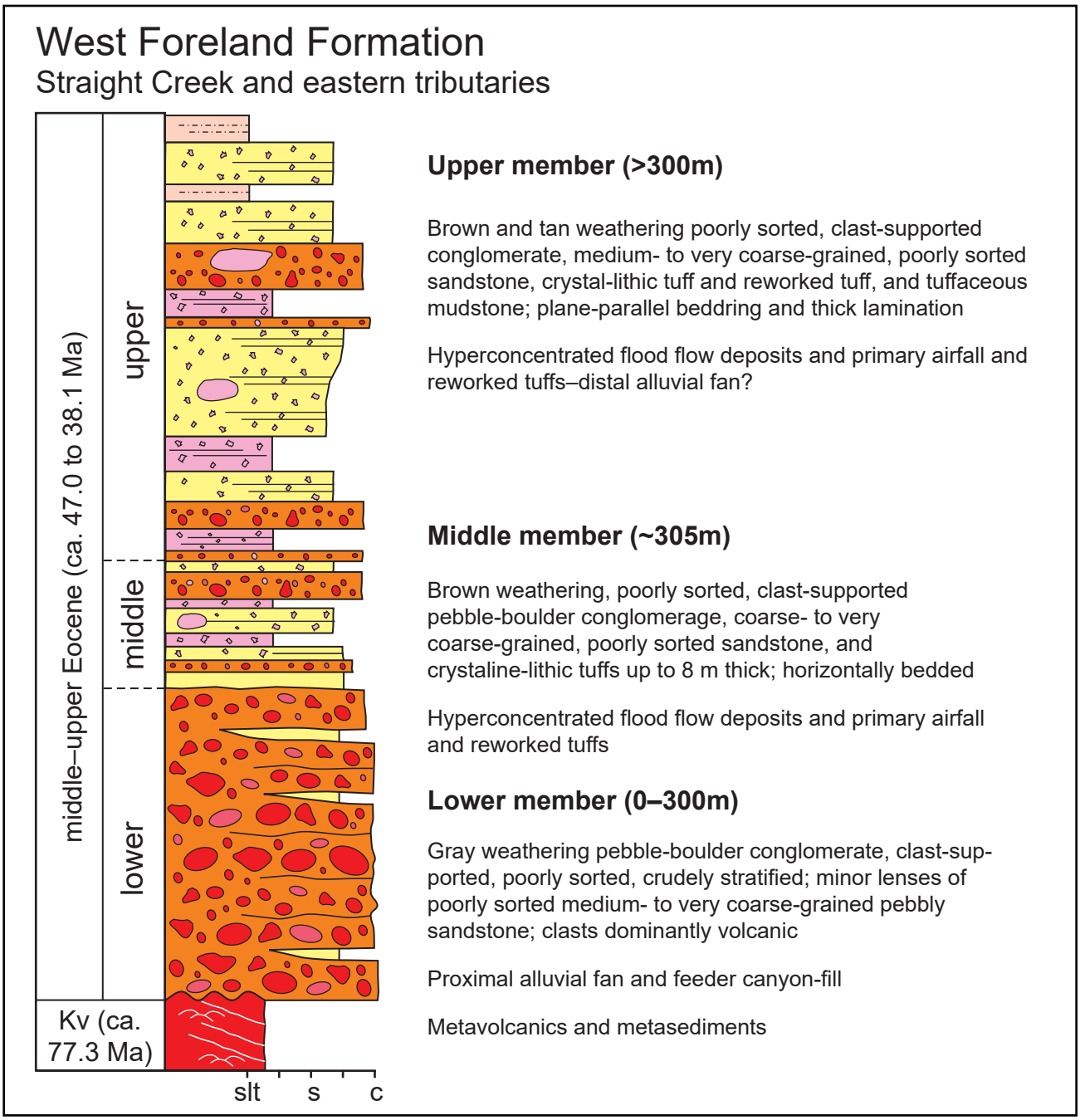


**Figure 5.** Composite summary of the West Foreland Formation in the vicinity of Straight Creek and Capps Glacier, Tyonek Quadrangle, based on bedrock geologic mapping and detailed stratigraphic studies by the authors. Three informal members are recognized based on lithofacies and the presence/absence of reworked and primary tephras.

basal part of the Tyonek Formation. Results of recent stratigraphic studies (LePain and others, 2013) and geologic mapping (Gillis and others, 2017; in preparation) on the west side of the basin indicate that rocks with Hemlock-like facies as described by Calderwood and Fackler (1972) are exposed as a mappable belt of discontinuous outcrops for over 40 km from the Chuitna River in the west to Mount Susitna in the east (fig. 3). We therefore recognize these strata as Hemlock Conglomerate. A complete, but intermittently exposed succession of these rocks occurs north of the Castle Mountain fault in apparent

stratigraphic conformity between West Foreland and Tyonek strata (fig. 4). The unit is compositionally and texturally mature, composed principally of well-rounded quartzose conglomerate, subordinate quartzofeldspathic cross-stratified pebbly sandstone, and minor carbonaceous and coaly mudstone that are interpreted to record braided fluvial deposition in a low-accommodation setting (LePain and others, 2013). Age constraints for the Hemlock Conglomerate are chiefly derived from plant macrofossil assemblages (Wolfe and others, 1966), micropaleontologic results (Zippi and Loveland, 2012; Zippi and others, 2021; Finzel and others, 2016), and three detrital zircon maximum depositional ages (MDAs; Finzel and others, 2016; Enkelmann and others, 2019). Interpreting the biostratigraphic constraints within the framework of the new geologic mapping of Gillis and others (in preparation) indicates that Hemlock strata are time transgressive. The youngest Hemlock ages in the field area occur between Capps Glacier and Lone Ridge (fig. 4) where they range from Late Oligocene to Early Miocene, and possibly as young as middle Miocene. The uncertainty about the middle Miocene age stems from our difficulties distinguishing between Hemlock and transitional conglomeratic lower Tyonek Formation (see Adkison and others, 1975a) in the field area. Ages become progressively older in outcrop away from the margin and along strike to the northeast from late Eocene–Early Oligocene on the Beluga River north of the CMF (fig. 4), to middle–late Eocene south of the CMF, to middle Eocene in the Theodore and Lewis river drainages (fig. 3). Thus, Hemlock sedimentation may have been partially contemporaneous with the underlying West Foreland Formation and overlying Tyonek Formation (as suggested by Swenson, 2001). Hemlock ages may again become younger offshore approaching the basin axis. Recent zircon U–Pb data from outcrop and upper Cook Inlet wells (Finzel and others, 2015, 2016; Enkelmann and others, 2019) provide the first geochronologic maximum depositional ages for the Hemlock Conglomerate of 27.0 ± 0.5 Ma (n=1 grain, 1σ uncertainty) on the northwest side of the basin and 25.9 ± 0.3 Ma (weighted mean age, n=7 grain, 1σ uncertainty) at the basin axis. These ages are consistent with its proposed biostratigraphic age range.

### Tyonek Formation (Tt)

The Tyonek Formation north of the CMF between Capps Glacier and Lone Ridge occurs as an incomplete, weakly deformed, and poorly exposed succession (fig. 4). An apparently gradational depositional contact with the Hemlock Conglomerate is preserved north and west of Lone Ridge. The formation is better characterized south of the Castle Mountain fault from shallow well cores and discontinuous outcrops adjacent to the Chuitna River (Flores and others, 1994), but is perhaps most continuously exposed along the Beluga River (fig. 4). There, the succession is incomplete and truncated by faults that place it against Hemlock Conglomerate, West Foreland, and Beluga formations at different locations along the drainage (Gillis and others, in preparation). At two Beluga River locations, the base of the Tyonek Formation is in angular unconformity with gently south-dipping Hemlock Conglomerate and moderately north-dipping West Foreland Formation. The stratigraphic contact with the overlaying Beluga Formation is not observed in outcrop on the west side of the basin, but elsewhere this transition is considered gradational (Calderwood and Fackler, 1972). In locations north and south of the Castle Mountain fault (fig. 4), Tyonek strata are characterized by thick, tabular, cross-stratified sandstone and siltstone that compositionally resemble Hemlock Conglomerate, but with intercalated mudrock and common coal beds up to 18 m thick. The Tyonek Formation is interpreted to record low-gradient braided fluvial and floodplain deposition in a high-accommodation setting (LePain and others, 2013). Although discontinuously exposed along the upper Chuitna River, Chuit Creek, and Wolverine Creek (fig. 4), quartzose pebble conglomerates and sandstones of the Hemlock Conglomerate appear to transition into compositionally similar sandstones with increasingly common mudrock and coal that characterize the Tyonek Formation. Palynologic data from these outcrops document strata that decrease in

age to the northwest from middle Eocene to middle Miocene with no apparent discontinuity in age calls (Zippi and Loveland, 2012; Zippi and others, 2021). Tyonek outcrops near Capps Glacier (fig. 4) are the type section for the early to middle Miocene Seldovian floral stage (Wolfe and others, 1966; Wolfe and Tanai, 1980), although in lower Cook Inlet the age of the strata is believed to extend down into the Angoonian stage (early–late Oligocene; Wolfe and others, 1966; Wolfe and Tanai, 1980). Recent micropaleontologic results (Zippi and Loveland, 2012; Zippi and others, 2021)—from some of the same outcrops where Wolfe and others (1966) collected plant megafossils used to define the Seldovian floral assemblage—and results from recent geologic mapping (Gillis and others, in preparation) produce age interpretations ranging from early Miocene to late Miocene, although they generally bracket the age of Tyonek strata exposed on the west side of the basin between early–middle and late–middle Miocene. In the Lewis River drainage (fig. 3), quartzose sandstones mapped as Tyonek Formation by Magoon and others (1976) yield micropaleontologic and detrital zircon maximum stratigraphic ages that suggest late Eocene deposition (Enkelmann and others, 2019; Zippi and others, 2021).

### Beluga Formation (Tb)

On the west side of Cook Inlet basin, the Beluga Formation only crops out along the Chuitna and Beluga Rivers (fig. 4). Where best exposed along the Beluga River, it is in fault contact with the underlying Tyonek Formation, and the gradational contact with overlaying Sterling Formation is well exposed at a prominent bend in the river (fig. 4; Gillis and others, in preparation). Beluga strata are composed principally of poorly consolidated clayey siltstone, lignitic coal, and thin-bedded argillaceous sandstone with less common thick, lenticular sandstone bodies. These strata are interpreted to record deposition in an anastomosing fluvial system in a high-accommodation environment (Mongrain, 2012; LePain and others, 2013). On the east side of Cook Inlet, several K-Ar, $^{40}$Ar-$^{39}$Ar, and zircon fission-track dates (Triplehorn and others, 1977; Dallegge and Layer, 2004; Turner and others, 1980, respectively) constrain deposition of the unit near the axis of the basin from ca. 11.3 to 8.8 Ma. Recently published detrital zircon U–Pb results from Beluga Formation strata along the Chuitna and Beluga rivers produce youngest single grain dates of ca. 17.4 ± 0.5 and 10.5 ± 0.5 Ma (1σ uncertainty), respectively (Finzel and Enkelmann, 2017), the latter of which is consistent with more robust age constraints on the Kenai Peninsula. Recent biostratigraphic results on the west side of the basin support a middle to late Miocene age for these strata (Zippi and Loveland, 2012; Zippi and others, 2021).

### Sterling Formation (Ts)

Sterling Formation strata are commonly thought to be absent at the surface on the west side of the CIB (e.g. Magoon and others, 1976; Wilson and others, 2012). However, recent stratigraphic work (LePain and others, 2013), along with new geologic mapping (Gillis and others, in preparation), document that the lowermost Sterling exposed in bluffs along the lower Beluga River (fig. 4) is in depositional contact with the underlying Beluga Formation. This finding is supported by nearby subsurface mapping using area seismic and well data (Gillis and others, in preparation). Sterling Formation exposures along the Beluga River are dominated by thick cross-stratified, friable sandstone; minor siltstone; and few, thin lignitic coal beds that record a transition from an anastomosing, single-thread fluvial system in the underlying Beluga Formation to a sandy, braided fluvial system during a period of high sediment supply and rapid subsidence (LePain and others, 2013). On the Kenai Peninsula on the east side of Cook Inlet, Sterling Formation outcrops serve as the type section for the Pliocene Clamgulchian floral stage (Wolfe and others, 1966). The age of Sterling strata on the west side is poorly defined, but results from one palynologic sample collected from an outcrop on the lower Beluga River produced a latest Miocene/early Pliocene age call (Zippi and others, 2021) that is consistent with the age assignment of Wolfe and others (1966).

## ORGANIZATION OF THE ANALYTICAL DATA AND RESULTS

In order to restrict the body of this report to a manageable size, all descriptions of methods and analytical results are included as appendices and tables at the end of the text. A description of the $^{40}Ar/^{39}Ar$ and U–Pb analytical methods can be found in appendix A. Appendices B and C present the zircon U–Pb and $^{40}Ar/^{39}Ar$ analytical results, respectively. Appendices D–G summarize in detail the results of multi-mineral $^{40}Ar/^{39}Ar$ and zircon U–Pb analyses for each sample, and include a brief sample description, relevant figures, and brief interpretation of the results based on the age selection criteria outlined below and available geological constraints. Appendix H tabulates all the geochronologic dates and presents the preferred dates and location for each sample. Appendix I is a worksheet that documents the calculation of multi-mineral $^{40}Ar/^{39}Ar$ cooling rates for each plutonic body analyzed in the field area. Appendix J provides samples descriptions, classification codes, and locations for all major oxide analyses.

### Age Determination Criteria and Selection of Preferred Dates

#### Zircon U–Pb

Zircon U–Pb analytical methods are outlined in appendix A, and data files are located in appendix B. Zircon U–Pb and $^{40}Ar/^{39}Ar$ dates are summarized in tables 1–3 and appendix H. Prior to interpreting U–Pb results for each sample, a conservative concordance filter was applied to all grain dates. Individual zircon dates with 2σ uncertainties that do not overlap the 2σ envelope of the concordia line were omitted from further consideration (Spencer and others, 2016). In practice, however, omission of discordant zircons from our analyses was rare. Paleozoic and older grains, which more readily reveal open isotopic system behavior (i.e., Pb loss) than do younger zircons, are generally uncommon in this study and do not bear on crystallization or stratal ages of the sampled units. More significantly, the relatively low precision of the LA-ICPMS method and the shallow trajectory of pre-Paleozoic dates below the concordia line due to lead loss combine to render compromised isotopic systems in young (post-Paleozoic) zircons practically undetectable (Kryza and others, 2012; Spencer and others, 2016). We aimed to diminish the impacts of potential Pb loss in Meso–Cenozoic zircons by favoring weighted mean (WM) approaches in interpreting date distributions.

For the forearc strata, older zircons commonly dominate the date distributions of all but a few tephras analyzed for this study. This indicates that even apparent event beds were likely reworked by sedimentary processes prior to deposition and probably include syn-eruptive, xenocrystic, and detrital zircons. Therefore, maximum depositional ages (MDAs) defined by populations of young zircons were determined for all of the forearc basin samples, including most tephras. Several protocols have been presented in the literature for establishing MDAs for sedimentary samples (see Dickinson and Gehrels, 2009), yet the geochronology community continues to work toward a standardized approach (e.g., Spencer and others, 2016; Coutts and others, 2019; Herriott and others, 2019). In calculating MDAs for the Cook Inlet forearc strata we opted for a recently developed protocol—youngest statistical population (YSP; Coutts and others, 2019). This approach is a reliable means of calculating a MDA with a low likelihood of producing a date that is younger than the true stratigraphic age of the sampled interval (Coutts and others, 2019), which would violate the fundamental criterion of a MDA (see also Herriott and others, 2019). The YSP determination is the weighted mean (WM) of two or more of the youngest zircons (ranked by date) that yield a mean squared weighted deviation (MSWD) value close to 1.0. In rare instances where a YSP was not attained, the WM of the youngest cluster of three or more zircon dates that overlap at 2σ (YC2σ; Dickinson and Gehrels, 2009) was used instead. If neither a YSP nor YC2σ determination could be made, then the youngest single grain (YSG; Dickinson and Gehrels, 2009) was assigned as the MDA provided that it was

geologically reasonable, and also recognizing that the determination has diminished reliability (Coutts and others, 2019; Sharman and Malkowski, 2020).

Determining the crystallization age of an igneous rock requires dating only zircons that grew immediately prior to magma crystallization (autocrystic grains; Miller and others, 2007) However, igneous rocks can contain significant quantities of antecrystic zircons (older grains that suggest long magma residence times [Hildreth, 2001; Charlier and others, 2005]) and xenocrystic grains inherited from wall rock that must be excluded prior to calculating the WM. Few strategies have been developed for distinguishing antecrystic and xenocrystic grains in LA-ICPMS data (e.g., Campbell and others, 2006; Seigel and others, 2018) and a standardized approach for doing so has not been established. At present, the only quantitative method leverages differences in grain chemistry and zircon zonation with respect to the laser spot location to help differentiate genetically distinct zircon populations (Seigel and others, 2018); information our data lack. However, autocrystic grains are expected to define a normal distribution of the youngest quantity of zircons in an igneous rock (Campbell and others, 2006). We therefore calculate crystallization dates for this study by adapting our detrital zircon WM MDA methodology to filter statistical outliers from the younger and older ends of the grain date distribution. We interpret the youngest few zircons that fall outside of the n-dependent 2σ (95 percent probability) envelope to have experienced lead loss, rather than the less likely possibility that they represent only 1–3 percent of the grains analyzed per sample that are autocrystic. In practice, young results were omitted from only 3 samples, changing their dates by less than the WM uncertainty in each case.

All U–Pb WMs presented here were determined using an Excel spreadsheet developed by the Boise State University Isotope Geology Laboratory (Herriott and other, 2019). This spreadsheet reports three levels of WM uncertainties that include cumulative contributions (sources) of uncertainty: analytical; analytical and systematic; analytical, systematic, and decay constant (see Schoene, 2014). We employ U–Pb WM dates that incorporate systematic uncertainties, which are determined by propagating in quadrature a factor that characterizes the long-term excess variance of reference zircons employed during the analytical sessions (apps. A7 and A8; Chang and others, 2006; Horstwood and others, 2016). U–Pb weighted mean and concordia diagrams were generated using the free open-source program IsoplotR (Vermeesch, 2018) in which input errors were set to 2σ; systematic uncertainties are graphically portrayed and reported for the WMs in each ranked date plot in the appendices.

### $^{40}Ar/^{39}Ar$

$^{40}Ar/^{39}Ar$ methodology is presented in appendix A, and all data files are in appendix C. A summary of the $^{40}Ar/^{39}Ar$ results is provided in tables 1–3 and appendix H, with all dates quoted to the ± 2σ level and calculated using the constants of Renne and others (2010). For unaltered mineral phases or groundmass that remained largely closed isotopic systems, three dates are presented for each analysis: integrated, plateau, and inverse isochron (also simply referred to as "isochron"). The integrated, plateau, and inverse isochron dates were determined from the isotopic ratios for each step calculated from corrected measurements weighted by the amount of $^{39}Ar$ released per step. The integrated date is determined by the total gas measured, analogous to a potassium-argon (K–Ar) result. The plateau age is defined by three or more consecutive gas release fractions that are within two standard deviations of each other (MSWD less than 2.5) and equivalent to no less than 50 percent of the total gas released. For cases in which all the requirements of a plateau age are not met, a weighted mean age is calculated by selecting steps that best approach all the criteria of a plateau age (≤2.5 MSWD; ≥50 percent $^{39}Ar$ release; 3 or more consecutive steps). Inverse isochron dates are determined by regressing the ratio of $^{36}Ar/^{40}Ar$ to $^{39}Ar/^{40}Ar$ for each temperature step. The inverse isochron date reported here is

based on the identical temperature steps that define the plateau. Additional discussion of the results of each date analysis appears below.

Interpretation of the $^{40}Ar/^{39}Ar$ dates often leverage geologic field observations, and zircon U–Pb and palynologic ages from the same samples or from samples collected nearby from the same unit (see Zippi and Loveland, 2012; Zippi and others, 2021; Gillis and others, in preparation; this report). Preference was assigned to one of the three calculated $^{40}Ar/^{39}Ar$ dates for each sample (integrated, plateau, or inverse isochron) based on an assessment of the following—the number of gas fractions used for the calculation and their total gas release, the character of the age spectra and isochrons, the magnitude of the analytical uncertainty, and value of the MSWD. If the plateau and isochron age calculations agreed within error, the date calculated using the most gas released over the greatest number of temperature steps and yielding the lowest uncertainty and MSWD closest to unity (1.0) was usually preferred. Integrated dates were favored for cases in which the age spectra were highly disturbed and failed to define a plateau, and in which the argon isotopic ratios failed to produce an isochron, provided that the dates appeared geologically meaningful. If none of the calculated $^{40}Ar/^{39}Ar$ dates agreed within error with nearby U–Pb dates, then the date closest to the U–Pb date within analytical error was selected as the preferred $^{40}Ar/^{39}Ar$ date but was noted to be potentially problematic.

### Multiple Diffusion Domain (MDD) forward modeling

Thermal history modeling of potassium feldspar is based on the multiple diffusion domain theory of Lovera and others (1989) in which various diffusion length scales intrinsic to potassium feldspar make it sensitive to argon retention over a wide range of temperatures between approximately 150 and 350˚C (Foland, 1994; Quidelleur and others, 1997). Results of a furnace diffusion experiment carried out on a single sample were statistically compared to randomly generated theoretical time-temperature curves using a non-linear, least-squares routine based on the Levenberg-Marquardt method described in Quidelleur and others (1997). A chi-squared merit function evaluated the possible solutions against the measured data and the routine was halted when the fractional decrease was less than 0.0001 (the solutions converged). The routine and supporting scripts are freely available for download at https://sims.ess.ucla.edu/argonlab/. The furnace step heating experiment is described in app. A.

### Age Nomenclature

We refer to the International Stratigraphic Chart (2018/08, Cohen and others, 2013, updated) throughout the text for all references to geologic age. Informal usage of early, middle, and late for subdividing epochs was used to focus attention to a part of the geologic timescale without implying specific stages or date ranges.

## SUMMARY OF RESULTS

### Plutonic and Volcanic Crystallization

Zircon U–Pb crystallization dates for intrusive and extrusive rocks sampled from the Neacola and Tordrillo mountains, and from Beluga Mountain to their northeast, range in age from ca. 84.3 to 55.8 Ma. $^{40}Ar/^{39}Ar$ hornblende results from the same samples overlap with or slightly predate the zircon crystallization, suggesting that hornblende dates closely approximate ages of intrusive bodies in the field area. When considered with geochemical data from the same samples, the dates tentatively define 4 periods of arc magmatism at ca. 84–77 Ma, ca. 74–71 Ma, ca. 69–66 Ma, and ca. 62–56 Ma along a 120-km-long trend from the Neacola Mountains to the southwestern margin of Susitna basin (figs. 3 and 4; table 1). Most Late Cretaceous intrusive rocks were emplaced from 74.3 ± 2.8–68.5 ± 1.6 Ma, but an earlier, less well-resolved episode of plutonism occurred from 84.3 ± 1.9–77.3 ± 1.8 Ma. Two samples analyzed for zircon U–Pb and hornblende $^{40}Ar/^{39}Ar$ from the ca. 69–66 Ma rocks produce identical results within analytical uncertainty, consistent with extremely rapid cooling to below approximately 500˚C due

**Table 1.** Zircon U-Pb and $^{40}Ar/^{39}Ar$ results for igneous rocks.

| Sample # | Location | Unit | Lithology | App. # | Analysis type | Mineral | Preferred analysis date ± 2σ uncertainty (Ma) | Criteria | Comment | Inferred crystallization/ cooling/maximum depositional age ± 2σ (Ma) |
|---|---|---|---|---|---|---|---|---|---|---|
| **Cretaceous Intrusive Rocks** | | | | | | | | | | |
| 07BG276b | Mount Susitna | Kgd | Granodiorite | D13 | $^{40}Ar/^{39}Ar$ | Biotite | 65.8 ± 0.6 | Plateau | Post-crystallization cooling age | — |
| | | | | | $^{40}Ar/^{39}Ar$ | Feldspar | 63.0 ± 0.6–61.2 ± 0.6 | Max.–min. | Cooling from ~350°–150°C | |
| 07BG275b | Mount Susitna | TKgd | Granodiorite | D12 | $^{40}Ar/^{39}Ar$ | Hornblende | 70.5 ± 1.2 | Plateau | Approximate crystallization age | 70.5 ± 1.2 |
| | | | | | $^{40}Ar/^{39}Ar$ | Biotite | 67.6 ± 0.6 | Plateau | Post-crystallization cooling age | |
| | | | | | $^{40}Ar/^{39}Ar$ | Feldspar | 65.2 ± 0.6–61.1 ± 0.8 | Max.–min. | Cooling from ~350°–150°C | |
| 10LF307c | Neacola Mountains | Kg | Quartz vein | D11 | $^{40}Ar/^{39}Ar$ | Muscovite | 64.4 ± 2.4 | Plateau | Potential alteration age | — |
| 10LF304a | Neacola Mountains | Kmg | Monzogranite | D10 | U-Pb | Zircon | 68.5 ± 1.6 | YSP | Crystallization age | 68.5 ± 1.6 |
| | | | | D9 | $^{40}Ar/^{39}Ar$ | Hornblende | 69.1± 1.4 | Inv. isochron | Approximate crystallization age consistent with zircon U-Pb date | |
| | | | | | $^{40}Ar/^{39}Ar$ | Biotite | 65.8± 1.4 | Plateau | Post-crystallization cooling age | |
| 07EF027a | Neacola Mountains | Kgd | Granodiorite | D8 | $^{40}Ar/^{39}Ar$ | Hornblende | 69.3 ± 1.2 | Plateau | Approximate crystallization age | 69.3 ± 1.2 |
| | | | | | $^{40}Ar/^{39}Ar$ | Biotite | 64.7 ± 0.6 | Plateau | Post-crystallization cooling age | |
| | | | | | $^{40}Ar/^{39}Ar$ | Feldspar | 61.7 ± 0.8 | Plateau | Post-crystallization cooling age | |
| 07EF028a | Neacola Mountains | Kgd | Granodiorite | D7 | $^{40}Ar/^{39}Ar$ | Hornblende | 71.0 ± 1.2 | Plateau | Approximate crystallization age | 71.0 ± 1.2 |
| | | | | | $^{40}Ar/^{39}Ar$ | Biotite | 67.5 ± 0.6 | Plateau | Post-crystallization cooling age | |
| | | | | | $^{40}Ar/^{39}Ar$ | Feldspar | 65.5 ± 0.4–61.0 ± 0.4 | Max.–min. | Cooling from ~350°–150°C | |
| 10BAE351a | Neacola Mountains | Kgd | Granodiorite | D6 | $^{40}Ar/^{39}Ar$ | Hornblende | 71.8 ± 1.4 | Plateau | Approximate crystallization age | 71.8 ± 1.4 |
| | | | | | $^{40}Ar/^{39}Ar$ | Biotite | 69.5 ± 1.2 | Plateau | Post-crystallization cooling age | |
| 10BAE353b | Neacola Mountains | Kqd | Quartz diorite | D5 | $^{40}Ar/^{39}Ar$ | Hornblende | 73.4 ± 8.6 | Plateau | Minimum crystallization age, low T Ar loss | 73.4 ± 8.6 |
| | | | | | $^{40}Ar/^{39}Ar$ | Biotite | 75.0 ± 2.2 | Plateau | Suspected excess argon retention, low T Ar loss | |
| 10LF255a | Neacola Mountains | Kga | Gabbro | D4 | $^{40}Ar/^{39}Ar$ | Hornblende | 74.3 ± 2.8 | Plateau | Approximate crystallization age, low T Ar loss | 74.3 ± 2.8 |
| | | | | | $^{40}Ar/^{39}Ar$ | Biotite | 75.7 ± 2.8 | Plateau | Suspected excess argon retention, low T Ar loss | |
| 10LF282a | Lone Ridge | Kgd | Diorite | D3 | U-Pb | Zircon | 77.8 ± 1.9 | YSP | Crystallization age | 77.8 ± 1.9 |
| | | | | D2 | $^{40}Ar/^{39}Ar$ | Hornblende | 78.0 ± 5.2 | Integrated | Approximate crystallization age consistent with zircon U-Pb age | |
| | | | | | $^{40}Ar/^{39}Ar$ | Biotite | 75.8 ± 1.6 | Plateau | Post-crystallization cooling age | |
| 09PD272a | Lone Ridge | Kdi | Diorite | D1 | U-Pb | Zircon | 84.3 ± 1.9 | YSP | Crystallization age | 84.3 ± 1.9 |
| **Paleocene Intrusive Rocks** | | | | | | | | | | |
| 07BG256b | Spurr-Capps Glacier area (Capps granitoid) | Tg | Biotite granite | E11 | U-Pb | Zircon | 55.8 ± 1.3 | YSP | Crystallization age. Youngest grain omitted (see Appendix F12) | 55.8 ± 1.3 |
| | | | | E10 | $^{40}Ar/^{39}Ar$ | Biotite | 61.6 ± 1.2 | Plateau | Excess Ar retention | |
| 08MAW207a | Spurr-Capps Glacier area (Capps granitoid) | Tg | Biotite granite | E9 | U-Pb | Zircon | 56.8 ± 1.3 | YSP | Crystallization age | 56.8 ± 1.3 |
| 10LF315b | Capps Glacier area (Capps granitoid) | Td | Basaltic andesite dike | E8 | $^{40}Ar/^{39}Ar$ | Whole rock | 56.8 ± 1.8 | Plateau | Maximum crystallization age | 56.8 ± 1.8 |
| 10BAE398a | Capps Glacier area (Capps granitoid) | Td | Andesite dike | E7 | $^{40}Ar/^{39}Ar$ | Whole rock | 58.6 ± 1.4 | Plateau | Maximum crystallization age | 58.6 ± 1.4 |

**Table 1, continued.** Zircon U-Pb and $^{40}Ar/^{39}Ar$ results for igneous rocks.

| Sample # | Location | Unit | Lithology | App. # | Analysis type | Mineral | Preferred analysis date ± 2σ uncertainty (Ma) | Criteria | Comment | Inferred crystallization/ cooling/maximum depositional age ± 2σ (Ma) |
|---|---|---|---|---|---|---|---|---|---|---|
| 07BG252b | Spurr-Capps Glacier area (Capps granitoid) | Tg | Biotite granite | E6 | $^{40}Ar/^{39}Ar$ | Biotite | 61.0 ± 1.0 | Integrated | Excess Ar retention, exceeds zircon U-Pb date of granite body | 59.5 ± 1.2 |
| | | | | | | Potassium feldspar | 59.5 ± 1.2 | Inv. isochron | Excess Ar retention, slightly exceeds zircon U-Pb date of granite body | |
| 11BG019a | Beluga Mountain | Tv | Andesite sill(?) | E5 | U-Pb | Zircon | 57.7 ± 1.4 | YSP | Crystallization age | 57.7 ± 1.4 |
| 07BG271b | Little Mt. Susitna | Tg | Granite | E4 | $^{40}Ar/^{39}Ar$ | Hornblende | 60.7 ± 1.6 | Plateau | Approximate crystallization age | 60.7 ± 1.6 |
| | | | | | | Potassium feldspar | 57.7 ± 1.2 | Plateau | Minimum crystallization age | |
| 07BG270b | Little Mt. Susitna | Tg | Granite | E3 | $^{40}Ar/^{39}Ar$ | Hornblende | 61.6 ± 1.0 | Plateau | Approximate crystallization age | 61.6 ± 1.0 |
| | | | | | $^{40}Ar/^{39}Ar$ | Biotite | 62.8 ± 0.6 | Plateau | Suspected excess argon retention | |
| | | | | | $^{40}Ar/^{39}Ar$ | Potassium feldspar | 62.4 ± 0.4–59.6 ± 0.8 | Max.–min. | Cooling from ~350°–150°C | |
| 10LF298a | Neacola Mountains | TKg | Granite | E2 | U-Pb | Zircon | 65.3 ± 1.6 | YSP | Crystallization age | 65.3 ± 1.6 |
| | | | | E1 | $^{40}Ar/^{39}Ar$ | Hornblende | 69.2 ± 1.0 | Integrated | Excess Ar retention | |
| | | | | | $^{40}Ar/^{39}Ar$ | Biotite | 65.5 ± 1.4 | Plateau | Approximate crystallization age | |
| | | | | | | Feldspar | 63.9 ± 1.8–61.8 ± 1.4 | Max.–min. | Cooling from ~350°–150°C | |
| **Latest Cretaceous Volcanic and Volcaniclastic Rocks** | | | | | | | | | | |
| 09BG415c | Neacola Mountains | Kd | Mafic dike | F7 | $^{40}Ar/^{39}Ar$ | Biotite | 70.6 ± 1.4 | Plateau | Approximate crystallization age | 70.6 ± 1.4 |
| 09BG415a | Neacola Mountains | Kd | Potassium feldspar pegmatite | F7 | $^{40}Ar/^{39}Ar$ | Biotite | 72.5 ± 1.6 | Plateau | Approximate crystallization age | 72.5 ± 1.6 |
| | | | | | $^{40}Ar/^{39}Ar$ | Feldspar | 67.2 ± 0.8–63.4 ± 1.0 | Max.–min. | Cooling from ~350°–150°C | |
| 07BG257b | Capps Glacier area | Kv | Metabasalt | F6 | $^{40}Ar/^{39}Ar$ | Plagioclase | 59.7 ± 1.4 | Integrated | Inferred thermally-reset Kv | — |
| 08DL053-0.0a-2 | Capps Glacier area | Kv | Metabasalt | F5 | U-Pb | Zircon | 77.3 ± 1.8 | YSP | Extrusive age | 77.3 ± 1.8 |
| **Paleocene Volcanic and Volcaniclastic Rocks** | | | | | | | | | | |
| 10LF311b | Capps Glacier area | Tv | Trachy-andesite flow | F4 | $^{40}Ar/^{39}Ar$ | Whole rock | 59.0 ± 1.2 | Plateau | Extrusive age | 59.0 ± 1.2 |
| 09PD206a | Capps Glacier area | Tv | Volcaniclastic | F3 | U-Pb | Zircon | 61.1 ± 2.6 | YSG | Maximum depositional age defined by youngest geologically reasonable date | 61.1 ± 2.6 |
| 11TMH024a | Beluga Mountain | Tv | Lava | F2 | U-Pb | Zircon | 58.5 ± 1.5 | YSP | Extrusive age | 58.5 ± 1.5 |
| 11BG022a | Beluga Mountain | Tv | Volcaniclastic | F1 | U-Pb | Zircon | 61.1 ± 1.4 | YSP | Maximum depositional age | 61.0 ± 1.4 |

to mesozonal emplacement. The Paleocene granitic suite (ca. 61.6–55.8 Ma; table 1) is best constrained by zircon U–Pb results to between 56.8 ± 1.3 and 55.8 ± 1.3 Ma. $^{40}Ar/^{39}Ar$ data from the Paleocene rocks indicate retention of excess argon for every mineral phase analyzed (hornblende, biotite, potassium feldspar, and plagioclase) in some cases, with extraneous argon in biotite being most prevalent. Nevertheless, potassium feldspar results from two samples (07BG271b; fig. E4, and 07BG252b; fig. E6) whose integrated, plateau, and inverse isochron dates are identical within analytical error are no younger than ca. 57.7 Ma, indicating epizonal crystallization and geologically instantaneous cooling below approximately 150 ˚C within the resolution of the techniques.

Episodes of Late Cretaceous and Paleocene volcanism associated with emplacement of the plutonic rocks summarized above occurred at about 77 and 61 Ma. Volcanic rocks related to the latest Cretaceous–earliest Paleocene episodes of arc magmatism (ca. 74–66 Ma) have not been identified in the field area. Altered 77.3 ± 1.8 Ma volcanic rocks with pillow morphologies along the southeastern Tordrillo mountain front underlay middle Eocene West Foreland Formation at the Capps Glacier fault (figs. 3 and 4; Gillis and others, 2017). Their eruption age overlaps with the nearby Lone Ridge diorite (ca. 84.3–77.8 Ma) that locally forms the faulted Eocene basin margin to the southeast (figs. 3 and 4) and are likely genetically related to the granodiorite. Paleocene volcaniclastic strata composing Beluga Mountain (fig. 3) and an andesitic sill(?) that intrudes them (fig. 3) range in age from 61.1 ± 2.6 to 57.7 ± 1.4 (zircon U–Pb; table 1; apps. F1–F2, and appendix E5, respectively). The volcanogenic strata are ostensibly in igneous contact with the 61.6 ± 1.0–60.7 ± 1.6 Ma (hornblende $^{40}Ar/^{39}Ar$; table 1; apps. E3 and E4) Little Mount Susitna granitoid (fig. 3; Wilson and others, 2012), suggesting that the granite intrudes its volcanic carapace. Paleocene mafic to intermediate dikes (58.6 ± 1.4–56.8 ± 1.8 Ma, whole rock-$^{40}Ar/^{39}Ar$; table 1; apps. E7 and E8) that intrude the ca. 56.8–55.8 Ma Capps granite (fig. 4) must post-date granitoid crystallization and likely yield dates that are slightly too old due to excess argon retention, as with other argon systems from the granitic body.

## Post Crystallization Intrusive Cooling

### Cretaceous-Paleocene Cooling

Cooling of intrusive rocks after their emplacement and crystallization in the crust is a passive process whose rate is governed on a first-order by the thermal gradient between the hot plutonic body and cooler country rock into which it intrudes (Harrison and McDougall, 1980). However, conductive asymptotic cooling can be attenuated by subsequent reheating from nearby intrusions or enhanced by syntectonic processes (Davis and others, 2012; Foster and Fanning, 1997). Moreover, intrusive bodies at thermal equilibrium in the middle crust can be overprinted by upper crustal processes such as brittle faulting and erosion (Ehlers, 2005). Determining patterns of cooling is therefore important for understanding the igneous and tectonic processes active from pluton emplacement to its exhumation to the surface.

To determine trends and estimate rates of cooling of the Late Cretaceous to early Paleocene outcrops from approximately 800 to 150˚C, we use the mineral pair method (e.g., Benjamin and others, 1987), in which the difference in the nominal closure temperature of two co-existing minerals is divided by the difference in their respective closure dates (app. I). For instance, the rate of cooling from melt crystallization ~800 to 500˚C is calculated using zircon and hornblende dates from the same sample. However, estimating when and how rapidly the intrusive rocks in the study area cooled below their crystallization temperatures is complicated by suspected unquantified or unidentified excess argon (externally sourced radiogenic argon incorporated into the crystal lattice) in some of the analyzed mineral phases. Unidentified excess argon is a particular concern for inter-

preting biotite dates because the mineral is known to yield a well-defined plateau despite having a compromised isotopic system (Gileti, 1974b). The biotite results (closure temperature equals approximately 350–300˚C; Harrison and others, 1985; Grove and Harrison, 1996; McDougall and Harrison, 1999) produce dates that in many cases are uncharacteristically older than hornblende aliquots (closure temperature equals approximately 500˚C; Harrison, 1981) from the same sample (fig. 6), suggesting uptake of excess argon in the biotite despite evidence of minor argon loss from the biotite's lower retentivity sites. Moreover, the biotite fractions produce dates that are uniformly older than the maximum dates of co-existing potassium feldspar (fig. 6), which begins retaining argon at approximately the same temperature (350˚C; Foland, 1994; Quidelleur and others, 1997), further suggesting widespread radiogenic argon contamination of biotite. Conversely, only 2 of 11 biotite analyses (apps. D6 and D8) produced inverse isochrons that confirmed an initial argon content ($^{36}Ar_i$) near atmospheric values (i.e., a simple two-reservoir argon system that lacks an excess component; Heizler and Harrison, 1988). Due to their apparent poor fidelity, we omit the

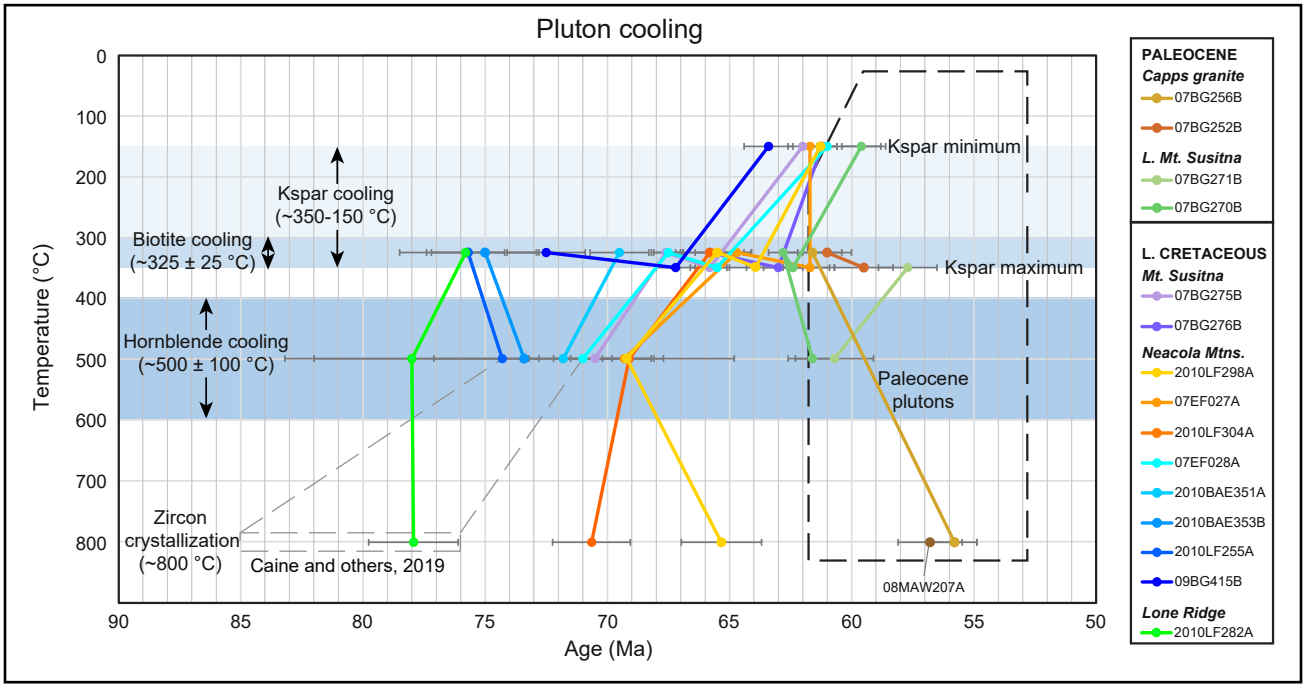


**Figure 6.** $^{40}Ar/^{39}Ar$ and zircon U-Pb age-temperature plots of all analyses for Late Cretaceous and Paleocene plutons. Colored solid circles are coded by sample and mark the thermochronometer date with respect to the average accepted closure temperature range of the thermochronometer. Colored lines connecting the circles represent simplified linear cooling paths between thermochronometer closures. Dashed gray rectangle represents the zircon U–Pb age range of plutons located southeast of the Lake Clark fault in the Neacola-Chigmit Mountains (Caine and others, 2019). Gray dashed lines connect zircon U–Pb dates by others to $^{40}Ar/^{39}Ar$ results from the same plutons (this study). Blue-shaded temperature regions represent closure temperature ranges for hornblende, biotite, and potassium feldspar. Negative time temperature slopes between hornblende and biotite are interpreted to be a function of suspected excess argon retention in biotite. The negative slope between biotite and potassium feldspar maximum ages are interpreted to be a function of their overlapping closure temperatures and the mean value used for biotite (325 ˚C), which is slightly cooler than the accepted maximum temperature of potassium feldspar Ar closure (approximately 350 ˚C). However, the ages become abruptly younger between biotite and feldspar closure, suggesting a 1–5 Ma isothermal condition at approximately 350 ˚C for each sample, or retention of excess argon that produced a biotite cooling age that is artificially older than the potassium feldspar maximum date. The diverse timing at which the isothermal step occurs for each sample supports the latter. Date uncertainty bars represented by thin black horizontal lines with short, thin vertical lines at their endpoints. Black dashed outline represents the time-temperature space occupied by Paleocene plutons.

biotite results from cooling rate calculations and instead estimate the rate of cooling from approximately 500 to 350˚C using hornblende and potassium feldspar maximum closure dates (fig. 7).

Unlike hornblende and biotite which consist of single diffusion length scales over which argon is lost above their respective closure temperatures, potassium feldspar hosts multiple diffusion length scales (domains) that control argon loss over a broad range of temperatures from about 350 to 150˚C (Foland, 1994; Quidelleur and others, 1997). Therefore, a cooling rate over an approximately 200˚C span can be estimated directly from its maximum and minimum dates. Importantly, the temperature sensitivity of argon diffusion from potassium feldspar over such a broad range makes it amenable to thermal modeling. Multiple domain diffusion modeling, or MDD, can thus be a powerful tool for reconstructing the medium- to low-temperature cooling history of a sample and identifying rate changes with time (e.g., Quidelleur and others, 1997).

Calculated rates of cooling from zircon crystallization to hornblende argon closure in the study area are rapid to geologically instantaneous for all samples (20 ˚C/m.y. to infinite) (fig. 7; app. I). Some samples from the Neacola Mountains lack zircon U–Pb dates, so their rates were estimated using crystallization ages from nearby samples reported by Caine and others, (2019) (fig. 7). The results indicate melt emplacement at mid- to upper-crustal depths. Hornblende-feldspar mineral pairs from Late Cretaceous–earliest Paleocene granitoids yield an average cooling rate of 33˚C/m.y. beginning earlier than 71

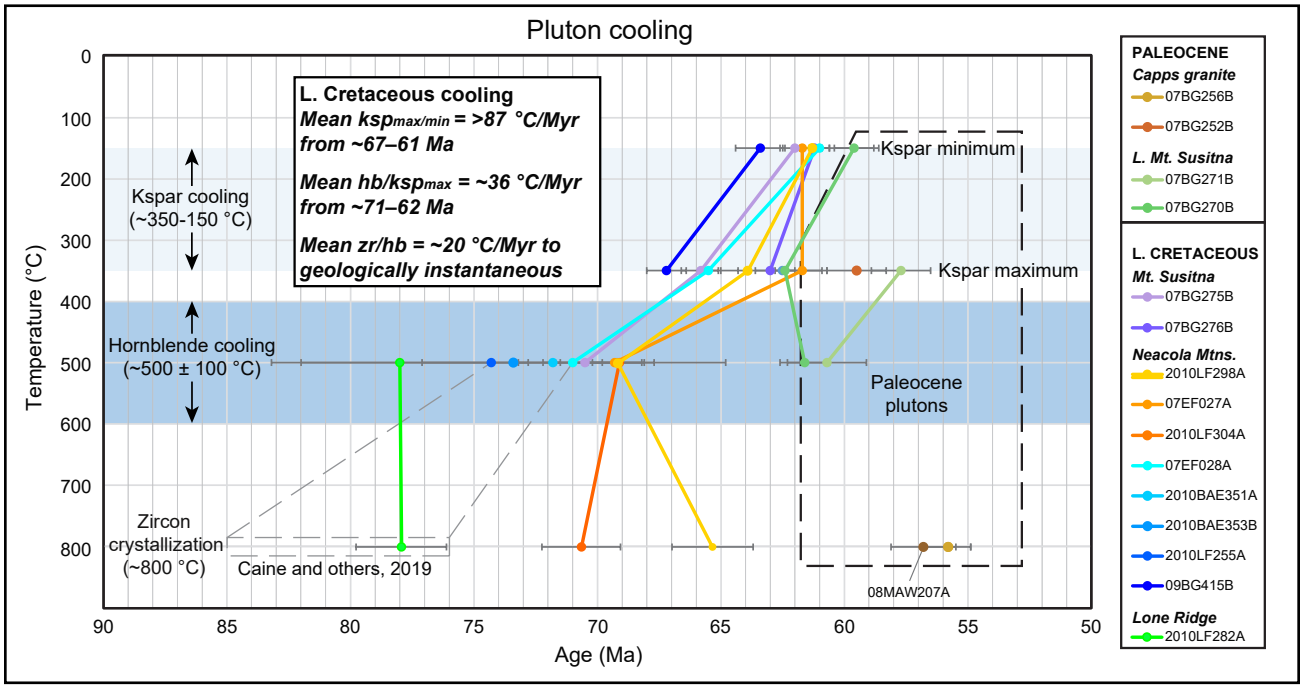


**Figure 7.** $^{40}Ar/^{39}Ar$ and zircon U-Pb age-temperature plots of all analyses for Late Cretaceous and Paleocene plutons similar to fig. 6, but with biotite results omitted (see text for discussion). Solid circles color coded by sample mark the therrmochronometer date with respect to the average accepted closure temperature range of the thermochronometer. Colored lines connecting the circles represent generalized cooling paths between thermochronometer closure. Dashed gray rectangle represents the zircon U–Pb age range of plutons located southeast of the Lake Clark fault in the Neacola-Chigmit Mountains (Caine and others, 2019). Gray dashed lines connect zircon U–Pb dates by others to $^{40}Ar/^{39}Ar$ results from the same plutons (this study). Blue-shaded temperature regions represent closure temperature ranges for hornblende and potassium feldspar. Note the three-fold increase in cooling rate from approximately 25 ˚C/Myr to 78 ˚C/Myr between 67 and 60 Ma, which suggests that cooling was dynamic (rather than passive asymptotic thermal decay after melt emplacement). Date uncertainty bars represented by thin black horizontal lines with short, thin vertical lines at their endpoints.

to 62 Ma (fig. 7; app. I), implying that rapid cooling of the intrusive bodies to about 500°C was followed by slower cooling to approximately 350°C. This thermal decay is consistent with mesozonal melt emplacement and conductive cooling to the ambient crustal temperature (Dodson, 1973). However, maximum and minimum potassium feldspar dates suggest that the average rate of cooling more than doubled to about 88°C/m.y. between ca. 67 and 60 Ma (fig. 7; app. I).

A challenge to interpreting time-temperature trajectories using the mineral pair method, however, is that the analytical uncertainties of the cooling dates and closure temperature estimates allow for a range of permissible cooling paths. In the study area, these uncertainties permit rocks to have cooled at a uniform rate to 150°C with no acceleration, particularly if hornblende closed at temperatures significantly greater than 500°C or at the younger uncertainty range of its cooling dates (fig. 7). Rapid linear cooling of intrusive rocks to low temperatures is most commonly achieved following emplacement in the uppermost crust prior to reaching thermal equilibrium. However, characteristics common to very shallow crystallization and cooling such as a dominant fine grain size, porphyritic and granophyric textures, and miarolitic cavities (Candella, 1977) have not been identified in Late Cretaceous plutons in the study area and their absence favors emplacement at deeper crustal levels. Alternately, linear cooling could result from a combination of conduction and erosional unroofing but would require exponential thermal decay after emplacement at a lower crustal level to be balanced by exponentially accelerating exhumation cooling to upper crustal levels at the same rate—a special case we consider unlikely. Therefore, despite the latitude for uniform cooling from 500–150°C, we favor a two-phase model as suggested by the nominal date and closure temperature values.

The inference of punctuated cooling is supported by a MDD model of a Mount Susitna granodiorite sample (fig. 3). The sample initially cooled slowly from 65 Ma or earlier at about 9°C/m.y. before accelerating to approximately 97°C/m.y. from 63 Ma to 61 Ma or later (fig. 8, app. D12K–M). Notably, the model results demonstrate that regardless of the cooling age and closure temperature uncertainties of hornblende, a reduction and subsequent acceleration in cooling rate is required for the pluton to reach near-surface temperatures, corroborating results using the mineral pair method. Such acceleration requires that a mechanism other than thermal conduction at mid-to upper-crustal levels controlled cooling near the Cretaceous-Paleocene boundary, which will be explored further in the Discussion section below.

Paleocene intrusive rocks reveal a relatively simple cooling history despite excess argon reten-

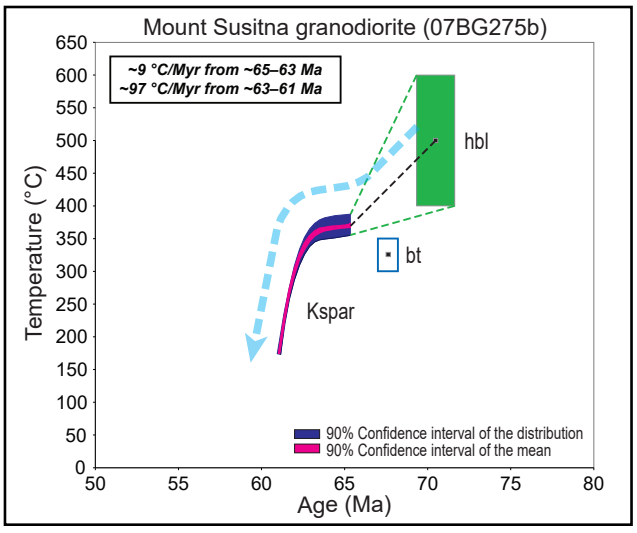


**Figure 8.** Potassium feldspar multi-domain diffusion model of a sample collected from the Mount Susitna granodiorite (fig. 3) constrained to cool monotonically. Results of unconstrained model runs (not shown) best define simple cooling with no reheating. Hornblende (green filled rectangle) and biotite (blue unfilled rectangle) from the same sample plotted with the K-feldspar model in time-temperature space. Extents of rectangles reflect date and nominal closure temperature (Tc) uncertainties. Biotite date omitted due to suspected excess argon. Results show that regardless of hornblende date and Tc uncertainties, the cooling rate must have decayed prior to accelerating at approximately 63 Ma. Blue dashed arrow schematically reflects the two-phase cooling trajectory from mid- to upper-crustal temperatures. Note temperature decreases downward and time decreases to the left, opposite of mineral pair cooling plots (figs. 6 and 7).

tion in many of their thermochronometers (figs. 10 and 11; app. I). Cooling of Paleocene granites from emplacement to below approximately 150˚C occurred over a brief period from ca. 60 to 56 Ma. Zircon crystallization ages from the Capps granite are slightly younger than biotite and argon ages from the same samples, which retained small amounts of excess argon. However, the zircon ages are identical within analytical uncertainty to a nearby feldspar sample whose inverse isochron suggests sound argon systematics, indicating instantaneous cooling from zircon crystallization to less than 150˚C within the resolution of the geochronometers. The Little Mount Susitna granite also records very rapid cooling from approximately 500 to 150˚C at rates of approximately 75–150˚C/m.y. despite excess argon retention in biotite (fig. 7; app. I). These results suggest melt emplacement in the upper crust with only minor unroofing (<3–6 km) since approximately 56 Ma.

## Stratigraphic Age Constraints

U–Pb and $^{40}Ar/^{39}Ar$ results summarized below supplement a growing stratigraphic geochronological database for the Cook Inlet basin and represent the largest collection of radiometric ages produced for West Foreland Formation strata. Most of the results are from interbedded tephras and volcaniclastic sandstones collected near the base of the Cenozoic succession in the study area. Volcanogenic material is rare in the younger Cenozoic units (see LePain and others, 2013), as volcanic arc activity to the west of the forearc basin waned or ceased during the late Paleogene and early Neogene (Finzel and others, 2015; Helmold and others, 2018). As a result, absolute age control for most of the units remains sparse.

### West Foreland Formation (Twf) (MDAs 47.0 ± 1.1–38.1 ± 1.0 Ma)

The 24 West Foreland geochronologic results presented in this report from samples collected throughout the unit establish the age of margin-proximal deposition between ca. 47.0 and 38.1 Ma. The base of the West Foreland Formation (Twfl) is exposed at two locations—near Straight Creek and along the north-facing slope immediately south of Capps Glacier (fig. 4)—where it unconformably overlies and is in local fault contact with Late Cretaceous altered volcanic rocks (unit Ku; LePain and others, 2013, unit Kv; Gillis and others, in preparation; this report). Twfl generally lacks contemporaneous volcanic interbeds or co-eruptive detrital grains, and only a single sample from this subunit (fig. 5; table 2; app. G1) produced results that approximate its stratigraphic age. This volcaniclastic sandstone collected from a measured stratigraphic section 22.5 meters above the unconformable contact with unit Kv produced a maximum stratigraphic age (MDA) of 47.0 ± 1.1 Ma that constrains the oldest strata of the succession to middle Eocene. The lower several meters of the section are composed entirely of metavolcanic clasts derived from the underlying Kv, which produced a zircon U–Pb age of 77.3 ± 1.8 Ma (table 1; app. F5). This is one of two known locations in the upper Cook Inlet region where Cenozoic strata are observed in stratigraphic contact with pre-Cenozoic basin floor lithologies. A similar relationship occurs approximately 4 km along strike to the northeast near Capps Glacier. These West Foreland exposures are therefore the oldest known strata of Cenozoic Cook Inlet forearc basin fill in the region (fig. 9). Common volcanic and subordinate granitic clasts from texturally immature, proximal alluvial fan conglomerates in the Twfl produced zircon U–Pb dates of 102.9 ± 2.4 Ma, 97.7 ± 2.2 Ma, and 55.7 ± 1.3 Ma (table 3; apps. G35–G37).

Intercalated, generally reworked tephras are common in the middle unit of the West Foreland Formation (Twfm). However, the subunit is principally dominated by thick pebble-cobble conglomerates and thick, poorly sorted, massive to crudely laminated, volcaniclastic sandstones (LePain and others, 2013). The tephras range from decimeter- to multi-meter thick and commonly include pebble-sized pumiceous clasts in a very fine-grained matrix. Biotite and white feldspar crystals are locally recognizable in hand samples. Seven of nine tuffaceous samples analyzed from

**Table 2.** Zircon U-Pb and $^{40}Ar/^{39}Ar$ results for West Foreland Formation and Kenai Group strata.

| Sample # | Location | Unit | Lithology | App. # | Analysis type | Mineral | Preferred analysis date ± 2σ uncertainty (Ma) | MSWD | PoF | n | Criteria | Comment | Inferred crystallization/ cooling/maximum depositional age ± 2σ (Ma) |
|---|---|---|---|---|---|---|---|---|---|---|---|---|---|
| **Beluga Formation** | | | | | | | | | | | | | |
| 09JRM100-20.0 | Chuitna River | Tb | Siltstone(?) | G32 | U-Pb | Zircon | 9.7 ± 2.1 | — | — | 1 | YSG | Maximum depositional age (with caution) | ~9.7 |
| 08JRM204 | Beluga River | Tb | Not recorded, likely tephra | G31 | U-Pb | Zircon | 11.3 ± 0.4 | 1.02 | 0.43 | 16 | YSP | Maximum depositional age | 11.3 ± 0.4 |
| **Tyonek Formation** | | | | | | | | | | | | | |
| 08DL055-109.0 | Beluga River | Tt | Tonstein | G30 | U-Pb | Zircon | 15.2 ± 0.4 | 0.93 | 0.56 | 24 | WM | Stratigraphic age | 15.2 ± 0.4 |
| 09DL029-7.0a | Beluga River | Tt | Tephra clast | G29 | U-Pb | Zircon | 15.9 ± 0.5 | 0.79 | 0.79 | 31 | YC2σ | Maximum depositional age. Youngest grain omitted (see Appendix H29) | 15.9 ± 0.5 |
| 11BG145 | Beluga River | Tt | Tonstein | G28 | $^{40}Ar/^{39}Ar$ | Glass | 23.6 ± 2.8 | 1.04 | Not calc. | 12 | Inv. isochron | Questionable stratigraphic age | 23.6 ± 2.8 |
| 11DJM071a | Beluga River | Tt | Tonstein | G27 | $^{40}Ar/^{39}Ar$ | Glass | 28.4 ± 8.2 | 1.09 | Not calc. | 11 | Inv. isochron | Exceeds U-Pb maximum depositional date from same bed | 28.4 ± 8.2 |
| 10BG409d | Beluga River | Tt | Tonstein | G26 | $^{40}Ar/^{39}Ar$ | Glass | 28.8 ± 1.0 | 0.23 | Not calc. | 6 | Plateau | Questionable stratigraphic age | 28.8 ± 1.0 |
| **West Foreland Formation in Approximate Stratigraphic Order** | | | | | | | | | | | | | |
| 08BG218a | Beluga River | Twfu | Volcaniclastic lithology | G25 | U-Pb | Zircon | 38.1 ± 1.0 | 0.95 | 0.45 | 6 | YSP | Maximum depositional age | 38.1 ± 1.0 |
| 08BG215a | Chakachatna River | Twfu | Reworked crystal-lithic tuff | G24 | U-Pb | Zircon | 38.3 ± 0.9 | 0.96 | 0.51 | 20 | YSP | Maximum depositional age | 38.3 ± 0.9 |
| 08BG199a | Scarp Creek | Twfu | Reworked crystal-lithic tuff | G23 | U-Pb | Zircon | 38.5 ± 0.9 | 1.01 | 0.44 | 12 | YSP | Maximum depositional age | 38.5 ± 0.9 |
| 10TMH243a | Olson Creek | Twfu | Reworked(?) tephra | G22 | U-Pb | Zircon | 39.4 ± 0.9 | 1.00 | 0.48 | 90 | YSP | Maximum depositional age | 39.4 ± 0.9 |
| 08BG229a | Capps Glacier-Straight Creek area | Twfu | Volcaniclastic sandstone | G21 | U-Pb | Zircon | 40.7 ± 1.2 | 1.65 | 0.10 | 9 | YC2σ | Maximum depositional age | 40.7 ± 1.2 |
| 08BG227a | Capps Glacier-Straight Creek area | Twfu | Reworked tephra | G20 | U-Pb | Zircon | 42.2 ± 1.0 | 0.95 | 0.52 | 17 | YSP | Maximum depositional age | 42.24 ± 1.44 |
| 08EF004 | Capps Glacier area | Twfu | Tuffaceous sandstone | G19 | U-Pb | Zircon | 42.8 ±2.8 | 0.05 | 0.82 | 2 | YSP | Maximum depositional age | 42.5 ± 3.5 |
| 09DL030-20.8 | Capps Glacier-Straight Creek area (screamer cr.) | Twfu | Reworked tephra | G18 | U-Pb | Zircon | 43.1 ± 1.3 | 0.80 | 0.55 | 6 | YC2σ | Maximum depositional age | 43.1 ± 1.3 |
| 08DL056-11.8b | Capps Glacier-Straight Creek area | Twfm/ Twfu | Volcaniclastic sandstone | G17 | U-Pb | Zircon | 44.8 ± 1.7 | 0.36 | 0.78 | 4 | YC2σ | Maximum depositional age | 44.8 ± 1.7 |
| 08DL056-1.7 | Capps Glacier-Straight Creek area | Twfm/ Twfu | Volcaniclastic sandstone | G16 | U-Pb | Zircon | 42.9 ± 1.2 | 0.65 | 0.75 | 10 | YC2σ | Maximum depositional age | 42.9 ± 1.2 |
| 08DL056-0.3 | Capps Glacier-Straight Creek area | Twfm/ Twfu | Volcaniclastic sandstone | G15 | U-Pb | Zircon | 43.5 ± 0.9 | 1.00 | 0.48 | 56 | YSP | Maximum depositional age | 43.5 ± 0.9 |
| 09DL027-11.1a | Capps Glacier area | Twfm | Tuffaceous sandstone | G14 | U-Pb | Zircon | 43.9 ± 2.7 | — | — | 1 | YSG | Maximum depositional age | 43.9 ± 2.7 |
| 08BG193A | Capps Glacier-Straight Creek area | Twfm | Reworked tephra | G13 | U-Pb | Zircon | 42.4 ± 1.0 | 0.87 | 0.59 | 14 | YSP | Maximum depositional age | 42.4 ± 1.0 |
| 08DL057-37.5ba | Capps Glacier-Straight Creek area | Twfm | Reworked tephra | G12 | U-Pb | Zircon | 41.8 ± 9.4 | 1.05 | 0.31 | 2 | YSP | Maximum depositional age | 41.8 ± 9.4 |

**Table 2, continued.** Zircon U-Pb and $^{40}Ar/^{39}Ar$ results for West Foreland Formation and Kenai Group strata.

| Sample # | Location | Unit | Lithology | App. # | Analysis type | Mineral | Preferred analysis date ± 2σ uncertainty (Ma) | MSWD | PoF | n | Criteria | Comment | Inferred crystallization/ cooling/maximum depositional age ± 2σ (Ma) |
|---|---|---|---|---|---|---|---|---|---|---|---|---|---|
| 09DL028-28.5aa | Capps Glacier area | Twfm | Reworked tephra | G11 | U-Pb | Zircon | 44.0 ± 1.5 | 0.51 | 0.60 | 3 | YC2σ | Maximum depositional age | 44.0 ± 1.5 |
| 08MAW213-32.5a | Capps Glacier-Straight Creek area | Twfm | Silicified reworked tephra | G10 | U-Pb | Zircon | 43.7 ± 6.4 | 2.89 | 0.06 | 3 | YC2σ | Maximum depositional age | 43.7 ± 6.4 |
| 08MAW213-1.25a | Capps Glacier-Straight Creek area | Twfm | Silicified reworked tephra | G9 | U-Pb | Zircon | 43.4 ± 1.8 | 1.17 | 0.32 | 6 | YSP | Maximum depositional age | 43.4 ± 1.8 |
| 07DL080-72.9 | Capps Glacier area | Twfm | Reworked tephra | G8 | U-Pb | Zircon | 41.1 ± 1.0 | 0.92 | 0.47 | 6 | YSP | Maximum depositional age | 41.1 ± 1.0 |
| 07DL080-72.8 | Capps Glacier area | Twfm | Reworked tephra | G7 | $^{40}Ar/^{39}Ar$ | Glass | 57.8 ± 5.6 | 0.70 | Not calc. | 7 | Plateau | Not geologically meaningful due to open-system behavior (excess argon) | — |
| 07DL080-67.5 | Capps Glacier area | Twfm | Reworked tephra | G6 | U-Pb | Zircon | 43.0 ± 1.0 | 0.94 | 0.54 | 25 | YSP | Maximum depositional age | 43.0 ± 1.0 |
| | | | | G5 | $^{40}Ar/^{39}Ar$ | Plagioclase | 44.1 ± 3.6 | 0.80 | Not calc. | 9 | Plateau | Approximate stratigraphic age consistent with zircon U-Pb date | |
| | | | | | $^{40}Ar/^{39}Ar$ | Glass | 34.8 ± 19.6 | — | — | — | Integrated | Not geologically meaningful due to open-system behavior | |
| 07DL080-4.2 | Capps Glacier area | Twfm | Bentonite | G4 | U-Pb | Zircon | 41.9 ± 1.0 | 0.87 | 0.59 | 15 | YSP | Maximum depositional age | 41.9 ± 1.0 |
| | | | | G3 | $^{40}Ar/^{39}Ar$ | Hornblende | 43.0 ± 5.2 | 0.03 | Not calc. | 2 | Plateau | "Pseudo" plateau age | |
| | | | | | $^{40}Ar/^{39}Ar$ | Plagioclase | 43.3 ± 3.2 | 0.70 | Not calc. | 4 | Plateau | Approximate stratigraphic date, overlaps zircon YSP date | |
| | | | | | $^{40}Ar/^{39}Ar$ | Glass | 4.4 ± 77.8 | — | — | — | Integrated | Not geologically meaningful due to open-system behavior | |
| 08DL054-1.7 | Capps Glacier-Straight Creek area | Twfm | Pumaceous sandstone | G2 | U-Pb | Zircon | 42.1 ± 1.2 | 0.23 | 0.97 | 7 | YC2σ | Maximum depositional age | 42.1 ± 1.2 |
| 08DL053-22.5b | Capps Glacier-Straight Creek area | Twfl | Volcaniclastic sandstone | G1 | U-Pb | Zircon | 47.0 ± 1.1 | 1.01 | 0.46 | 36 | YSP | Maximum depositional age | 47.0 ± 1.1 |

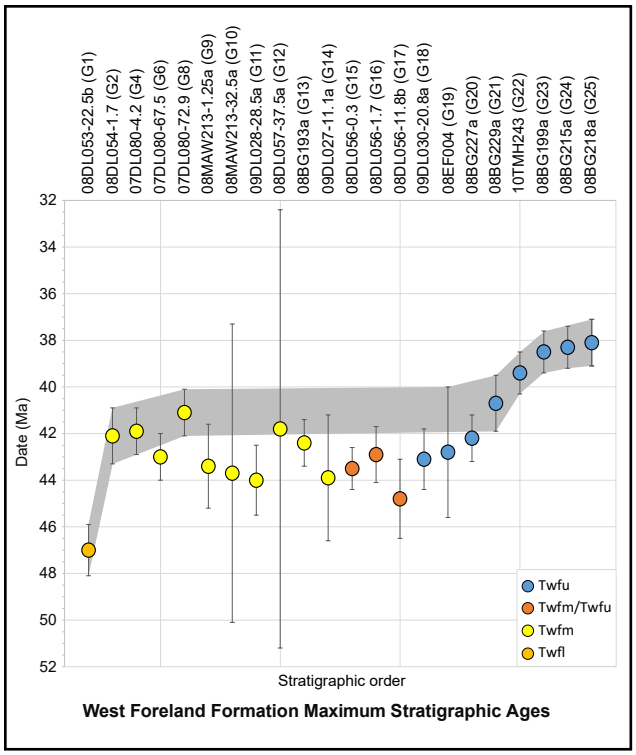


**Figure 9.** West Foreland maximum stratigraphic ages (MDAs). Colored circles with error bars represent MDA categorized by subunit. The gray-shaded region encompasses the generalized range of permissible dates based on: the MDA uncertainty, measured or inferred stratigraphic order, and Law of Superposition. Note the restricted, less than 2 My timeframe within which much of the unit was deposited.

the middle subunit contained large proportions of detrital grains and produced a relatively wide range of middle Eocene MDAs (see also sample CB-13; Finzel and others, 2016). Nevertheless, two samples collected from low in the middle subunit produce relatively high-n youngest statistical populations (YSP) that are consistent with deposition within a narrow window of 42.1 ± 1.2–41.1 ± 1.0 Ma (fig. 9; table 2; apps. G3–G13). Two granitic clasts collected from Twfm yielded zircon U–Pb dates of 60.0 ± 1.4 Ma, and 58.5 ± 1.3 Ma (table 3; apps. G39 and G39).

U–Pb constraints improve higher in the succession, where abundant, less extensively reworked, thick tephra beds characterize the upper subunit (Twfu). Twfu consists of abundant, interbedded, cross-stratified sandstones and pebble conglomerates, and is interpreted as recording a mix of lahar (volcano-hydrologic events in the sense of Smith and Lowe, 1991) and dilute stream flow processes (LePain and others, 2013). Tephra samples collected across the study area from the upper subunit often produce relatively high-n YSPs yielding a restricted range of MDAs of ca. 40.7 ± 1.2–38.1 ± 1.0 Ma (fig. 9; table 2; apps. G21–G25). The proximity of the youngest sample to the gradational contact with the overlying Hemlock Conglomerate suggests that it provides a reasonable approximation for the upper age of the West Foreland Formation.

## Hemlock Conglomerate (Th) (Middle Eocene to Early or Middle[?] Miocene)

Stratigraphic age constraints for the Hemlock Conglomerate cropping out on the west side of the CIB are based principally on palynomorph assemblages (Zippi and others, 2021) because no primary volcanic material has been observed in these strata. Results from samples collected along the Beluga and Theodore River drainages and Chuit Creek (figs. 3 and 4) constrain the strata as middle to late Eocene, rendering them the oldest documented Hemlock Conglomerate in the basin. The results are consistent with a youngest single grain (YSG) detrital zircon date of 44.4 ± 0.7 Ma (1σ uncertainty) from these strata cropping out in the Theodore River drainage (Finzel and others, 2016). Minor yet distinctive flow-banded volcanic clasts observed only at the Beluga and Theodore Rivers outcrops produce zircon U–Pb and whole rock $^{40}Ar/^{39}Ar$ dates of 55.7 ± 0.6 and 55.4 ± 1.3 Ma, respectively (table 3; apps. G43 and G44). A third igneous clast yielded a zircon U–Pb date of 61.6 ± 1.5 Ma (table 3; app. G42).

## Tyonek Formation (Tt) (Late Eocene to Late-Middle Miocene)

Primary volcanic material is rare in the Tyonek Formation but is locally present as thin tonsteins in coal seams (e.g., Triplehorn and others, 1977). Thus, recent stratigraphic age constraints for this unit are principally interpreted from results of extensive

**Table 3.** Zircon U-Pb and $^{40}Ar/^{39}Ar$ results for detrital samples and Kaloa deposits.

| Sample # | Location | Unit | Lithology | App. # | Analysis type | Mineral | Preferred analysis date ± 2σ uncertainty (Ma) | Criteria | Comment |
|---|---|---|---|---|---|---|---|---|---|
| **Detrital Samples** | | | | | | | | | |
| 10BG405a | Beluga River | Tb | Granitic clast | G48 | U-Pb | Zircon | 57.1 ± 1.3 | YSP | Provenance age |
| 10BG405b | Beluga River | Tb | Granitic clast | G47 | U-Pb | Zircon | 63.2 ± 1.4 | YSP | Provenance age |
| 10BG405c | Beluga River | Tb | Granitic clast | G46 | U-Pb | Zircon | 63.1 ± 1.4 | YSP | Provenance age |
| 08DL055-15.95 | Beluga River | Tt | Tephra clast | G45 | U-Pb | Zircon | 33.9 ± 0.9 | YSP | Provenance age |
| 10TMH208a | Beluga River | Th | Flow-banded rhyolite clast | G44 | $^{40}Ar/^{39}Ar$ | Whole rock | 55.7 ± 0.6 | Plateau | Provenance age |
| 07DL073-4.0d | Theodore River | Th | Igneous clast | G43 | U-Pb | Zircon | 55.4 ± 1.3 | YSP | Provenance age |
| 07DL073-4.0j | Theodore River | Th | Igneous clast | G42 | U-Pb | Zircon | 61.6 ± 1.5 | YC2σ | Provenance age |
| 08BG224a | Capps Glacier area | Twfu | Tuffaceous sandstone | G41 | U-Pb | Zircon | — | — | Provenance |
| 08DL056-27.5b | Capps Glacier area | Twfm | Tuffaceous sandstone | G40 | U-Pb | Zircon | — | — | Provenance |
| 07DL080-27.1a | Capps Glacier area | Twfm | Igneous clast | G39 | U-Pb | Zircon | 58.5 ± 1.3 | YSP | Provenance age |
| 07DL080-12.0a | Capps Glacier area | Twfm | Granitic clast | G38 | U-Pb | Zircon | 60.0 ± 1.4 | YSP | Provenance age |
| 08DL053-23.4b | Capps Glacier-Straight Creek area | Twfl | Igneous clast | G37 | U-Pb | Zircon | 55.7 ± 1.3 | YSP | Provenance age. Youngest grain omitted (see Appendix H37) |
| 08DL053-23.4a | Capps Glacier-Straight Creek area | Twfl | Igneous clast | G36 | U-Pb | Zircon | 102.9 ± 2.4 | YSP | Provenance age |
| 07DL083-0.0a | Capps Glacier area | Twfl | Igneous clast | G35 | U-Pb | Zircon | 97.7 ± 2.2 | YSP | Provenance age within a few m of Kv contact |
| **Kaloa Samples** | | | | | | | | | |
| 07DL076b | Granite Point | Qgl | Bentonite | G34 | U-Pb | Zircon | 37.5 ± 0.9 | YC2σ | Maximum depositional age of bed within allochthonous block |
| | | | | G33 | $^{40}Ar/^{39}Ar$ | Hornblende | 76.6 ± 1.4 | Integrated | Allochthonous, open system behavior |
| | | | | | $^{40}Ar/^{39}Ar$ | Plagioclase | 39.7 ± 2.8 | Inv. isochron | Allochthonous, stratigraphic age of bed |
| | | | | | | Glass | 19.2 ± 1.8 | Plateau | Allochthonous, open system behavior |

palynologic sampling (Zippi and Loveland, 2012; Zippi and others, 2021). The palynologic age calls are supported by an early-middle Miocene zircon U–Pb MDA (15.9 ± 0.5) and primary airfall date of a tonstein (15.2 ± 0.4; Apps. G29 and G30). These U–Pb dates constrain a composite measured section along the Beluga River (fig. 4) of which section 08DL055 documents the upper 109 meters. The section also produced several high-confidence middle Miocene palynology age determinations. The zircon dates are indistinguishable from two plagioclase K-Ar ages of tonsteins (15.8 ± 1.8 and 15.9 ± 1.5 Ma) from a Tyonek outcrop on the Chuitna River, approximately 15 km to the west (fig. 4), which corresponds to the type section for the Seldovian floral stage (Wolfe and others, 1966; Turner and others, 1980). Palynomorphs from the Chuitna outcrop and numerous Tyonek exposures toward Capps Glacier (fig. 4) also produce middle Miocene stratigraphic ages (Zippi and Loveland, 2012; Zippi and others, 2021). A tephra clast collected from near the base of 08DL055 yielded an uncommon zircon U–Pb date of 33.9 ± 0.9 Ma (table 3; app. G45).

$^{40}Ar/^{39}Ar$ analyses of volcanic glass from Tyonek Formation tonsteins collected along the Beluga River (fig. 4) produce less reliable results that directly conflict with the palynologic and zircon U–Pb results from the same stratigraphic successions. For instance, one sample yielded a middle Oligocene $^{40}Ar/^{39}Ar$ date of 28.8 ± 1.0 Ma (table 2; app. G26), whereas a palynologic sample collected approximately 1 m below the tonstein produced a moderate-confidence early Miocene age (09BG409a, Zippi and others, 2021). Similarly, an $^{40}Ar/^{39}Ar$ glass date of a thick marker coal bed on the northeast bluff overlooking the Beluga River (28.4 ± 8.2 Ma; table 2; app. G27) is over 10 m.y. older than a zircon U–Pb analysis of the same tonstein collected over 2 km away (15.2 ± 0.4 Ma; table 2; app. G30). Palynologic results for samples collected from a mudrock interval beneath the coal near both locations produced moderate- to high-confidence middle Miocene age determinations (samples 08DL055-101.0 and 10DJM072a, Zippi and others, 2021), casting doubt on the validity of the middle to late Oligocene $^{40}Ar/^{39}Ar$ date. In light of the contradiction between the glass $^{40}Ar/^{39}Ar$ results and the complementary palynologic and zircon U–Pb ages, the glass ages are deemed unreliable—presumably due to open-system behavior and uptake of excess argon during devitrification (e.g., Fleck and others, 1977). Particularly problematic is that for one sample (app. G26), the age spectra suggest systematic argon loss, not gain, highlighting the need for independent age control when assessing the argon data for glass. Another tonstein volcanic glass date of 23.6 ± 2.8 Ma (table 2; app. G28) from an approximately 1 m-thick coal in structurally complex lower Tyonek or upper Hemlock strata exposed a few hundred meters southeast the Castle Mountain fault (fig. 4) suggests that the transitional strata are Oligo-Miocene in age. Unlike other glass dates in the area that exhibit open-system behavior, the inverse isochron from this sample indicates only an atmospheric component of initial argon ($^{40}Ar/^{36}Ar_i$ = 294.3 ± 2.9), and thus no evidence of extraneous argon retention that would produce an artificially older date. The result is nearly 8 m.y. older than nearby Tyonek zircon U–Pb dates yet younger than quartzose sandstones exposed in the Lewis River drainage along strike to the northeast (fig. 3) and mapped by Magoon and others (1976) as Tyonek Formation. Strata there yielded palynomorphs and a detrital zircon MDA that suggest a late Eocene age (Enkelmann and others, 2019; Zippi and others, 2021). Thus, sedimentary facies most closely associated with Tyonek Formation strata locally vary widely in age from late Eocene to late-middle Miocene.

### Beluga Formation (Tb) (Middle to Late Miocene)

As with the Tyonek Formation, the Beluga Formation is generally non-volcanogenic on the northwest side of the basin, and reliable geochronologic age control there has been lacking. Recent palynologic results for Beluga Formation outcrops on the Beluga and Chuitna Rivers (fig. 4) restrict their ages to late Miocene (Zippi and Loveland, 2012; Zippi

and others, 2021). Two new zircon U–Pb dates from probable intercalated ash layers collected from outcrops in both drainages constrain the strata to no older than middle Miocene. On the Chuitna River, a sample collected from a measured stratigraphic section yielded an YSG of 9.7 ± 2.1 Ma (table 2; app. G32). This YSG date conforms with more reliably dated Beluga Formation outcrops nearer the basin axis on the Kenai Peninsula (Triplehorn and others, 1977; Turner and others, 1980; Dallegge and Layer, 2004) and with results of high-resolution palynologic sampling of the same section (n=27) that produced a stratigraphically consistent suite of early-late to late Miocene high-confidence age determinations (Mongrain, 2012; Zippi and others, 2021). The date also overlaps (within analytical uncertainty) another YSG MDA of 10.5 ± 0.5 Ma (1σ uncertainty) from the Chuitna River (Finzel and other, 2016) and a YSP determination of 11.3 ± 0.4 Ma (table 2; app. G31) from a probable tephra collected along the Beluga River within a few tens of meters of the inferred unconformable contact between the Beluga Formation and overlaying Sterling Formation. Several palynologic age determinations from the same Beluga River outcrop yielded consistent early late Miocene results with high confidence (Zippi and others, 2021). Nevertheless, YSG determinations are prone to underestimating the age of a stratigraphic succession (Spencer and others, 2016; Coutts and others, 2019; Herriott and others, 2019), so caution should be exercised when interpreting the ca. 9.7 Ma MDA. Three granitic clasts collected at the Beluga River location produced zircon U–Pb dates of 63.1 ± 1.4 Ma, 63.2 ± 1.4 Ma, and 57.1 ± 1.3 Ma (table 3; apps. G46–G48).

### Sterling Formation (Ts) (Latest Miocene to Early Pliocene)

The Sterling Formation has recently been identified in outcrop along the Beluga River (fig. 4) where its depositional contact with the underlying Beluga Formation is mapped along a vertical bluff using surface lithological observations and publicly available and privately held seismic data (Gillis and others, 2017). A single palynologic result from a nearby outcrop produced an age determination of latest Miocene to early Pliocene with moderate confidence (Zippi and others, 2021). The result is consistent with dates from core material recovered from the nearby Beluga River Unit #212-24 well. The material was collected from an interval identified as Sterling Formation by the unit operator (Phillips Alaska, Inc.) and produced $^{40}Ar/^{39}Ar$ ages of 6.85 ± 0.90 and 6.24 ± 0.37 Ma (Dallegge and Layer, 2004).

### Kaloa Beds (Granite Point)

Complex stratigraphic associations are observed at an outcrop along a coastal bluff near Granite Point (fig. 3). At this locality, large blocks of Miocene rocks are incorporated into tilted Quaternary glacial deposits. The Quaternary beds have been variously interpreted as glacial moraine (Schmoll and others, 1984) or glacio-estuarine deposits (Reger, 2009) that envelop large, detached blocks of middle Miocene strata (Haeussler and others, 2000). Reger (2009) interpreted the allochthonous bodies as submarine slide blocks of Beluga Formation strata sourced from the flank of the growing Granite Point anticline located approximately 2.5 km offshore to the southeast. However, a newly recognized sliver of middle Eocene West Foreland Formation strata (sample 07DL076b, zircon U–Pb YC2σ = 37.5 ± 0.9 Ma; table 3; app. G34) is structurally intercalated with the late Miocene allochthonous blocks and complicates this interpretation. Uppermost West Foreland Formation occurs at approximately 3,720 m measured depth in the core of the anticline (Tyonek State #2, American Stratigraphic Company, unpublished), precluding the hypothesis of a mass wasting source from the southeast. The closest West Foreland Formation strata exposed at the surface in the region are 25–35 km inland toward the northwest from the coastal bluff location (see Gillis and others, 2017). These West Foreland outcrops are most notable at the glacially carved margin of the Chakachatna drainage, which debouches near Granite Point. The southernmost West Foreland Formation outcrop exposed along the drainage margin produced a YSP of 38.3 ± 0.9 Ma (table 3; app. G24), which

is indistinguishable within uncertainty to the MDA of the allochthonous block strata. Early(?) to Late Miocene Tyonek Formation and middle to Late Miocene Beluga Formation strata also occur in the bluffs overlooking the drainage. In light of the new geochronologic data, our preferred interpretation is that structurally interleaved Beluga and West Foreland formations slumped onto the glacier from the over-steepened valley wall of the Chakachatna drainage. The blocks of Cenozoic strata were subsequently transported basinward to the Granite Point area and deposited offshore as large drop blocks at the terminus of the tidewater glacier, where they were incorporated into Quaternary diamicton.

## Detrital Zircon Date Distributions

Determining depositional ages for Cook Inlet basin strata was the principal goal for their zircon U–Pb analyses, yet dates of detrital zircons present in most of the samples provide important information about sediment source area(s) as well. We use the detrital dates to supplement detailed detrital zircon provenance work by Finzel and others (2015, 2016) and Enkelmann and others (2019) to refine the permissible sediment sources to the West Foreland Formation. Most of the geochronologic samples analyzed for stratigraphic age control reported here are not generally recognized as primary airfall tephra material, but often consist of re-transported ash in probable lahar deposits (LePain and others, 2013). Often, the majority of grains (up to 98 percent) analyzed from each formation are recognized as detrital. Most of the detrital zircon dates cluster into groups that coincide with ages of bedrock commonly exposed near the margins of the forearc basin (e.g., Wilson and others, 2012). Fewer grains match ages of bedrock exposed distal to the basin or zircons recycled from nearby Mesozoic strata (fig. 10A).

Samples to be characterized for their detrital constituency typically require a minimum of 95 individual grain analyses to achieve a 95 percent probability of identifying all grain fractions that represent ≥5 percent of the complete grain date distribution (Vermeesch, 2004). Analyses of our tephra samples consist of 25–115 grains with the primary goal of establishing their eruptive ages (assuming a high yield of co-genetic volcanic zircons), which requires fewer dates. Nevertheless, we take advantage of important yet incomplete detrital information from our samples and circumvent the shortcomings of their low individual numbers of analyses by compositing 825 pre-middle Eocene dates from 25 samples collected throughout the West Foreland succession to construct an integrated detrital zircon date distribution for the entire unit. Recent research has demonstrated that high-count analyses (300 or more grains/sample) are most successful at capturing small but potentially important grain date populations that could be missed by lower-count protocols—particularly when attempting to establish maximum depositional ages (MDAs) of sampled strata with low quantities of syn-eruptive grains (Pullen and others, 2014; Coutts and others, 2019). The high-count method is also better suited to characterizing the relative abundance of grain date populations. Comparison of the composite West Foreland age distribution (n=825) to a high-count detrital zircon sample (n=306) collected from the middle West Foreland Formation by Capps Glacier (fig. 10B; sample CB-13; Finzel and others, 2016) reveals that compositing smaller numbers of zircons per sample over a greater stratigraphic interval captured a greater diversity of grain date populations than did a high-count analysis from a single outcrop. Whereas individual samples with low count analyses do not accurately document spatial and temporal variability in detrital zircon date compositions throughout the succession, these results demonstrate that a composite of such analyses for dynamic depositional systems provides a better understanding of sediment provenance for the unit as a whole than do high-count single-location analyses.

### West Foreland Formation (Twf)

West Foreland strata produce detrital zircon concentrations at ca. 56–68 Ma, ca. 78–85, and ca. 96–107 Ma separated by a regular but less dense array of dates (fig. 10A). Mesozoic grains concentrated at ca. 174–206 Ma comprise only 2 percent of the zircon extracted from West Foreland Forma-

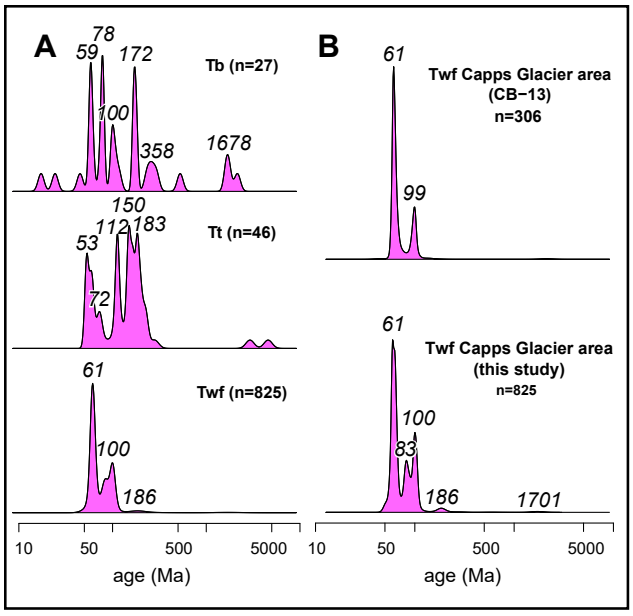


**Figure 10. A.** Kernel density estimates (KDE) of detrital zircons from the West Foreland (Twf), Tyonek (Tt), and Beluga (Tb) formation samples analyzed for this study. Y-axis = date density. X-axis = dates plotted on logarithmic scale. All zircons of West Foreland Formation age (<ca. 47 Ma) were omitted from the Twf KDEs to highlight the unit's non-syndepositional grain dates. Only the West Foreland Formation results are discussed at length for their sediment provenance implications (see text). **B.** KDE comparison of detrital zircon results from a single, high-count analysis of a West Foreland sample collected near Capps Glacier (Finzel and others, 2016), and a multi-sample composite from throughout the stratigraphic succession (this study). Dates plotted on log scale. Note that the composite KDE produces a slightly more complex curve than the single high-count analysis, indicating that it more completely reproduces the age distribution of the unit as a whole (see text for discussion).

tion rocks (fig. 10A), and Paleozoic and Precambrian zircons are very rare. Paleozoic grains constitute only 0.2 percent of the total zircons extracted from West Foreland lithologies, and Precambrian grains constitute slightly more at 0.7 percent (fig. 10A). Paleoproterozoic zircon ages group between 1,637 and 1,807 Ma.

### Tyonek and Beluga Formations (Tt and Tb)

Unlike results from the West Foreland Formation, detrital zircon age spectra from the Tyonek (n=46, N=1) and Beluga (n=27, N=1) formations are incomplete due to their low number of analyses (fig. 10A). The Tyonek Formation sample (09DL029-7.0a) yields age groupings at ca. 51–62 Ma, ca. 71–76 Ma, ca. 109–113 Ma, and more diffuse groups of dates between ca. 144 and 170 Ma and ca. 180 and 203 Ma. Similarly, the Beluga Formation sample produces clusters of ages at ca. 56–62 Ma, ca. 73–81 Ma, ca. 98–106 Ma, and ca. 167–180 Ma. Three Beluga Paleoproterozoic dates range from ca. 1627 to 2144 Ma. Three granitic clasts from an upper Beluga Formation outcrop on the Beluga River yielded zircon U–Pb crystallization ages of ca. 63.2, ca. 63.1, and ca. 57.1 Ma. Although many of the major age peaks are likely present, the relative zircon date abundances are certainly misrepresented (see Finzel and others, 2016 for comparison).

## DISCUSSION

### Igneous Crystallization and Chemistry

Zircon U–Pb and hornblende $^{40}Ar/^{39}Ar$ dates reported here from the eastern Neacola and southeastern Tordrillo mountains, and southwestern Susitna basin compliment results from an extensive reconnaissance potassium-argon (K–Ar) study of the Aleutian–Alaska Range during the late 1960s and early 1970s (Reed and Lanphere, 1969, 1972) and a more recent compilation of latest Cretaceous–Cenozoic igneous rock dates in Alaska (Moll-Stalcup, 1994) that identify major magmatic flare-ups from the Middle Jurassic to mid-Cenozoic[1]. Reported age ranges for middle Cretaceous to Cenozoic Alaska-Aleutian Range magmatism vary between studies, but episodes of punctuated arc activity are typically recognized from ca. 100 to 88 Ma, ca. 75 to 66 Ma, ca. 63 to 55 Ma, and ca. 43 to 37 Ma (Reed and Lanphere, 1973; Moll-Stalcup, 1994; Hart and others, 2004; Graham and others, 2013).

We group the plutonic rocks in the field area into 4 suites based on their chemistry and age. Major oxide and trace element analyses of igneous

[1]A large zircon U-Pb and $^{40}Ar/^{39}Ar$ dataset from the western Alaska Range including results from the Tordrillo and Neacola mountains was published in Jones and others (2020) as this paper went to press. See References for a complete citation.

rocks from throughout the area (app. J; Freeman and others, 2016) include many of the same samples dated for this study. The plutonic rocks exhibit a broad trend from intermediate to felsic compositions correlated with time (fig. 11). Intrusive suites classified by total alkali versus silica (Wilson, 1989) include ca. 84–77 Ma diorite, ca. 74–71 Ma granodiorite to diorite with minor gabbro, ca. 69–65 Ma granodiorite to granite, and ca. 62–56 Ma granite to granodiorite (fig. 11A). Volcanic rocks and dikes have mafic to intermediate compositions and are divided into three groups based on their potassium and sodium to silica ratios (fig. 11B) following LeBas and others (1986) and Peccerillo and Taylor (1976). They include late Paleocene basaltic andesite to andesite dikes (ca. 58.6–56.8 Ma) and undated basaltic dikes, a shoshonitic flow, and peperite.

Ca. 84–77 Ma diorites composing Lone Ridge are the oldest igneous rocks exposed in the area. The fault-bounded body is calc-alkalic, magnesian, and metaluminous (figs 11A, C–E). The rocks commonly have incompatible element concentrations that suggest a magmatic arc genesis (fig. 12A; Pearce and others, 1984), although several exhibit marginal adakite-like Sr/Y compositions (fig. 12B). Virtually all ca. 74–71 Ma intrusive rocks are restricted to the southeast block of the Lake Clark fault (LCF) in the Neacola Mountains and produce the broadest range of $SiO_2$/differentiation of the igneous suites analyzed. As with the Lone Ridge diorites, they are magnesian and metaluminous, with a modified alkali-lime index that ranges from calc-alkalic to calcic (Frost and others, 2001). The ca. 69–65 Ma granitoids are found exclusively on the north side of the LCF in the study area and are entirely peraluminous (fig. 11D). Most possess elevated Sr/Y ratios that plot firmly in the adakite field (fig. 12B), perhaps indicating collisional genesis (Todd and Jones, 2017; Cole and Chung, 2013). The Paleocene granodiorites and granites (ca. 62–56 Ma) of the Tordrillo Mountains array along a linear trend with respect to silica in most major element plots and are metaluminous to peraluminous (figs. 12A, C–E). Their calc-alkalic signatures and trace element compositions (figs. 12E and 13A, B) are typical of Cordilleran-type magmatic arc granitoids (fig. 12A; Frost and others, 2001).

Basaltic andesite to andesite dikes intrude the late Paleocene Capps granite in a systematic east-west subvertical orientation, many along what are interpreted as transtensional synthetic Riedel shears to the dextral-normal Capps Glacier fault (Gillis and others, 2009, 2017). Similar in composition to the granite phase of the pluton, they are calc-alkalic, magnesian, and metaluminous (fig. 11B–E) with a trace element composition consistent with magmatic arc genesis (fig. 12C). However, one of the two samples from this group has elevated Nb and Zr, suggesting a within-plate component or zircon accumulation (figs. 12C, D; Whalen and others, 1987). Undated basaltic dikes that intrude the ca. 84–77 Ma diorite at Lone Ridge are distinctive; their geochemistry is sub-alkalic, yet ferroan. Unlike the magmatic arc signatures of the granitoids detailed above, this group has a clear within-plate chemical signature suggesting emplacement during crustal extension. Undated shoshonites within volcaniclastic strata have significantly different chemical signatures from other igneous rocks in the region. They are the only alkalic group rocks (fig. 11B, E) with very high potassium (up to 8.8 percent), strontium (near 2000 ppm), and barium (up to 2700 ppm) concentrations (figs. 11B, E, 12B). The volcaniclastic strata are intruded by the Capps granite, and are therefore older than ca. 56 Ma. The youngest plausible detrital zircon date from a nearby sample is ca. 61.1 Ma, tentatively suggesting these rocks constitute the volcanic ediface of the Capps granite. Although the petrogenetic and tectonic significance of shoshonitic rocks have yet to be resolved, they are known to originate in subduction settings that are modified by post-orogenic extension, and/or mantle upwelling (Lipman and others, 1971; Kay and Kay, 1993; Pe-Piper and others, 2009).

Re-transported tephras characteristic of the West Foreland Formation make up a fifth suite of

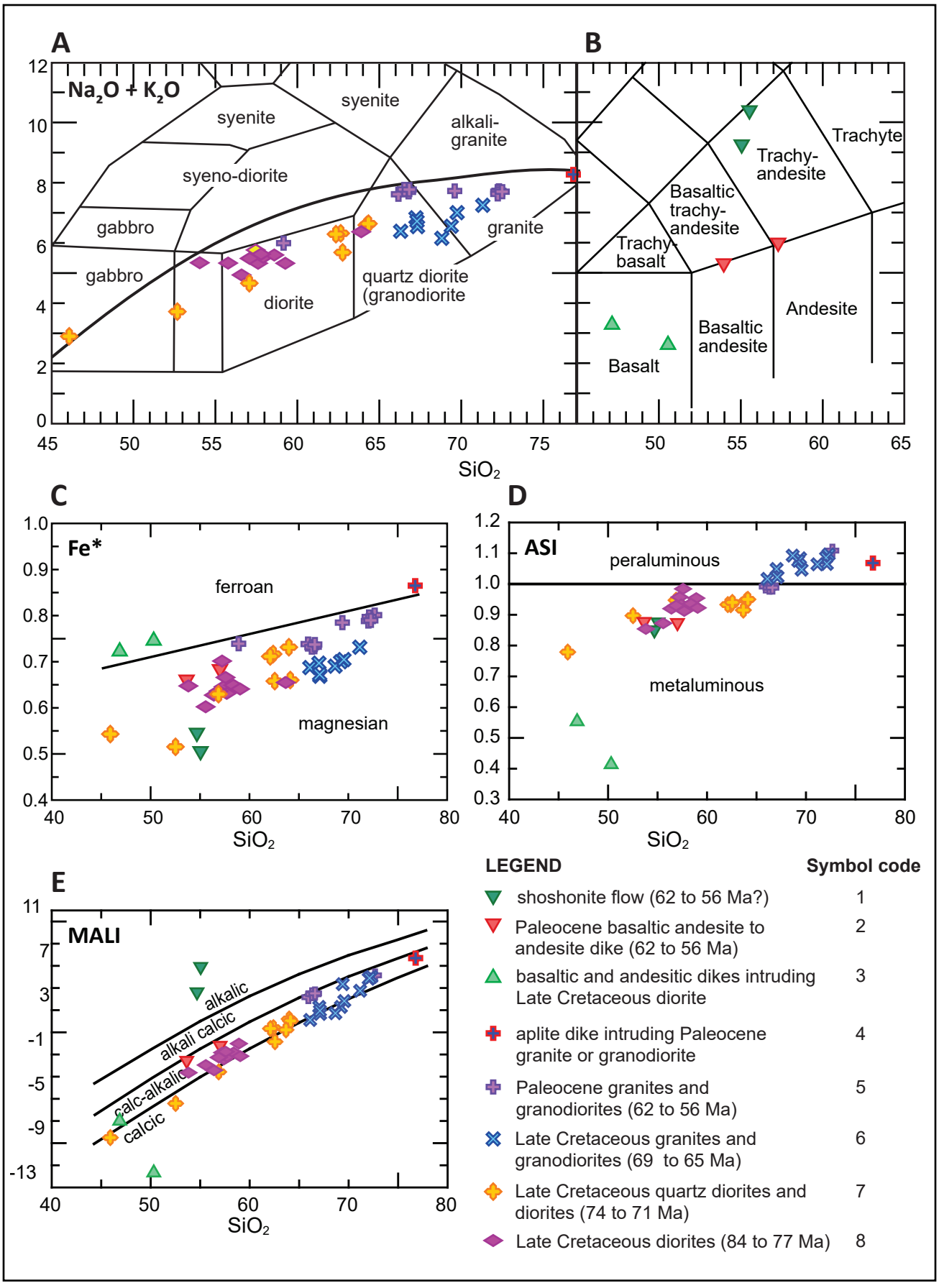
A
B
Na2O + K2O
syenite
syenite
alkali-granite
syeno-diorite
gabbro
granite
gabbro
diorite
quartz diorite (granodiorite
Trachyte
Trachy-andesite
Basaltic trachy-andesite
Trachy-basalt
Andesite
Basaltic andesite
Basalt
SiO2
C
Fe*
ferroan
magnesian
SiO2
D
ASI
peraluminous
metaluminous
SiO2
E
MALI
alkalic
alkali calcic
calc-alkalic
calcic
SiO2
LEGEND
Symbol code
shoshonite flow (62 to 56 Ma?) 1
Paleocene basaltic andesite to andesite dike (62 to 56 Ma) 2
basaltic and andesitic dikes intruding Late Cretaceous diorite 3
aplite dike intruding Paleocene granite or granodiorite 4
Paleocene granites and granodiorites (62 to 56 Ma) 5
Late Cretaceous granites and granodiorites (69 to 65 Ma) 6
Late Cretaceous quartz diorites and diorites (74 to 71 Ma) 7
Late Cretaceous diorites (84 to 77 Ma) 8

igneous rocks. No geochemical data exist for these rocks, but their MDAs range from ca. 42 to 38 Ma and most closely correlate to middle Eocene subalkaline intermediate to felsic plutons (Reed and Lanphere, 1973; Todd and others, 2014) exposed within 55 km to the west and north in the Neacola and Tordrillo mountains, respectively (Wilson and others, 2012; Wartes and others, 2015).

## Cooling of Intrusive Rocks

Zircon U–Pb and hornblende $^{40}Ar/^{39}Ar$ results from granitoids in the study area are consistent with conductive cooling of the intrusive bodies shortly after their emplacement in the middle to upper crust. Following Newton's law of cooling, plutonic thermal decay after melt emplacement into a colder medium progresses rapidly, but slows asymptotically as the intrusive body reaches equilibrium with the country rock. Mineral pair time-temperature cooling paths and MDD modeling suggests regional acceleration in cooling in the early Paleocene marked by increased rates below approximately 350˚C (figs. 7 and 8). The transition from slower to faster cooling implies that processes other than heat conduction into thermally stable bedrock were required for the rate increase. Candidate mechanisms include 1. thermal resetting of the potassium feldspar $^{40}Ar/^{39}Ar$ system at shallow crustal depths (and subsequent rapid cooling), or 2. denudation of the magmatic arc (advection of heat toward the surface due to erosional or structural unroofing of the uppermost crust). The timing of cooling broadly corresponds to an early Paleocene lull in plutonism (Helmold and others, 2018), but also to the development of a regional unconformity near the Cretaceous-Paleocene boundary that stripped much of the older forearc basin strata from its margins during an inferred episode of uplift and exhumation followed by re-initiation of the basin as a terrestrial depocenter (Boss and others, 1976). Therefore, determining the process(es) responsible for Late Cretaceous through Paleocene cooling is an important component to understanding contemporaneous Cook Inlet forearc basin dynamics.

A potential analog for two-phase cooling of Cretaceous-Paleocene Alaska-Aleutian Range plutons is the Sierra Nevada batholith. The Sierra Nevada batholith is arguably the most well-studied intrusive complex in the world (e.g., Piwinskii, 1968; Bateman and Dodge, 1970; Chen and Moore, 1982; Coleman and others, 2004), and the type example of an incrementally-assembled sheet pluton (e.g., Glazner and others, 2004; Coleman and others, 2004). $^{40}Ar/^{39}Ar$ thermochronology of the central Sierra Nevada batholith intrusive suite illustrates that plutons emplaced at 8–12 km depth (Ague and Brimhall, 1988; Davis and others, 2012) underwent a similar cooling history to Late Cretaceous intrusive rocks of this study. Zircon crystallization ages of the John Muir and Mount Whitney suites define growth of the plutonic complex over an approximately 12 m.y. period, comparable to the approximately 7 m.y. duration of late Cretaceous pluton assembly in the Neacola Mountains. $^{40}Ar/^{39}Ar$ results from co-existing hornblende, biotite, and potassium feldspar extracted from the Sierra Nevada rocks indicate two episodes of rapid cooling from approximately 800 to 150˚C—one that records cooling after pluton emplacement, and one interpreted as post-emplacement exhumation of the arc complex (Davis, 2010). As with many upper Cook Inlet Late Cretaceous plutons, zircon and hornblende dates from the Sierra Nevada granitoids overlap within analytical uncertainty, indicating immediate cooling at geologic timescales

**Figure 11, page 32 (previous).** Geochemical classification of Late Cretaceous and Paleocene igneous rocks from the Neacola and Tordrillo mountains. **A.** Total alkali versus silica diagram (Wilson, 1989) showing the compositional range of the plutonic rocks. **B.** Total alkali versus silica diagram of LeBas and others (1986) showing the compositional range of volcanic rocks. **C.** Fe-number (Fe*; Frost and others, 2001). **D.** Aluminum saturation index (ASI; Frost and others, 2001). **E.** Modified alkali-lime index (MALI; Frost and others, 2001). The data have been normalized to 100 percent anhydrous, with total $Fe_2O_3$ recalculated into FeO and $Fe_2O_3$ following the LeMaitre (1976) method. See appendix J for sample numbers, locations, and descriptions keyed to symbol codes.

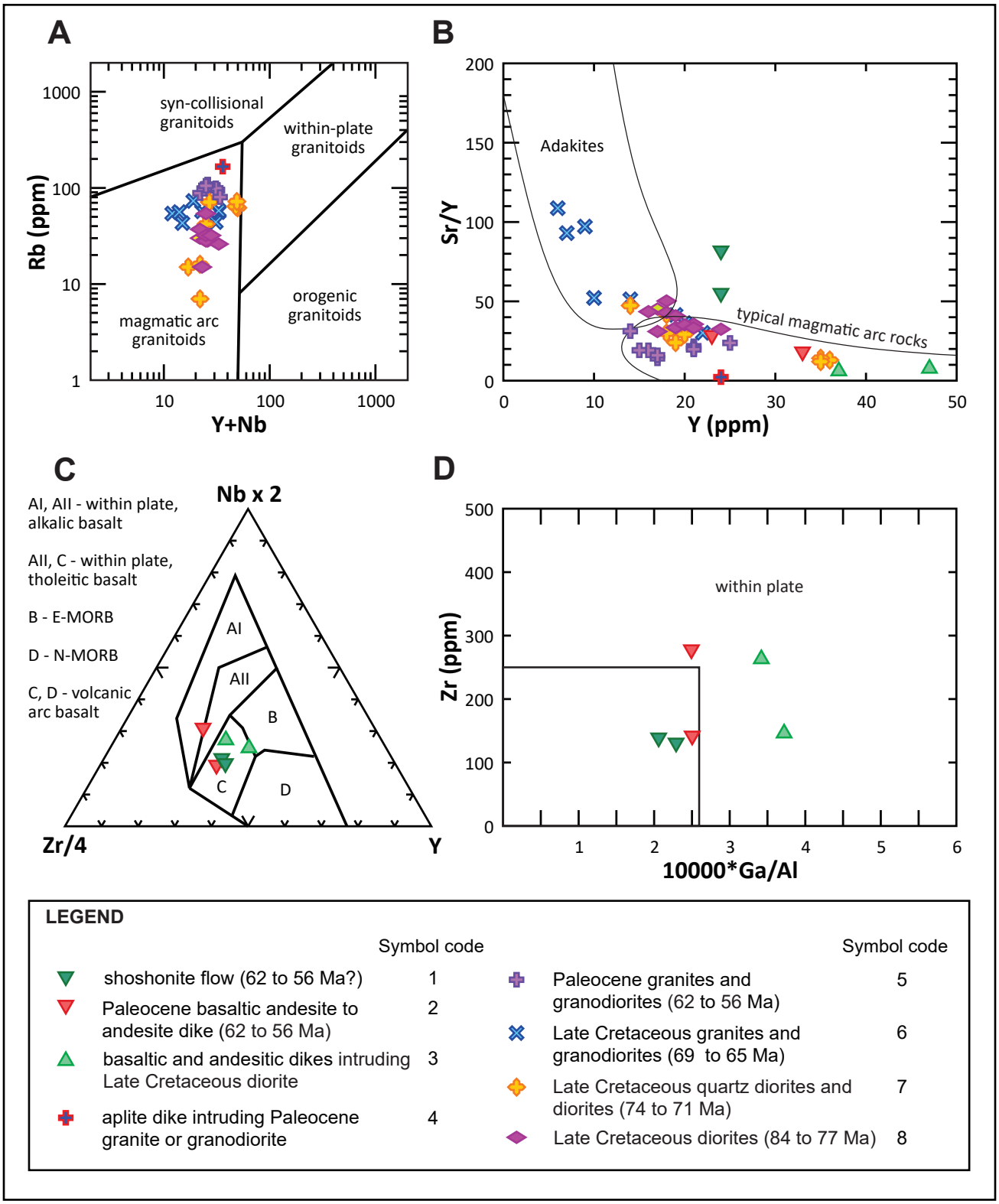


**Figure 12.** Tectonic classification of the igneous rocks from the Neacola and Tordrillo mountains: (**A**) Pearce and others (1984) classification for granitic rocks; (**B**) Y versus Sr/Y bivariate diagram; (**C**) Meschede (1986) discrimination diagram for basalts; and (**D**) Whalen and others (1987) discrimination diagram for within-plate granitoids. See appendix J for sample numbers, locations, and descriptions keyed to symbol codes.

to 500˚C in the middle to upper crust. Following a 7-19 m.y. period of relatively slow cooling after hornblende closure, potassium feldspar from these rocks record accelerated cooling to 150˚C at about 40–50˚C/m.y. Cooling recorded by feldspar from the Neacola Mountains in the upper Cook Inlet region similarly accelerates after a period of thermal decay following pluton emplacement (figs. 7 and 8). However, unlike the upper Cook Inlet granitoids, cooling below 350˚C in the central Sierra Nevada commenced over a narrow 1-2 m.y. time interval, which Davis (2010) interpreted as wholesale rapid exhumation of the undeformed arc complex. Potassium feldspar results reported here indicate that cooling below 350˚C was temporally and spatially more variable, occurring over a broader, 6 m.y. period at relatively short (kilometer-scale) wavelengths.

Such heterogeneous cooling recorded for nearly 100 km at the arc-forearc basin transition from the Neacola Mountains to Mount Susitna points to local expressions of regional processes in the early Paleocene. Possible mechanisms include thermal resetting of plutons by younger adjacent intrusions during ongoing arc construction, or structurally controlled exhumation cooling during a period of arc-forearc deformation. Feldspar in the study area exhibit no significant loss of argon in their lower temperature steps indicative of partial thermal resetting (e.g. apps D7H, D8H, D12G, D13D, E1G, E3H, E4E, and E6D), and unrestricted MDD model runs that were free to interrogate reheating favored monotonic cooling. Regionally, 40Ar/39Ar results suggest only conductive, post-emplacement cooling of plutons or cooling enhanced by exhumation. Twenty to 35 km due north of the study area in the Tordrillo Mountains (fig. 1), late Paleocene granitic rocks are interpreted to have cooled rapidly below approximately 150˚C during an episode of early to middle Eocene exhumation (Benowitz and others, 2012). In the Talkeetna Mountains 50 to 145 km along strike to the northeast (fig. 1), results from Late Cretaceous granitoids indicate that cooling followed a simple asymptotic path from emplacement to complete potassium feldspar closure (Harlan and others, 2017). Rejuvenated Paleogene cooling in the Talkeetna Mountains is instead recorded by lower temperature apatite fission-track thermochronometers (Bleick and others, 2012; Terhune and others, 2019). Save for one sample analyzed from the central Talkeetna Mountains (Terhune and others, 2019), available $^{40}Ar/^{39}Ar$ data collected over a broad area lack evidence of reheating between 150˚C and 350˚C. Notably, proposed regional resetting of forearc thermochronometers in south-central Alaska at temperatures up to approximately 250˚C by widespread arc magmatism or subduction of a spreading ridge inferred from detrital thermochronology (Finzel and others, 2016; Enkelmann and others, 2019) is not expressed in bedrock samples along the basin margin. Rather, heterogeneous cooling recorded by medium- to low-temperature thermochronometers that lack evidence for thermal resetting is most consistent with temporally- and spatially-variable exhumation across tectonic structures (Ehlers, 2005). Thus, the regional feldspar results support the contention that Paleogene cooling of the forearc was principally driven by deformation rather than transient heat sourced from the mantle (Lease and others, 2016).

## Evidence for Structurally Controlled Denudation and Cooling

Thermochronology paired with structural studies is particularly well suited for assessing the role faults play in the exhumation and cooling of structural domains (e.g. O'Sullivan and Wallace, 2002; Stockli and others, 2003). The Late Cretaceous intrusive rocks of the Neacola Mountains and the Paleocene Capps granite at the southern edge of the Tordrillo Mountains are cut by the Lake Clark and Capps Glacier dextral transtensional faults, respectively (see Gillis and others, 2017). $^{40}Ar/^{39}Ar$ results from samples collected across the structures separating exhumed granitoids from the forearc basin indicate that Late Cretaceous hornblende cooling predated faulting, yet Paleocene medium- to low-temperature (potassium feldspar) cooling closely predated or was synchronous with

transtension at the boundary. Thermochronometers analyzed from plutons of different age and geochemical compositions cut by the steeply southeast-dipping Lake Clark fault (LCF) constrain emplacement at different times and depths across the structure and subsequent diachronous cooling. Zircon crystallization ages of the up-thrown footwall intrusive rocks in the study area near Blockade Glacier (ca. 68.5–65.8 Ma) postdate downthrown hanging-wall block plutons analyzed from samples collected along its strike for approximately 60 km by 7 to 19 m.y. (Cain and others, 2019; zircon U–Pb=ca 85–76 Ma). However, hornblende cooling in the downthrown block lags pluton crystallization by 5 to 11 m.y. compared to upthrown block zircon and hornblende dates that overlap within analytical uncertainty and define geologically instantaneous cooling (fig. 13). The contrasting crystallization ages and high-temperature cooling between structural blocks implies that the LCF separates plutons emplaced at different times and depths. In short, the more rapid cooling from crystallization to below 500°C of the younger

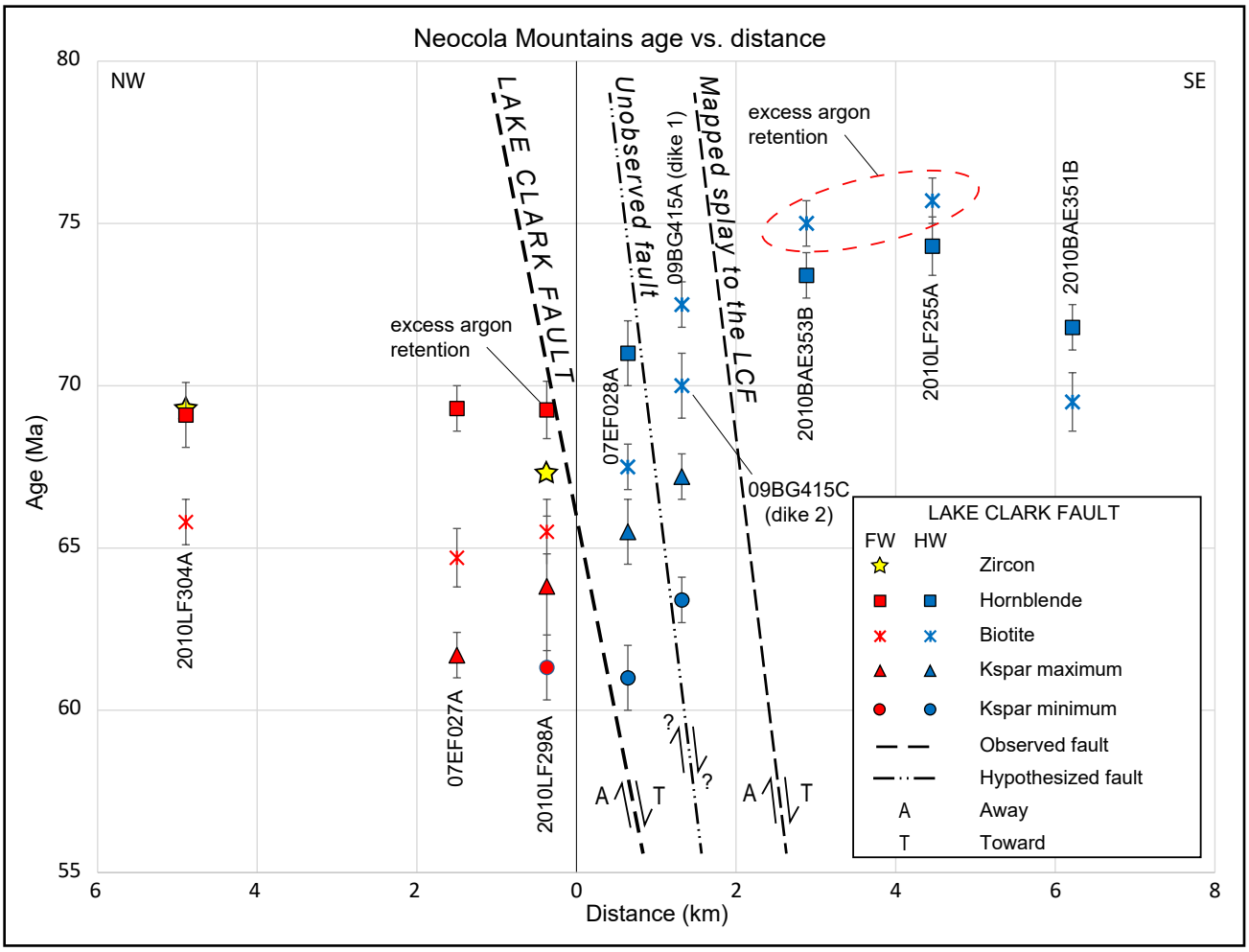


**Figure 13.** Age-distance plot across the Lake Clark fault, Neacola Mountains. Red symbols represent cooling ages from the up-thrown (footwall) block of the fault, blue symbols represent analyses from the down-thrown (hanging-wall) block. Black inclined dashed and dash-dotted lines represent faults separating thermochronometers. Note that specific mineral ages between footwall samples do not vary within analytical uncertainty, suggesting the samples cooled synchronously from approximately 500–150°C. Conversely, the cooling age distribution is older and more complex in the hanging-wall of the Lake Clark fault, and ages of specific minerals become younger broadly toward the fault across known and suspected structures. The pattern of cooling is consistent with down-to-the-southeast throw on the Lake Clark fault and structural dissection of its hanging-wall, consistent with subsidiary structures mapped in the area.

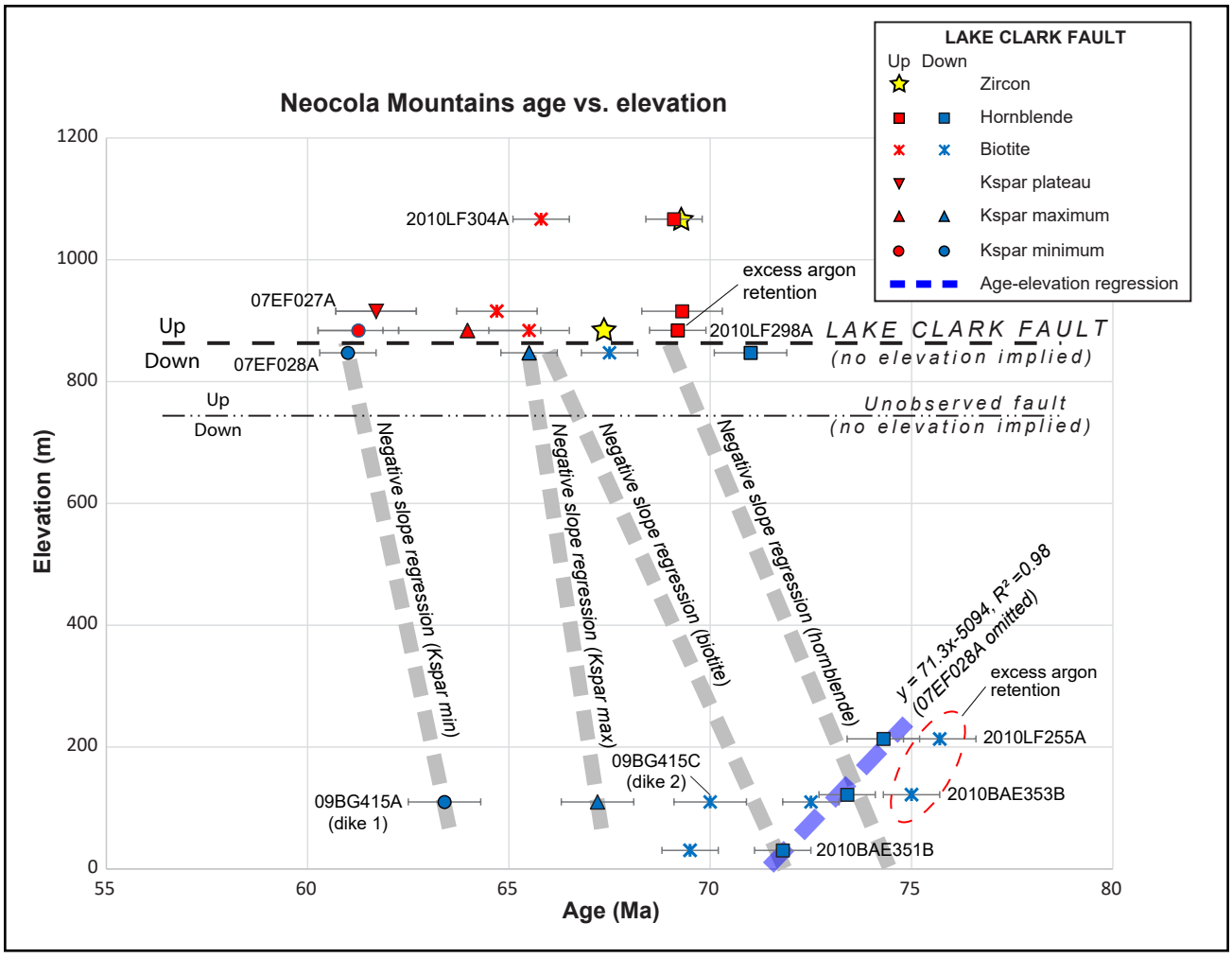


**Figure 14.** Age-elevation plot across the Lake Clark fault, Neacola Mountains. Red symbols represent cooling ages from the up-thrown (footwall) of the fault, blue symbols represent analyses from down-thrown (hanging-wall) block. Black horizontal dashed and dash-dotted lines represent faults separating thermochronometers, but otherwise have no associated elevation. Broad dashed lines are linear regressions of footwall and hanging-wall thermochronometers. Note that the negative slope regressions in the down-thrown block of the Lake Clark fault are constrained principally by a single high-elevation sample (07EF028a). When the hornblende age of this sample is restored vertically to align with the well-defined hornblende regression of the lower footwall samples, it produces similar slopes for the other mineral pairs, suggesting that sample 07EF028a is structurally separated from the other footwall samples.

upthrown block suggests it was emplaced more shallowly than the older, more slowly cooled rocks of the downthrown block. Faulting commenced after the hornblende system closed in both blocks.

A positive correlation between the three oldest downthrown hanging-wall hornblende dates and elevation (fig. 14) may also support slower initial cooling of the downthrown block. A linear regression of their relation (R-squared = 0.98) yields a slow apparent cooling rate of 3 to 4°C/m.y. assuming an elevated arc geothermal gradient of 35 to 55°C/km (Benowitz and others, 2012; Finzel and others, 2016; Terhune and others, 2019). Although tenuous, this slow rate may suggest that the samples cooled near the top of the hornblende $^{40}Ar/^{39}Ar$ partial retention zone (PRZ; see Baldwin and Lister, 1998; Reiners and Brandon, 2006), or were slowly exhumed through it. These relations are consistent with increasingly incomplete retention of argon with increasing depth (temperature) within the PRZ or slow exhumation through the PRZ at

a rate of 0.07 mm/yr. However, fitting regression lines through dates that include the highest elevation, youngest sample in the block (07EF028a) produces negative slopes for all thermochronometers (fig. 14), implying that the youngest sample was structurally elevated with respect to the older samples after hornblende cooling was completed by ca. 71 Ma. Restoring the youngest hornblende date to where it intersects the regression line requires approximately 880 m of down-to-the-southeast normal throw along an inferred splay to the LCF (fig. 14). Faster exhumation rates would require even greater throw. Although the fault splay was not observed in the field, a potential analog fault is well exposed less than 5 km to the northeast, where a transtensional subsidiary fault to the LCF is of sufficient magnitude to juxtapose Late Cretaceous intrusive rocks against Miocene forearc basin strata (Gillis and others, 2017). A source of error when interpreting these cooling ages in time-elevation space is the small (approximately 200 m) elevation range with respect to the several-kilometer horizontal distance between them over which most of the hangingwall samples were collected. The low relief increases the likelihood of unrecognized structural complexity and introduces potentially large uncertainties in the calculated exhumation rate (and thus the cooling rate) (Huntington and others, 2007). Therefore, more thorough systematic sampling across the LCF over a greater elevation range is warranted to better estimate exhumation and cooling rates from age-elevation profiles.

Nevertheless, in contrast to hornblende results from the downthrown block that appear to record protracted depth-dependent cooling, the synchronous zircon and hornblende dates in the upthrown block of the LCF (apps. D8 and D9) indicate instantaneous cooling of the sample within the resolution of the geochronometers at a position above the hornblende PRZ at ca. 69 Ma. We infer that the granodiorite that composes the entire up-thrown block was emplaced at a similarly shallow depth. Collectively, hornblende $^{40}Ar/^{39}Ar$ results suggest that downthrown and upthrown granitoids crystallized at different times and depths. The current partial juxtaposition of older, deeper downthrown rocks against younger, more shallowly-emplaced upthrown rocks favors a component of southeast-side-up reverse displacement on the LCF after the youngest hornblende sample began retaining argon at ca. 69 Ma, followed by extensional reactivation by the Paleocene (see below).

Cooling rates derived from hornblende-feldspar mineral pair ages and potassium feldspar maximum—minimum dates provide constraints on latest Cretaceous/Paleocene inception of the LCF and highlight disparate cooling histories of its downthrown hanging-wall and upthrown footwall blocks (fig. 15). Cooling of both blocks from approximately 500 to 350°C (hornblende-feldspar) occurred at the same average rate of 23°C/m.y. At about 67–66 Ma, their cooling histories diverge (fig. 15, app. I). From approximately 67 to 61 Ma the downthrown hanging-wall cooled from 350 to 150°C at the rate of 49°C/m.y.; double that of the upthrown footwall based on feldspar maximum and minimum dates (fig. 15, app. I). This acceleration of hanging-wall cooling is consistent with focused denudation of the block when it was topographically higher than the footwall and initiation of the LCF as a transpressional structure. Cooling of the footwall block below 150°C followed cooling of the hanging-wall by approximately 3 m.y. at a mean rate of about >80°C/m.y. from ca. 64 Ma to 61 Ma (fig. 15, app. I), likely due to reactivation of the LCF as a transtensional structure and inversion of the fault blocks during the Paleocene.

Although additional analyses are required to more accurately quantify depth of emplacement and rates of cooling for each structural domain, the polyphase slip history suggested by the downthrown and upthrown block cooling ages is supported by recent field studies. Kinematic indicators measured at numerous locations along the LCF zone and map-scale geologic relationships record spatially and temporally variable motion along the fault system (Caine and others, 2017; Gillis and others,

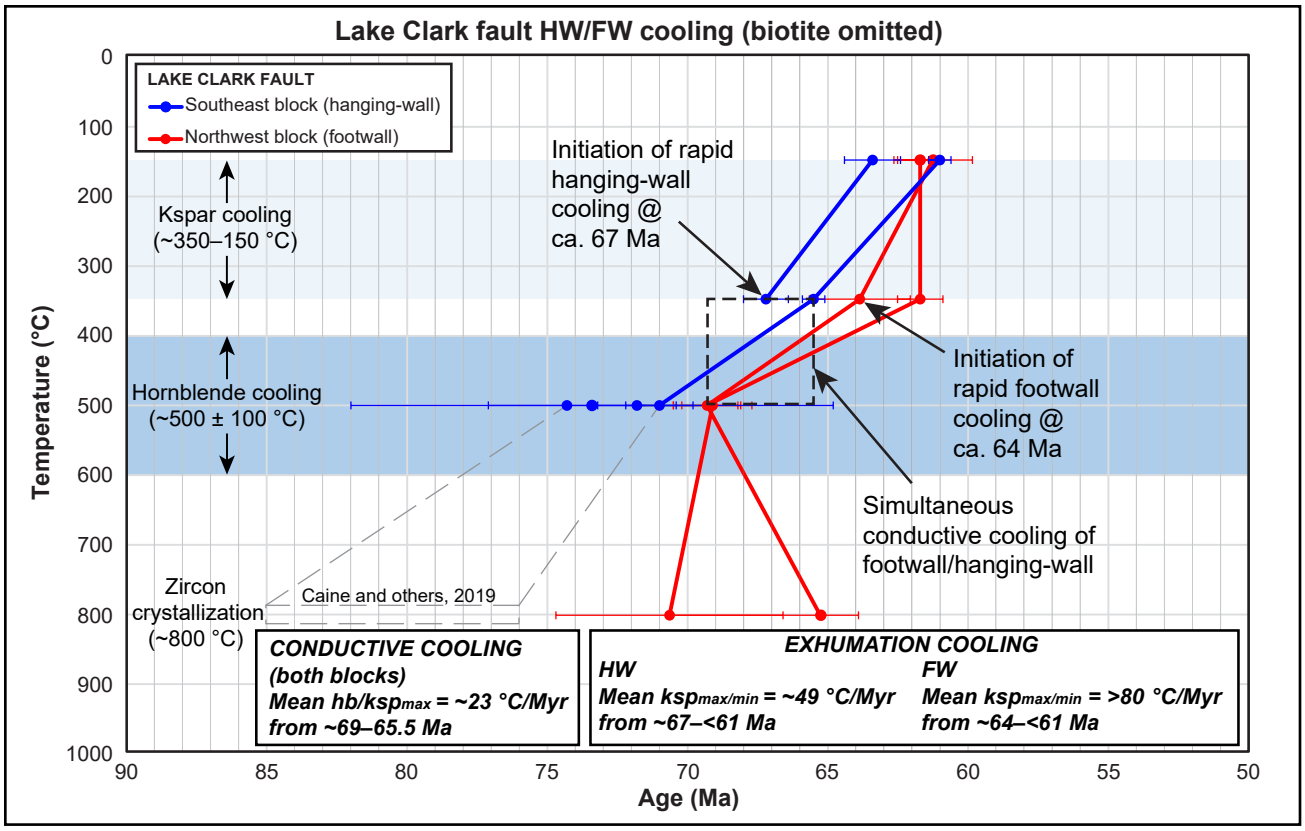


**Figure 15.** Cooling paths from approximately 800 to 150°C for granitoids sampled across the Lake Clark fault color coded by their hanging-wall and footwall positions (biotite results omitted). Dashed gray rectangle represents the zircon U-Pb age range of plutons located southeast (hanging-wall) of the Lake Clark fault in the Neacola-Chigmit Mountains (Caine and others, 2019). Gray dashed lines connect hanging-wall zircon U-Pb dates by others to $^{40}Ar/^{39}Ar$ results from the same domain (this study). Pale blue horizontal temperature fields represent closure temperature ranges for hornblende and potassium feldspar. Note that emplacement of hanging-wall granitoids predates footwall intrusion, but both blocks cool simultaneously at the same reduced rate from about 69–67 Ma. At ca. 67 Ma, hanging-wall cooling accelerates with respect to adjacent footwall rocks, perhaps marking the inception of the Lake Clark fault as a transpressional structure. Footwall cooling commences at a rapid rate at about 64 Ma as hanging-wall cooling ceases; interpreted as inversion of the Lake Clark fault under transtension (see fig. 16).

2017). Penetratively foliated diorite to granodiorite with fault-parallel fabrics that compose the southeast (downthrown) block of the LCF are placed against weakly foliated granodiorite to granite in the northwest (upthrown) block along a steeply southeast-dipping plane, suggesting that more deeply seated downthrown plutons are in reverse fault contact with more shallowly emplaced and compositionally distinct upthrown rocks (Caine and others, 2017, this study). This observation is consistent with hornblende $^{40}Ar/^{39}Ar$ results that indicate that rocks to the southeast were exhumed from a greater crustal depth. However, approximately 2 km to the northeast near the terminus of the LCF, downthrown Tyonek Formation strata exhibit the opposite relationship to the upthrown granodiorite (figs. 3 and 4). At that location, numerous slip lineations measured on a large splay to the fault clearly define down-to-the-south, dextral normal slip (Gillis and others, 2017). Thus, geologic and thermochronologic evidence indicates that the LCF initiated as a reverse or transpressional fault that was subsequently reactivated transtensionally (fig. 16), and that the magnitude of reverse slip exceeded the normal-slip component.

Accelerated deformation and cooling in the Paleocene is not restricted to rocks cut by the LCF.

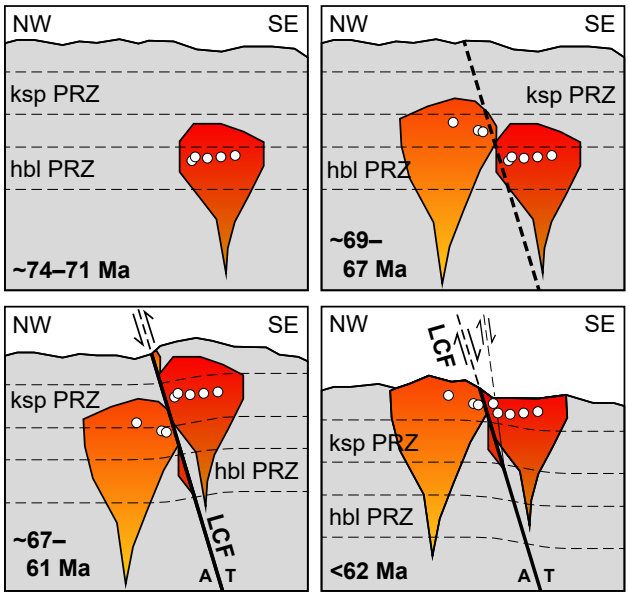


**Figure 16.** Interpretive block diagram of fault slip vs. cooling history across the Lake Clark fault as constrained by zircon U-Pb crystallization, $^{40}Ar/^{39}Ar$ cooling, and geologic relationships showing different emplacement times and depths of the hanging-wall and footwall plutons. White dots represent relative sample locations with time as constrained by the cooling data and positions at which they were collected. Thermochronometer dates suggest that the LCF initially slipped in a reverse sense beginning at about 67 Ma before reactivating in a normal sense after about 62 Ma.

Mineral pairs from the Mount Susitna granodiorite located at the intersection of the CMF and faulted western limit of the Susitna basin (figs. 3 and 4) also record increased cooling from 53°C/m.y. after 66 Ma to over 80°C/m.y. after 64 Ma (fig. 7, app. I). MDD modeling details an acceleration in cooling from approximately 9°C/m.y. to 97°C/m.y. at roughly 63 Ma. Comparable cooling trends for approximately 100 km along the structural boundary of the forearc basin implies that its thermal state was controlled in part by regional deformation at that time. Moreover, $^{40}Ar/^{39}Ar$ results and cross-cutting relations associated with the dextral normal Capps Glacier fault (CGF) in the southern Tordrillo Mountains—approximately 20 km to the northeast of the LCF and 75 km due west of Mount Susitna (figs. 3 and 4)—suggest that transtension may have initiated there as early as ca. 56 Ma. This broadly coincides with, and immediately postdates, rapid middle Paleocene cooling of the LCF upthrown block and Susitna basin margin, respectively. The ca. 56–55 Ma Capps granite that forms the upthrown footwall of the CGF at the southern flank of the Tordrillo Mountains was emplaced too shallowly for hornblende, biotite, or potassium feldspar systems to record structural exhumation. However, andesite and basalt dikes with arc to within-plate chemical signatures systematically intrude the granite along inferred synthetic Riedel shears that emanate from the CGF. Within analytical uncertainty, emplacement dates of the dikes overlap the crystallization ages of the Capps granite, indicating that intrusion of dikes must have closely post-dated emplacement of the granite. The dikes are therefore interpreted to date the onset of transtension and pull-apart basin formation immediately following late Paleocene pluton emplacement.

The rates at which Paleocene cooling occurred (±100°C/m.y.) are uncommonly rapid for exhuming orogens. Such rates are generally restricted to tectonically active areas with unusually high erosional efficiency such as the windward sides of mountains in Taiwan (75–150°C/m.y.; Dadson and others, 2003) and the glacially carved St. Elias Range in Alaska (120°C/m.y.; Berger and others, 2008). Cooling rates for highly strained regions can be even greater; for instance, Namche Barwa, Nepal and Nanga Parbat, Pakistan (100–200°C/m.y.; Whittington, 1996; Burg and others, 1997). Although the arc-forearc basin boundary was demonstrably tectonically active during the early Paleocene and into the Eocene, the region was neither highly denuded nor strained. The apparent incongruence between high cooling rate and relatively low magnitude of exhumation observed at the forearc margin may be reconciled if the recently intruded plutons had not yet equilibrated to the ambient crustal temperature before onset of denudation (e.g., Finzel and others, 2016). Hornblende-feldspar cooling at approximately 23°C/m.y. (app. I) implies that the plutons were still in a state of post-emplacement thermal decay during their exhumation. If so, then structurally driven exhumation would serve to increase an already

elevated geothermal gradient (and thus the cooling rate) as heat is advected toward the surface (Moore and England, 2001). Thus, such uncommonly high cooling rates may also characterize unroofing of active, or recently active, magmatic arcs.

In summary, the $^{40}Ar/^{39}Ar$ hornblende dates record rapid conductive cooling of plutonic bodies shortly after their emplacement in the middle to upper crust. Late Cretaceous granitoids of the Neacola Mountains separated by the LCF have different chemistries and were intruded at different depths. The older, more deeply emplaced ca. 74–71 Ma body is presumed to have been juxtaposed transpressionally against the younger ca. 69–67 Ma granitoid after ca. 67 Ma based on cooling ages and field relations. Diachronous closure of potassium feldspar appears to be largely structurally controlled. Synchronous cooling of both blocks from 500 to 350˚C occurred at a reduced rate of 23˚C/m.y. until about 66–64 Ma, when the fault blocks begin to follow different, more rapid cooling paths (fig. 15). Despite some temporal overlap in cooling domains, cooling of the southeast block (downthrown) at ca. 66–61 Ma predates northwest block (upthrown) cooling at ca. 62–<60 Ma by up to 5 m.y. (fig. 15) as the LCF initiated as a transpressional fault before its transtensional reactivation (fig. 16). The cooling ages along with whole rock $^{40}Ar/^{39}Ar$ dates of ordered dikes that intrude inferred transtensional structures of the CGF suggest initiation of regional transtension in the middle to late Paleocene. Similar thermochronologic results between the Neacola Mountains and Mount Susitna located approximately 100 km to the northeast at the arc-forearc basin margin (fig. 3) implies that accelerated Paleogene cooling was regional. As such, the faults that cut the Mount Susitna granodiorite (e.g., the CMF and structures along the southwest boundary of the Susitna basin) likely played a key role in the timing and rate of its cooling as well.

## Paleogene Sediment Provenance

Identifying source terranes and lithologies to a sedimentary basin is chiefly accomplished through analysis of its detrital constituents (e.g., Dickinson, 1985). Insights from spatial and temporal patterns of sediment provenance inform basin depositional models, particularly how sediment routing systems vary during basin development (e.g., DeGraaff-Surpless and others, 2002). Here we synthesize detrital zircon date distributions, zircon epsilon hafnium values (εHf), modal sandstone mineralogy, and conglomerate clast compositions to distinguish between West Foreland Formation and Hemlock Conglomerate and present a revised depositional model for the middle to late Eocene Cook Inlet forearc basin.

The large fraction of detrital zircons extracted from numerous reworked West Foreland Formation (Twf) tephras supplement sandstone and conglomerate clast compositional data, clast dates, sedimentary facies interpretations, and geologic mapping to define a model in which detritus sourced from the structurally elevated magmatic arc was syntectonically deposited into proximal transtensional sub-basins controlled by the structures discussed in the previous section. Samples collected from Twf in the downthrown block of the Capps Glacier fault (CGF) yielded chiefly middle Cretaceous and Paleocene detrital zircons (fig. 10B) with ages that are comparable to igneous bedrock ages in the adjacent upthrown block (e.g., Reed and Lanphere, 1972; Moll-Stalcup, 1994; Wilson and others, 2012; this study). Twf conglomerate compositions are dominated by intermediate to mafic volcanic rocks and lesser plutonic clasts (fig. 17A; Finzel and others, 2015; Helmold and others, 2018). Clasts analyzed from the lower and middle intervals of the succession yielded ca. 103–98 and ca. 60–56 Ma dates that complement major detrital zircon peaks at ca. 100 and 61 Ma (fig. 18). Basal Twf conglomerate is composed entirely of large clasts derived from the unit onto which it was deposited (Kv in fig. 5; LePain and others, 2013), and plutonic lithologies constitute nearly 25 percent of West Foreland clasts. The youngest dates require up to several kilometers of late Paleocene to early Eocene exhumation prior to clast deposition in the

forearc basin. Within 0.5 km of the CGF, the Twf is locally composed entirely of angular lithic fragments eroded from the proximal footwall granite and metavolcanics. Modal sandstone compositions characterized by volcanic-lithic framework grains (fig. 17B) plot firmly within the magmatic arc provenance field of Dickinson (1985) and indicate derivation from undissected and dissected arc sources of the Aleutian-Alaska Range (Helmold and others, 2018). LePain and others (2013) interpreted the margin-proximal succession as an upward fining fan-head trench to distal fan assemblage emanating from an active volcanic arc and from older arc lithologies in the up-thrown basin

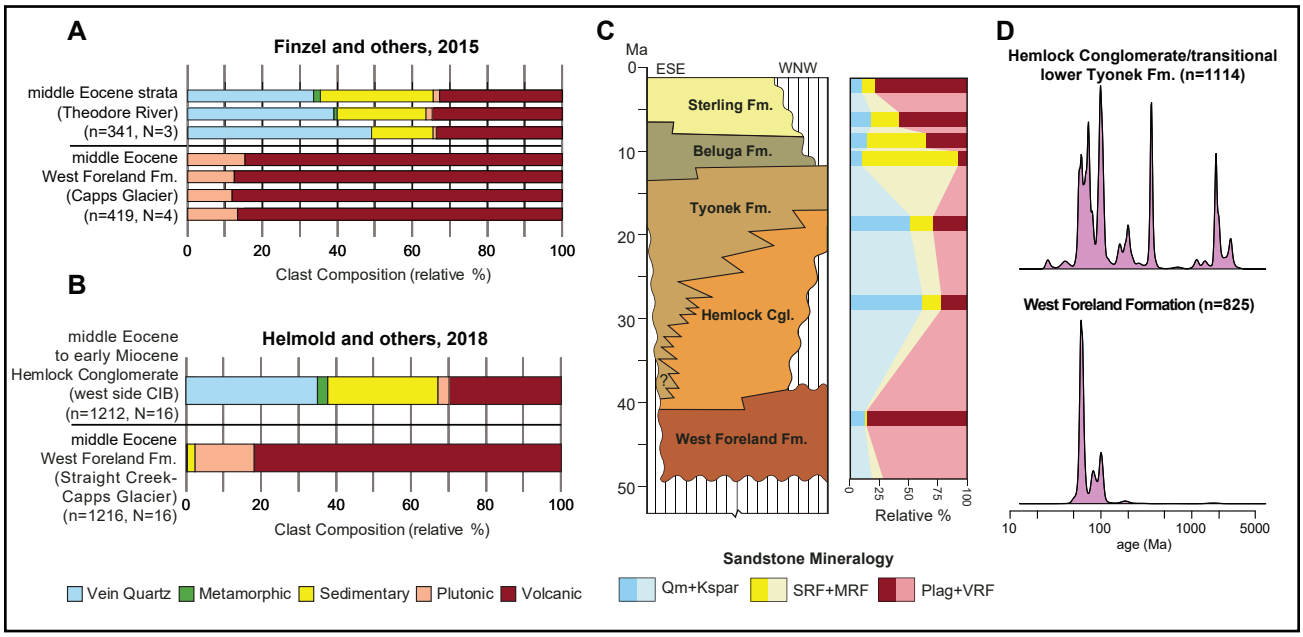


**Figure 17.** Detrital characteristics distinguishing the basin margin fan deposits of the West Foreland Formation from axial-fluvial Hemlock Conglomerate. **A.** Clast composition of middle Eocene conglomerates in the Theodore River drainage (top) and West Foreland Formation (Twf) from a single location near Capps Glacier (bottom). The bimodal composition of volcanic and plutonic lithologies from the Twf differ markedly from the abundant vein quartz, sedimentary, and fewer metamorphic rock clasts in the Theodore River strata, contrasting the strictly arc provenance of Twf with more diverse clast lithologies composing strata distal to the basin edge. The contemporaneous, yet compositionally distinct strata indicate competing sediment sources between the basin margin and axis at that time. (adapted from Finzel and others, 2015). **B.** Clast composition of conglomerates in the Hemlock Conglomerate (Th) aggregated from several northwestern middle Eocene to early Miocene Cook Inlet basin (CIB) outcrops and offshore well core (top), and from throughout the middle Eocene West Foreland succession between Straight Creek and Capps Glacier (bottom; adapted from Helmold and others, 2018). The Theodore River conglomerates bear a remarkable resemblance to Th clast lithologies from a variety of outcrops and well core along the northwest margin of the CIB that most commonly range in age from late Oligocene to early Miocene, with only a minor similarity to middle Eocene age West Foreland strata. The nearly identical minerology of the Eocene Theodore River strata to Th suggests that The Theodore River outcrops represent some of the oldest examples of Th known in the basin. Whereas middle Eocene Twf and Th conglomerates apparently interfinger distal to the northwestern basin margin, late Eocene to early Miocene Th overlies Twf near the basin edge, suggesting that a structurally elevated basin margin ceases to be an important sediment source after the middle Eocene. N= number of clast counting stations, n= total number of clasts counted. Volcanic clast category includes flow, volcaniclastic, and greenstone lithologies. Sedimentary clast category includes sandstone, siltstone, argillite, and chert, following Helmold and others (2018). **C.** CIB sandstone mineralogy tracks changes in clast composition between between Twf and Th on its northwestern side (adapted from Helmold and others, [2018]). The transition from feldpathic to quartzofeldspathic compositions in the upper Paleogene reflect a reduction in structural exhumation of the proximal margin and magmatic arc activity, resulting in a relative increase in distal metamorphic sediment sources (Finzel and others, 2015, 2016; Helmold and others, 2018). VRF=volcanic rock fragments, SRF=sedimentary rock fragments, MRF=metamorphic rock fragments, Qm=monocrystalline quartz. **D.** A comparison of detrital zircon dates between middle Eocene West Foreland Formation and middle Eocene to early Miocene Hemlock Conglomerate/transitional lower Tyonek Formation highlighting the proximal arc provenance of Twf vs. the diverse provenance of widely sourced Th.

margin. Cross-stratified Twf tephras and tuffaceous sandstones up to 12 m thick likely reflect hyperconcentrated flood flow during lahar events, indicating proximity to middle Eocene volcanic centers (LePain and others, 2013).

The distinguishing characteristics of Twf include a dearth of Mesozoic and older zircon grains, a uniformly feldspathic sandstone composition, textural immaturity, and common reworked tephras (LePain and others, 2013; Helmold and others, 2018). However, Twf deposited at the structural basin margin near Capps Glacier contrast sharply with middle–late Eocene clastic rocks exposed farther basinward in the Beluga, Theodore, and Lewis River drainages (fig. 3). Their markedly different lithofacies and provenance define two largely separate depositional systems operating simultaneously within the basin. Quartz-rich conglomerates (up to 50 percent clast composition) and sandstones that crop out adjacent to the Castle Mountain fault (CMF) in the drainages noted above contain abundant Precambrian and Mesozoic grains, are conspicuously quartzofeldspathic, texturally mature, and entirely lack bedded volcanogenic material (fig. 17; LePain and others, 2013; Finzel and others, 2015, 2016; Enkelmann and others, 2019; Helmold and others, 2018). These quartz-rich strata are further differentiated by evolved zircon εHf values that differ markedly from strongly juvenile West Foreland rocks of the Capps Glacier area while demonstrating a strong affinity to similarly evolved εHf values of late Oligocene Hemlock Conglomerate (Th) from well core and cuttings sampled closer to the basin axis (Finzel and others, 2016). Although distinctive, the strata are not well characterized, which has led to ongoing confusion about their formation assignment (e.g., Magoon and others, 1976; Zippi and Loveland, 2012; Wilson and others, 2012; Finzel and others, 2015, 2016). All available data along with recent stratigraphic investigations of these outcrops by

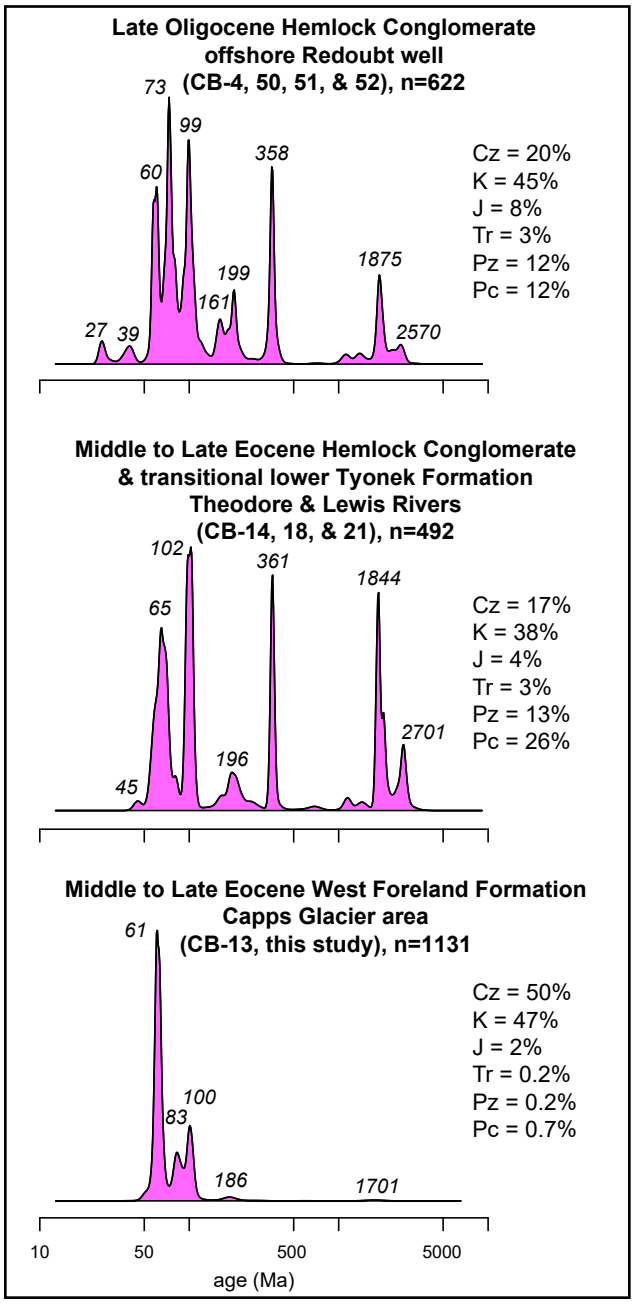


**Figure 18.** Kernel density estimates (KDE) of detrital zircons comparing middle Eocene quartz-bearing outcrops of the Theodore and Lewis rivers (middle) with late Oligocene Hemlock Conglomerate from the Redoubt well offshore of the West Foreland promontory, Cook Inlet (upper), and middle Eocene West Foreland Formation exposed in the Capps Glacier area (lower). Close similarities between the Theodore and Lewis river strata to Hemlock conglomerate, particularly their relatively high proportion of Paleozoic and older grains (24–39 percent), contrasts sharply with the West Foreland Formation date distribution, in which 97 percent of the grains are Cretaceous and younger. These results suggest the Theodore and Lewis river outcrops share greater affinity to the axial-fluvial component of the forearc basin depositional system during the Eocene, than to the alluvial system defined by fans emanating from the structurally-controlled basin margin.

DGGS (LePain and others, 2013; Helmold and others, 2018) indicate that they are time-transgressive Th and Tt as defined by Calderwood and Fackler (1972), rather than Twf as commonly viewed.

Lithofacies and provenance data also link the quart-rich middle–late Eocene strata exposed adjacent to the CMF (Zippi and Loveland, 2012; Finzel and others, 2016; Helmold and others, 2018; Zippi and others, 2021; this report) to a younger succession of early Oligocene–middle(?) Miocene Hemlock Conglomerate exposures south of Capps Glacier along the Beluga and Chuitna River drainages to the southwest (fig. 3) (LePain and others, 2013; Helmold and others, 2018), and to Hemlock Conglomerate recognized in wells offshore toward the basin axis (fig. 17; Finzel and others, 2016; Helmold and others, 2018; Enkelmann and others, 2019). Detrital zircon date distributions and zircon εHf values from middle–late Eocene Theodore and Lewis River outcrops (fig. 3) are nearly identical to those from late Oligocene Hemlock intervals from offshore wells (fig. 18). Strata sampled from both locations (sample CB-14 in Finzel and others, 2015, 2016; sample CB-21 in Enkelmann and others, 2019) produce detrital zircon distributions of which 24–39 percent of the grain ages are Paleozoic or older (fig. 18), yielding a grain-date distribution that is consistent, in part, with sediment sourced from metamorphic rocks of the Yukon–Tanana upland (Dusel-Bacon and others, 2015, 2017; Finzel and others, 2016).

Exposures on the Theodore River, north of the Castle Mountain fault (fig. 3), consist of massive to crudely bedded pebble-cobble conglomerate and minor quartzo-feldspathic sandstone as discontinuous lenses. Clasts consist of a variety of fine-grained volcanics, including the distinctive banded tuff noted in the Lewis River exposure, and a significant volume of white vein quartz. The Theodore River succession is the product of a gravelly braided fluvial system and is assigned to the Hemlock Conglomerate based on facies criteria. Following LePain and others (2013), we interpret similar facies cropping out on the Beluga River adjacent to the CMF as Hemlock. A single sample from quartz-rich late Eocene outcrops along the adjacent Lewis River produced a similarly high proportion of Paleozoic and older detrital grains (26 percent; sample CB-18 in Enkelmann and others, 2019). However, their facies differ from nearby Hemlock Conglomerate outcrops. The exposure on Lewis River, south of the Castle Mountain fault (fig. 3), consists dominantly of trough cross-bedded, quartzo-feldspathic sandstone and lesser amounts of interbedded pebble conglomerate and silty clayshale. Conglomerate clasts are dominantly white vein quartz, dark gray to black argillite and a minor, but distinctive, banded tuff. This succession is the product of a dominantly sandy braided fluvial system. Owing to its location in the far northwestern extent of the basin, the Lewis River succession may be correlative to the informal Bell Island sandstone known only in the uppermost Cook Inlet subsurface. The Bell Island sandstone is alternately considered a facies variation of the Hemlock Conglomerate (Hartman and others, 1972) or defined as lowermost Tyonek Formation (Boss and others, 1976). Following mapping by Magoon and others (1976), we assign the Lewis River succession to transitional lower Tyonek Formation based on facies criteria and similarities to lower Tyonek Formation in the Chuitna River and Capps Glacier areas. The lower middle Eocene–early Oligocene palynologic age calls for the Beluga, Theodore, and Lewis River outcrops (fig. 3) (Zippi and Loveland, 2012; Finzel and others, 2016; Zippi and others, 2021; this report) and ca. 45.2–42.7 Ma detrital zircon MDAs (Finzel and others, 2016; Enkelmann and others, 2019) make them the oldest known exposures of Hemlock Conglomerate and Tyonek Formation. These findings support interpretations based on proprietary industry data that indicates Cenozoic formations are time-transgressive and the West Foreland Formation, Hemlock Conglomerate, and transitional Tyonek Formation are locally contemporaneous (fig. 17C).

Although mineralogically mature composition is a distinguishing characteristic of Hemlock Conglomerate and lower Tyonek Formation, prox-

imal sediment sources also appear to be important in their Eocene successions. 55.7 ± 0.6 Ma intermediate to felsic volcanic clasts with distinctive flow-banded textures (table 3; apps. G43 and G44) are commonly observed only at Hemlock/transitional Tyonek outcrops on the Beluga, Theodore, and Lewis rivers (fig. 3) (LePain and others, 2013). The source of the distinctive volcanic clasts is uncertain, but a similar flow-banded andesite(?) horizon (54.3 ± 0.4 Ma, $^{40}Ar/^{39}Ar$) encountered in the Pure Kahiltna 1 well 80 km to the north in the Susitna basin (Stanley and others, 2013) may be correlative with 56.2 ± 1.7 to 45.5 ± 1.7 Ma bimodal volcanic rocks commonly associated with the middle–late Paleocene Arkose Ridge Formation in the adjacent Talkeetna Mountains (Silberman and Grantz, 1984). If the Hemlock clasts were sourced from the Talkeetna Mountains, it may suggest that middle Eocene exhumation cooling of the upthrown block of the CMF (Bleick and others, 2012; Terhune and others 2019) is tectonically linked to contemporaneous CGF slip and footwall exhumation. These new age and provenance data allow us to revise the CIB chronostratigraphic column to more accurately reflect deposition at the northwestern margin of the basin (figs. 17C and 19). The partially volcanilithic facies recognized along the Beluga, Theodore, and Lewis rivers (fig. 3) (e.g., the common ca. 56 Ma flow-banded volcanic clasts) might therefore mark the inter-fingering between transverse fan-dominated deposition at the tectonically active northwestern basin margin, and the trunk axial-fluvial drainage system occupying the basin axis.

The chronostratigraphic character of Cook Inlet Cenozoic strata is inferred in published stratigraphic columns influenced by proprietary industry data (e.g., Swenson, 2001); however, the contemporaneous deposition of West Foreland Formation, Hemlock Conglomerate, and Tyonek Formation outlined here is the first evidence of their potential lateral inter-fingering or transitional relationship in outcrop (fig. 19). Temporal and spatial associations suggest that the West Foreland Forma-

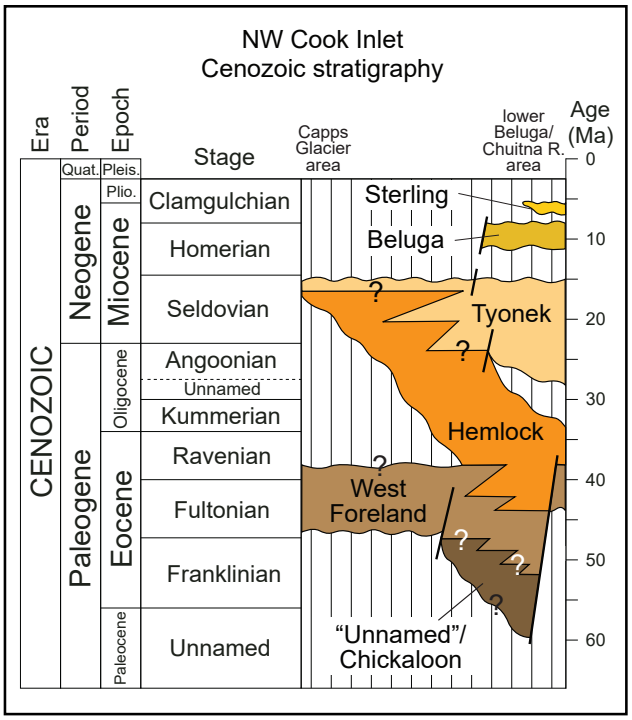


**Figure 19.** Revised chronostratigraphic column of Swenson (2001) for the west side of Cook Inlet based on new stratal age and geologic mapping constraints (Gillis and others, in preparation). Southeast of the Castle Mountain fault (CMF), West Foreland Formation (Twf) and inferred "un-named" Paleocene strata thicken across faults based on interpretation of subsurface data (Gillis and others, 2017). An apparently complete succession of uncommonly thick late Eocene–early Miocene Hemlock Conglomerate (Th) is upwardly gradational with Twf northwest of the CMF in the Capps transtensional basin (figs. 3, 4). The succession includes Eocene-age strata in the upper Chuitna River drainage and also middle Eocene to late Eocene–early Oligocene strata in the Theodore and Lewis drainages on the southeast of the CMF that may be laterally time transgressive. A middle Eocene–late Oligocene fault-bound sliver southeast of the CMF on the lower Beluga River is also considered part of the succession. Hemlock Conglomerate (Th) thins and becomes younger toward the northwest basin margin. At the Capps Glacier, very thin late Miocene Th, or perhaps conglomeratic lower Tyonek Formation (Tt) unconformable overlays Twf (fig. 4). The upper Th contact is gradational with Tt northwest of the CMF, but is in slight angular unconformity with Tt on the Beluga River southeast of the CMF (fig. 4). The Tt/Beluga Formation (Tb) contact is not exposed on the northwest side of Cook Inlet basin. However, Tb is unconformably overlain by Sterling Formation in outcrop on the lower Beluga River (fig. 4). Vertical ruled lines represent missing time. Dark inclined lines schematically represent faults.

tion and Hemlock Conglomerate/lower Tyonek Formation represent different, yet partly contemporaneous depositional systems within the forearc basin: one a fan-dominated system that is closely linked to active structures that delivered locally-sourced detritus from the basin margins (Twf), and the other an axial-fluvial system controlled by regional-scale subsidence and supplied with sediment from more diverse and distal source areas (Th/lower Tt) (LePain and others, 2013). Much of the coarse feldspathic West Foreland detritus was likely sequestered by transtensional sub-basins localized at the northwestern basin margin; where penetrated in wells nearer the basin axis—including its type section in the West Foreland #1 well—the unit is typified by a thinner succession of tuffaceous siltstone, claystone, and few tephras with only minor conglomeratic sandstone beds (Calderwood and Fackler, 1972). This depositional model (fig. 20) is an adaptation of those proposed by industry (e.g., McGowen and Doherty, 1994 [internal Atlantic-Richfield Company {ARCO} report] in Swenson, 2001) and Finzel and others (2015, 2016) but is notable for its emphasis on the role of transtensional tectonics in controlling sediment accommodation at the western CIB margin.

## Sediment Accumulation Rates

Where and how rapidly sediment accumulates in a basin provide insights into the mechanisms that

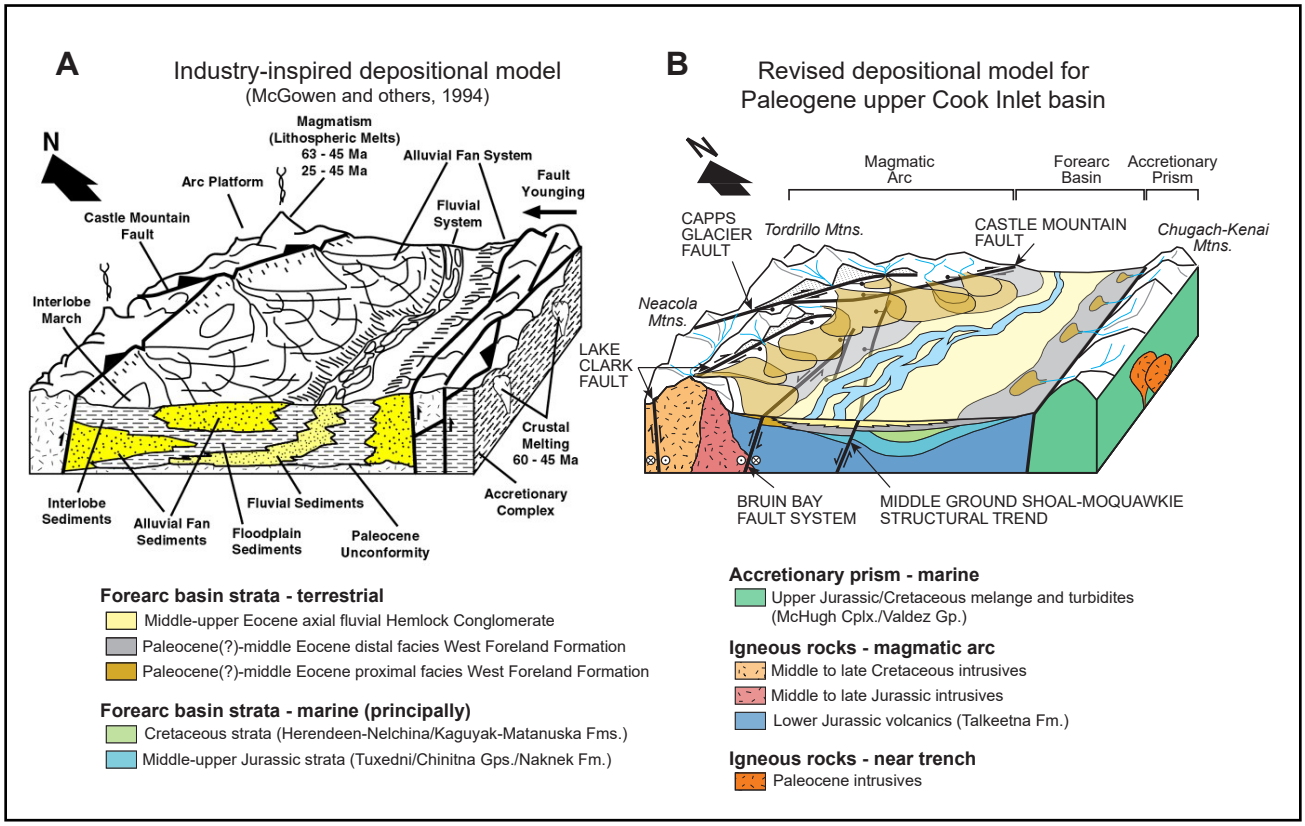


**Figure 20. A.** Block diagram of upper Cook Inlet during Eocene time comparing an industry-inspired model featuring an axial-fluvial depositional system in a contractional forearc basin setting (Swenson, 2001) with (**B**) a revised depositional model for the Paleogene basin depicting a similar depositional system in a transtensional setting. Middle Eocene West Foreland Formation was deposited as coarse alluvium emanating from the uplifted basin margins and finer grained sediments near the basin axis that bypassed transtensional sub-basins. Relatively thick middle–late Eocene Hemlock Conglomerate (Th) is only known to occur near the periphery of a transtensional basin where an axial fluvial system transporting sediment from metamorphic terranes distal to the CIB may have been drawn toward the locus of subsidence near the basin margin. By contrast, Oligocene and younger Th is widespread and uniformly thin, reflecting a very low sedimentation rate that may mark a period of tectonic quiescence in the basin.

drive subsidence and how they change over time. The relatively fine resolution of ages throughout the West Foreland Formation and refined understanding of the Cenozoic stratigraphy (LePain and others, 2013) allow for estimating sedimentation rates and trends at the arc-forearc basin margin. Twf exposed near the northwestern margin of upper Cook Inlet was deposited into a transtensional sub-basin bounded by the Capps Glacier and Castle Mountain faults (Gillis and others, 2017; figs. 3 and 4). Sediment accommodation in strike-slip basins is governed on a first order by the geometry and slip rate of the bounding faults (Xie and Heller, 2009); the latter of which commonly ranges between 0.01 and 10 mm/yr (Ziony and Yerkes, 1985). Consequently, subsidence of strike-slip basins is often rapid, brief, and localized by the structures that control it (Christie-Blick and Biddle, 1985). Published sediment accumulation rates for strike-slip basins range from 0.40 to 11 mm/yr (Johnson, 1985; Dorsey and others, 2011) for durations commonly less than 10 m.y. (Woodcock, 2004; Xie and Heller, 2009). In contrast, sedimentary basins from diverse tectonic settings worldwide typically record more modest long-term accumulation rates of about 0.03–1.5 mm/yr (Miall, 1978) over time scales of tens of millions of years or greater (Xie and Heller, 2009).

Provisional estimates of sediment accumulation rates for the West Foreland Formation presented here (fig. 5) are based on newly established MDAs and composite thicknesses from LePain and others (2013). These rates are low compared to rates documented in other transcurrent basins (e.g., Yeats, 1978; Link and Osborne, 1982; Johnson, 1985; Horowitz, 1989; Dorsey and others, 2011). The average rate of accumulation of the Twf is approximately 0.11 mm/yr based on a conservative maximum thickness of 960 m and an 8.9 m.y. duration of deposition. The rates vary with time and perhaps distance from the CGF toward the CMF from about 0.07 mm/yr for Twfl in the proximal hangingwall (350 m over 4.9 m.y. from ca. 47.0 to 42.1 Ma) to over 0.10 mm/yr for the upper subunit (Twfu) approximately 2 km basinward of the fault (>305 m in >3.0 m.y. from >41.1 to ca. 38.1 Ma). Most Twfm MDAs and the lowermost MDAs in Twfu are not stratigraphically concordant (i.e., do not follow a upward stratigraphic progression from older to younger dates; fig. 9). Few reliable dates anchor Twfm deposition, and therefore the Twfm/Twfu contact is only loosely bracketed by the youngest stratigraphically concordant Twfm and oldest concordant Twfu dates. These dates (41.1 and 40.7 Ma) constrain the range of sedimentation rates for the Twfm between 0.22 and 0.31 mm/yr, which is 2 to 3 times more rapid than Twfl and Twfu deposition (Twfm = 305 m in <1.4 or >1.0 m.y. [ca. 42.1–>40.7 or <41.1 Ma]). The variability in accumulation rates within the Twf suggests dynamic depositional processes at the faulted basin margin that are perhaps tied to an unsteady long-term slip rate (and thus the subsidence rate) on the CGF or local waxing and waning of volcanic arc construction in the upthrown basin shoulder.

The average accumulation rate estimated at the basin periphery where subsidence is structurally controlled is understandably greater than the basin-scale accumulation rate of 0.07 mm/yr (or 66 m/m.y.) for the West Foreland Formation calculated by Finzel and others (2016). However, our estimates are subject to uncertainty of the composite thicknesses of the subunits, and how accurately the MDAs approximate the stratigraphic ages. The latter point may be particularly relevant for the MDA of the basal succession. The lowest Twf sample yields a MDA that is about 4.9 m.y. older (ca. 47.0 Ma) than the relatively narrow range of MDAs that constrain the upper two-thirds of the unit (4.0 m.y. from ca. 42.1 to 38.1 Ma), and therefore the lowest sample has an outsized influence on the rate estimate (fig. 9). If this basal MDA is several million years older than the true stratigraphic age, the accumulation rate for the entire West Foreland might be closer to the 0.15 mm/yr estimated for deposition of the upper two subunits, and more consistent with the tectonic setting and facies associations of West Foreland Formation.

Between late Eocene and early Oligocene, the sediment accumulation rate decreased considerably.

Using the approximately 200 m average basin-wide thickness of Hemlock Conglomerate (Hartman and others, 1974) that was deposited over a conservative duration of 18 Ma (late Oligocene–early Miocene) yields a maximum depositional rate of 0.016 mm/yr. This rate is much lower than that estimated by Finzel and others (2016) based on an approximately 860 m unit thickness deposited over approximately 10 m.y. (0.086 mm/yr) and falls near the lower limit for tectonically subsiding basins (Miall, 2016). Thus, the unit's low sedimentation rate, highly stable quartzose petrology and textural maturity (Calderwood and Fackler, 1972), and sheet-like distribution (Hartman and others, 1974) is consistent with long distance and duration fluvial reworking during a period of very low basin subsidence (Heller and others, 1988; Horton and others, 2004). The pairing of stable framework grains and laterally continuous sedimentary architecture resulted in a hydrocarbon reservoir interval with uncommonly high interconnectivity for the basin (Boss and others, 1976).

Zircon U–Pb stratigraphic ages of samples collected over a 100 m measured interval from a Tyonek Formation outcrop on the Beluga River render a local sediment accumulation rate of 0.14 mm/yr over a time period of about 0.7 m.y. constrained by a 15.9 Ma MDA and 15.2 Ma stratigraphic age (tonstein). This rate is nearly twice that of the conservative West Foreland Formation estimate from the Capps Glacier area, and an order of magnitude higher than basin-average Hemlock Conglomerate, but it is only about 70 percent of the time-averaged subsidence rate estimated for the Tyonek Formation near the basin axis (0.20 mm/yr, Finzel and others, 2016). Notably, a lower sedimentation rate is expected where the unit thins toward the basin margin—an area likely prone to bypass—whereas the basin axis subsidence is understandably greater. Importantly, the sedimentation rate calculated along the Beluga River reflects local, shorter-term sediment supply and accumulation rather than a long-term estimate of tectonic subsidence throughout Tyonek time (Miall, 2016).

Collectively, sediment accumulation rates near the northwestern basin margin suggest that structural subsidence progressed at a slow to moderate rate during the middle Eocene followed by a marked reduction in sedimentation rates that likely reflect diminished accommodation. Sedimentation rates subsequently accelerated during the middle Miocene accumulation of the Tyonek Formation.

## SYNTHESIS AND TECTONIC SIGNIFICANCE

The geochronologic and thermochronologic results presented here establish important new links between arc magmatism, post-magmatic cooling, brittle deformation, and subsidence at the forearc basin margin. Post-Jurassic magmatism in the upper Cook Inlet region spans the interval of ca. 84 to 38 Ma that encompasses 1) shortening of the backarc during the Middle–Late Cretaceous (Wallace and others, 1989; Ridgway and others, 2002; Hampton and others, 2010; Hults and others, 2013; Box and others, 2019), 2) revitalized latest Cretaceous–Paleocene arc magmatism that post-dated backarc shortening but was broadly coeval with initiation of transcurrent faulting at the arc-forearc basin boundary (Grantz, 1966; Wallace and others, 1989; Moll-Stalcup, 1994), 3) widespread latest Paleocene-early Eocene low-flux volcanism that lacked a subduction affinity during ongoing transcurrent faulting and arc-parallel extension (Silberman and Grantz, 1984; Cole and others, 2006; Haeussler and others, 2013; Todd and others, 2014; Todd and Jones, 2017; Helmold and others, 2018), and 4) middle Eocene re-establishment of arc magmatism (Jicha and others, 2006; Helmold and others, 2018) during transtension at the arc-forearc basin margin (Little, 1992; Gillis and others, 2017).

The forearc basin recorded dramatic changes in sediment accommodation and depositional setting during the same Late Cretaceous through middle Eocene timespan. These include 1) deepening of marine depositional systems across the forearc basin during the Campanian through Maastrichtian (Magoon and others, 1980; Trop,

2008; LePain and others, 2013; Wartes and others, 2014), 2) pre-middle Paleocene shoaling of the basin and uplift and erosion of the basin margins (Boss and others, 1976; Winkler, 1992; Shellenbaum and others, 2010), 3) rejuvenated subsidence and reorganization of the forearc basin as a terrestrial depocenter in the middle Paleocene (Boss and others, 1976; Trop and others, 2003; LePain and others, 2013), and 4) structurally controlled late Paleocene–middle Eocene sedimentation at the upper Cook Inlet-Matanuska arc-forearc basin margin (Little, 1992; Trop and others, 2003; Gillis and others, 2017).

Recent research in the Cook Inlet arc and adjacent forearc areas is providing a better understanding of their Mesozoic and Cenozoic magmatic and depositional histories (e.g., Ridgway and others, 2012; Graham and others, 2013; LePain and others, 2013; Todd and others, 2014, 2016; Finzel and others, 2015, 2016; Finzel and Enkelmann, 2017; Todd and Jones, 2017; Herriott and others, 2018; Helmold and others, 2018), but uniquely linking results and observations of these studies to specific tectonic processes remains challenging. The data presented here span a period from Late Cretaceous through Paleogene over which the continental margin of southern Alaska was subjected to as many as four, often temporally overlapping, plate-scale tectonic events that variably controlled forearc evolution, which complicates interpretation of CIB geologic datasets. These include 1) late-stage suturing of the Wrangellia composite terrane (WCT) to the continental margin during the Middle to Late Cretaceous (Wallace and others, 1989; Ridgway and others, 2002; Hampton and others, 2010; Hults and others, 2013; Box and others, 2019) to as late as late Paleocene (Cole and others, 1999), 2) inferred oroclinal bending of Alaska that resulted in counterclockwise rotation of its western region by as much as 44° between ca. 66 and 44 Ma (Hillhouse and Coe, 1994), 3) west-to-east subduction of a spreading ridge with its accompanying slab window beneath the continental margin from ca. 61 to 50 Ma (Bradley and others, 2003), and 4) a shift in subduction obliquity to a more orthogonal vector at ca. 47–43 Ma (Engebretson and others, 1985; Lonsdale, 1988; Doubrovine and Tarduno, 2008).

Relatively few studies have focused on the timing and kinematics of faults that separate the arc and forearc basin and their role in arc exhumation and basin subsidence (e.g., Gillis and others, 2009; Jones and others, 2013; Betka and others, 2017; Caine and others, 2017; Rosenthal and others, 2017). Therefore, crystallization and cooling ages of rocks cut by the basin-bounding Lake Clark and Capps Glacier faults provide important information about the timing and style of brittle deformation at the arc-forearc basin boundary. Intrusive rocks of the Neacola Mountains belong to a suite of ca. 75–66 Ma plutons that intrude the sedimentary overlap succession that conceals the WCT suture zone (Wallace and others, 1989; Moll-Stalcup, 1994). These rocks have arc to collisional chemical compositions, potentially due to crustal thickening following WCT docking with North America (Cole and Chung, 2013; Todd and Jones, 2017; this study), and were cut by the steeply southeast-dipping LCF after ca. 66 Ma crystallization of the youngest pluton in the area. Cooling of the southeast block of the LCF accelerated sharply to 49°C/m.y. from ca. 67 until 61 Ma (fig. 15), perhaps marking its initiation as a transpressional structure (fig. 16). A recent fault kinematic study of the LCF by Caine and others (2017) reveals a complex spatial and polyphase slip history that notably includes ductilely deformed intrusive rocks to the southeast placed against non-foliated granitoids to the northwest consistent with southeast-side-up cooling during the early Paleocene. Although preliminary, the cooling results imply that exhumation of the outer arc was driven by a component of contraction that was coincident with shoaling of the forearc basin and a related basin-wide unconformity, and where the deepest level of erosion and greatest angularity occur along its arc-side margin. The concurrent events may mark the transition from backarc contraction to forearc transpression after terminal collision of Wrangellia

in the latest Cretaceous (Wallace and others, 1989; Moll-Stalcup, 1994).

Differential cooling across the LCF during the middle Paleocene appears to require transtensional inversion of early to middle Paleocene transpressional faults. Rapid cooling of the northwestern upthrown fault block lags initial cooling of the southeastern downthrown block by about 4 m.y. (fig. 15), but at ca. 64 Ma accelerates to a more rapid rate in excess of 80˚C/m.y.. Presently, the LCF in this area places middle Miocene Tyonek Formation strata in its downthrown southeastern (hangingwall) block against ca. 69–66 Ma granitoids, and a nearby map-scale Riedel shear with a comparable hangingwall/footwall relationship preserves numerous fault slip indicators that define dextral transtension (Gillis and others, 2017). Therefore, the acceleration in upthrown northwestern block cooling at ca. 64–61 Ma is tentatively interpreted to approximate the time at which the LCF was reactivated as a transtensional structure (fig. 16). Additionally, available data suggest that slip on faults located 20–30 km to the north and northwest, including the dextral transtensional Capps Glacier fault (CGF), are contemporaneous with or closely post-date ca. 60 Ma cooling in the upthrown block of the LCF. Reconnaissance investigation of a ductile shear zone cutting a ca. 98 Ma granitoid northwest of the LCF produced titanite dates of ca. 60–57 Ma that are tentatively interpreted to record the timing of metamorphism during ductile deformation (Jones and others, 2013). The cursory study revealed the shear zone preserves dextral-oblique kinematic indicators and strikes at a low angle to the nearby brittle CGF that is exposed approximately 30 km to the northeast. An east-west-striking dike swarm with basaltic to andesitic compositions intrudes apparent synthetic Riedel shears in the proximal CGF granite footwall (figs. 3 and 4) and is similar in age to the youngest titanite dates, suggesting that dextral-normal slip along the fault initiated shortly after ca. 57 Ma. The transtensional dikes that intrude the Capps granite at the basin margin in the southern-most Tordrillo Mountains are similar in age and composition to a prominent sub-vertical dike swarm that cuts across the range core for over 50 km (fig. 3; Haeussler and others, 2008; Wilson and others, 2012). These north-northwest-striking dikes produce $^{40}Ar/^{39}Ar$ dates between ca. 58 and 51 Ma and bear geochemical signatures that lack a subduction affinity (Haeussler and others, 2008; Todd and Jones, 2017). They comprise up to 30 percent of some mountain-scale outcrops (Haeussler and others, 2008; 2013) and require a commensurate magnitude of northeast-southwest host rock extension to accommodate the added volume of material.

A nearly identical relationship is documented along strike to the northeast in the Talkeetna Mountains and Matanuska Valley, where mafic to intermediate volcanic rocks with primitive geochemical signatures accompany dextral transtension and northeast-southwest directed extension (fig. 21; Little, 1992; Cole and others, 2006). Extrusive rocks of the Caribou Creek volcanic field (CCVF) that bisect the Talkeetna Mountains are compositionally well characterized (Cole and others, 2006) and present the only evidence to date that appears to require a slab window beneath the forearc basin in the early Cenozoic. The CCVF is controlled by a narrow system of graben-forming north-northwest extensional faults and dikes with strikes that mimic the Tordrillo dike swarm (fig. 21). Similar to the relative orientations between the Tordrillo dikes and the CGF, the CCVF is oriented at a comparably high angle to the dextral-slip CMF (fig. 21; Oswald, 2006; Cole and others, 2006). Moreover, numerous east-west-striking dikes that are concentrated near the CMF have shallow orientations to the structure (Grantz, 1960; Fuchs, 1980, 2019) as do those associated with the CGF (fig. 21), and are likewise consistent with melt injection into synthetic transtensional Riedel shears (e.g., Tchalenko, 1970; Pollard and others, 1986). The CCVF graben area began accumulating volcanic airfall and volcaniclastic deposits as early as ca. 59 Ma, although most mafic- to intermediate-composition magmas were erupted or intruded into the graben and adjacent to the CMF from ca. 56 to

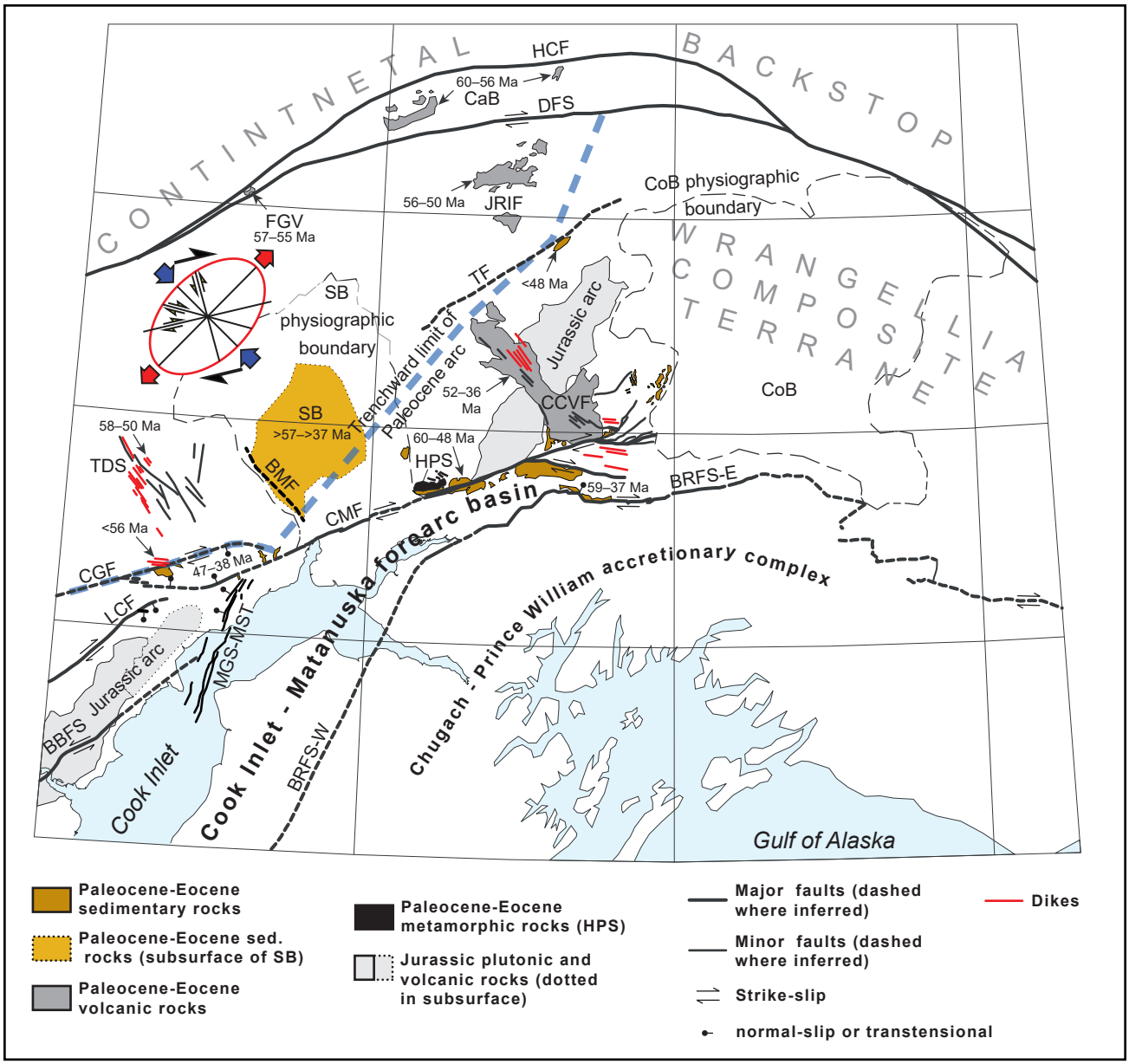


**Figure 21.** Generalized geologic map of south-central Alaska highlighting the location and ages of Paleogene sedimentary basins and contemporaneous volcanism with respect to major structural elements. Syntectonic sedimentation defined by growth strata in the Capps Glacier area and dated dikes that vary in thickness at dilatational jogs in oblique-slip faults in the Matanuska Valley indicate that deposition of thick clastic deposits at dextral fault step-overs at the Capps Glacier, Castle Mountain, and Border Ranges faults was concurrent with fault slip. Contemporaneous northwest-striking elements that project into, or abut against, the dextral-slip structures include the Tordrillo Mountains dike swarm, extensional faults and volcanism associated with the Caribou Creek volcanic field, and the Susitna basin. Coeval formation of all the Paleogene features can be accomplished in a state of regional northwest-directed principal stress. Note that the Susitna basin cuts across the trenchward limit of the Paleocene arc, and is therefore best defined as an intra-arc or successor basin rather than a continuation of the forearc basin. CGF=Capps Glacier fault, LCF=Lake Clark fault, CMF=Castle Mountain fault, BBFS=Bruin Bay fault system, MGS-MST=Middle Ground Shoal–Moquawkie structural trend, BMF=Beluga Mountain fault, BRFS-W=Border Ranges fault system, western strand, BRFS-E=Border Ranges fault system, eastern strand, DFS=Denali fault system, HCF=Hines Creek fault, CCVF=Caribou Creek volcanic field, JRIF=Jack River igneous field, FGV=Foraker Glacier volcanics, TDS=Tordrillo dike swarm, SB=Susitna basin, CoB=Copper River basin, CaB=Cantwell basin, HPS=Hatcher Pass schist.

40 Ma (Silberman and Grantz, 1984; Cole and others, 2006). Relative orientations of the north-northwest-striking dikes and CCVF to the dextral CGF and CMF, respectively, along with east-west-striking dikes proximal to both faults conform to a single horizontal strain ellipse with a southwest-northeast extension axis (fig. 21; Gillis and others, 2017). Their relation suggests a regional kinematic link between strike-slip at the basin margin and sub-parallel extension of the arc region during middle Paleocene–early Eocene volcanism.

Re-initiation of forearc depocenters followed pre-middle Paleocene uplift and erosion of the forearc basin and was synchronous with transtension, extension, and structurally controlled depleted volcanism (fig. 22). Non-marine clastic deposition into the Talkeetna–Matanuska and Cook Inlet segments of the forearc basin and the Susitna basin commenced within a few million years of each other in the late Paleocene. Strata in the Matanuska segment of the forearc basin (e.g., Arkose Ridge at ca. 60–48 Ma, Donaghy, 2012; Kortyna and others, 2013; Sunderlin and others, 2014; upper Chickaloon at ca. 56–52 Ma, Triplehorn and others, 1984; Wishbone at ca. 57–>37 Ma, Trop and others, 2003) rest unconformably on Mesozoic arc lithologies and shortened upper Cretaceous marine to terrestrial forearc rocks—achieving a composite thickness of 2,600 m or more (extrapolated from Trop and others, 2003). The oldest Cenozoic strata exposed at the surface in the CIB belong to the middle Eocene West Foreland Formation. However, Paleocene terrestrial clastic rocks have been penetrated in wells (Turner, 1986), and published interpretations informed by proprietary industry data suggest they are in angular unconformity with Maastrichtian marine strata (Boss and others, 1976; Swenson, 2001; Gregersen and Shellenbaum, 2016). The thickness of the purported Paleocene rocks is unknown, but middle Eocene West Foreland strata that overlay them range in thickness from a few hundred meters near the basin axis to over 1,000 m in the transtensional sub-basin formed between the CGF and CMF at the northwestern CIB margin (Hartman and others, 1974; LePain and others, 2013; Gillis and others, 2017). In the Susitna basin located directly north of the CIB and west of the Matanuska Valley segment of the forearc, ca. 57–54 Ma intercalated basalt, sandstone, siltstone, claystone, and conglomerate that are tentatively correlated to the Arkose Ridge Formation (Stanley and others, 2013) are penetrated in wells. Paleocene–middle Eocene strata in the basin reach a thickness of nearly 1,500 m but are truncated by a pre-Miocene unconformity.

Trop and others (2003) interpret late Paleocene–middle Eocene sedimentation into the Matanuska segment of the forearc basin to be structurally controlled by dextral-reverse motion on the CMF. Yet, deformation at the distal reaches of the CMF–CGF system to the southwest in upper Cook Inlet was likely transtensional during the late Paleocene based on the age of the mafic to intermediate dikes that intrude its synthetic Riedel shears. Regardless, dextral transtension between the CGF and CMF unequivocally controlled West Foreland Formation deposition into the Capps sub-basin at the northwest CIB margin by the middle Eocene (figs. 3 and 21; LePain and others, 2013; Gillis and others, 2017). Eocene transtension and extension are also documented along the Border Ranges fault system (BRFS) in the Matanuska Valley (Little and Naeser, 1989). Faults in that area define the trenchward boundary of the forearc basin and juxtapose Chickaloon Formation against Chugach and Peninsular terrane rocks along basinward-dipping faults. Dikes that locally thicken in dilatational jogs along some dextral faults produce zircon fission-track dates (Little, 1990) that are identical to syn-deformational West Foreland Formation strata. We therefore propose that the CGF, CMF, and segments of the Border Ranges fault system (BRFS) formed an integrated array of right-stepping dextral-slip faults from late Paleocene through the middle Eocene (fig. 21). Slip along the nearly 250 km length of the system produced apparent soft links (Walsh and Watterson, 1991) at transtensional step-overs between overlapping segments (CGF–CMF and CMF–BRFS). The thickest accu-

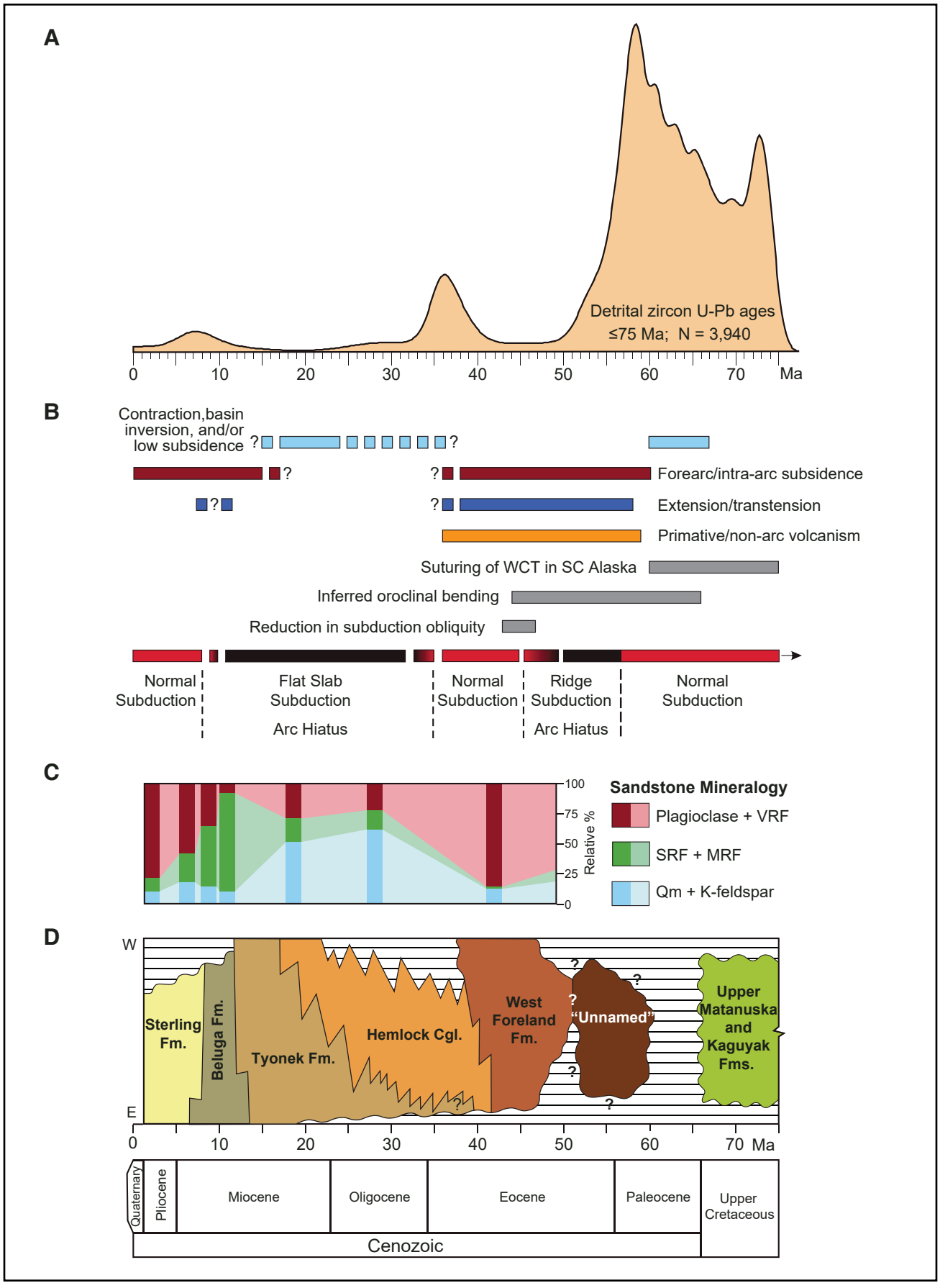
A
Detrital zircon U-Pb ages
≤75 Ma; N = 3,940
0
10
20
30
40
50
60
70
Ma
B
Contraction,basin inversion, and/or low subsidence
Forearc/intra-arc subsidence
Extension/transtension
Primative/non-arc volcanism
Suturing of WCT in SC Alaska
Inferred oroclinal bending
Reduction in subduction obliquity
Normal Subduction
Flat Slab Subduction
Arc Hiatus
Normal Subduction
Ridge Subduction
Arc Hiatus
Normal Subduction
C
Sandstone Mineralogy
Plagioclase + VRF
SRF + MRF
Qm + K-feldspar
Relative %
100
75
50
25
0
D
W
E
Sterling Fm.
Beluga Fm.
Tyonek Fm.
Hemlock Cgl.
West Foreland Fm.
"Unnamed"
Upper Matanuska and Kaguyak Fms.
0
10
20
30
40
50
60
70
Ma
Quaternary
Pliocene
Miocene
Oligocene
Eocene
Paleocene
Upper Cretaceous
Cenozoic

mulations of Paleogene sediments in the forearc were deposited in pull-apart basins at these fault step-overs and were sourced directly from their structurally uplifted margins (Little and Naeser, 1989; Trop and others, 2003; LePain and others, 2013). This model is a variation of that proposed by Pavlis and Roeske (2007), who invoked a linkage between the BRFS and the CMF to account for strike-slip duplexing inferred in the accretionary prism trench-ward of the fault system, whereas we call upon it to account for extension arc-ward of the fault system.

However, unlike the Cook Inlet and Matanuska Valley segments of the forearc basin, the Susitna basin is not in a forearc position. Rather, it cut across the trend of the Paleocene magmatic arc immediately following its zenith at ca. 58 Ma, as inferred from peak zircon occurrence (fig. 21). The basin's location between the Tordrillo dike swarm and Caribou Creek volcanic field of the same age, and its eastern and western margins that broadly parallels their strike (fig. 21) suggest that the Susitna basin initially formed as an extensional feature before its partial inversion prior to the middle Miocene (Stanley and others, 2014; Saltus and others, 2016; Shah and others, 2020). The Susitna basin's contemporaneous formation with transtensional sub-basins at the forearc margin and intercalated basalt from its deepest penetrated intervals suggests a genetic relationship between strike-slip deformation, arc-parallel extension, and mafic volcanism during waning arc magmatism (fig. 21). The structural association of the Susitna basin with oblique-slip depocenters at the forearc margin can be explained by an eastward increase in slip observed along dextral fault strands that results in parallel extension of the arc region (fig. 23A). Mechanical models of strike-slip systems predict fault-parallel extension in blocks moving away from fault terminations; commonly manifested as horsetail splay faults (e.g., Christie-Blick and Biddle, 1985). Slip magnitudes are low at the western end of the system along the LCF and CGF (10s of km; Ivanhoe, 1962; Haeussler and Saltus, 2005; Gillis and others, 2017), but increase by up to two orders of magnitude to the east (600–1000 km or more on the BRFS; fig. 23A; Roeske and others, 2003; Garver and Davidson, 2015). In between, moderate dextral slip along the CMF (fig. 23A) is inferred by lateral separation of the Jurassic intrusive rocks (Hackett, 1977) estimated at 110-130 km (Trop and others, 2005). Arc-parallel extension concentrated between the Tordrillo and Talkeetna mountains north of the fault system helps to balance the strain gradient imposed by the CMF and the western reaches of the fault system to which they are adjacent (fig. 23A). Transpressional structures associated with younger phases of deformation are

**Figure 22, page 53 (previous).** Tectonic events diagram with respect to regional zircon production, forearc deposition, and sediment provenance (modified from Helmold and others, 2018). **A.** Late Cretaceous–Cenozoic detrital zircon age distribution from Cenozoic strata and modern rivers of south-central Alaska contrasting periods of magmatic arc productivity in Late Cretaceous–Paleocene and mid- to late-Eocene times with pronounced lulls in arc activity in the early through mid-Eocene and Oligocene–mid-Miocene. **B.** Tectonic events that affected the south-central Alaska forearc region. From bottom to top: Red and black bars graphically represent periods of normal and atypical subduction, respectively. Gray bars depict periods during the Late Cretaceous and Cenozoic for which tectonic events other than ridge subduction are proposed to have affected south-central Alaska. Orange bar defines the age range of primitive and non-arc volcanism in the hinge area of the Alaska orocline. Blue bar represents the age range of forearc and intra-arc extension and transtension that coincides spatially and temporally with primitive volcanism. Maroon bars show periods of forearc and intra-arc subsidence and sedimentation. Cyan bars indicate periods of basin inversion and low sedimentation rates in the forearc region, and contraction inferred from cooling ages and structural constraints in the Neacola Mountains. **C.** Sandstone mineralogy of the Cook Inlet basin showing a general inverse correlation between compositional maturity and arc activity/sediment accommodation. Stacked darker rectangles reflect averages of samples. VRF=volcanic rock fragments, SRF=sedimentary rock fragments, MRF=metamorphic rock fragments, Qm=-monocrystalline quartz. **D.** Chronostratigraphic diagram of Cook Inlet. Note the broad time interval over which the very thin Hemlock Conglomerate (200 m thick basin-wide average) was deposited. Also, the lateral extent and thickness of the unnamed Eocene? –Paleocene strata in the Cook Inlet basin subsurface is poorly resolved. However, it is inferred that the strata are correlative to contemporaneous clastic deposits in the Matanuska Valley (Chickaloon and Wishbone formations), Talkeetna Mountains (Arkose Ridge Formation), and Paleocene/Eocene strata in the Susitna basin subsurface.

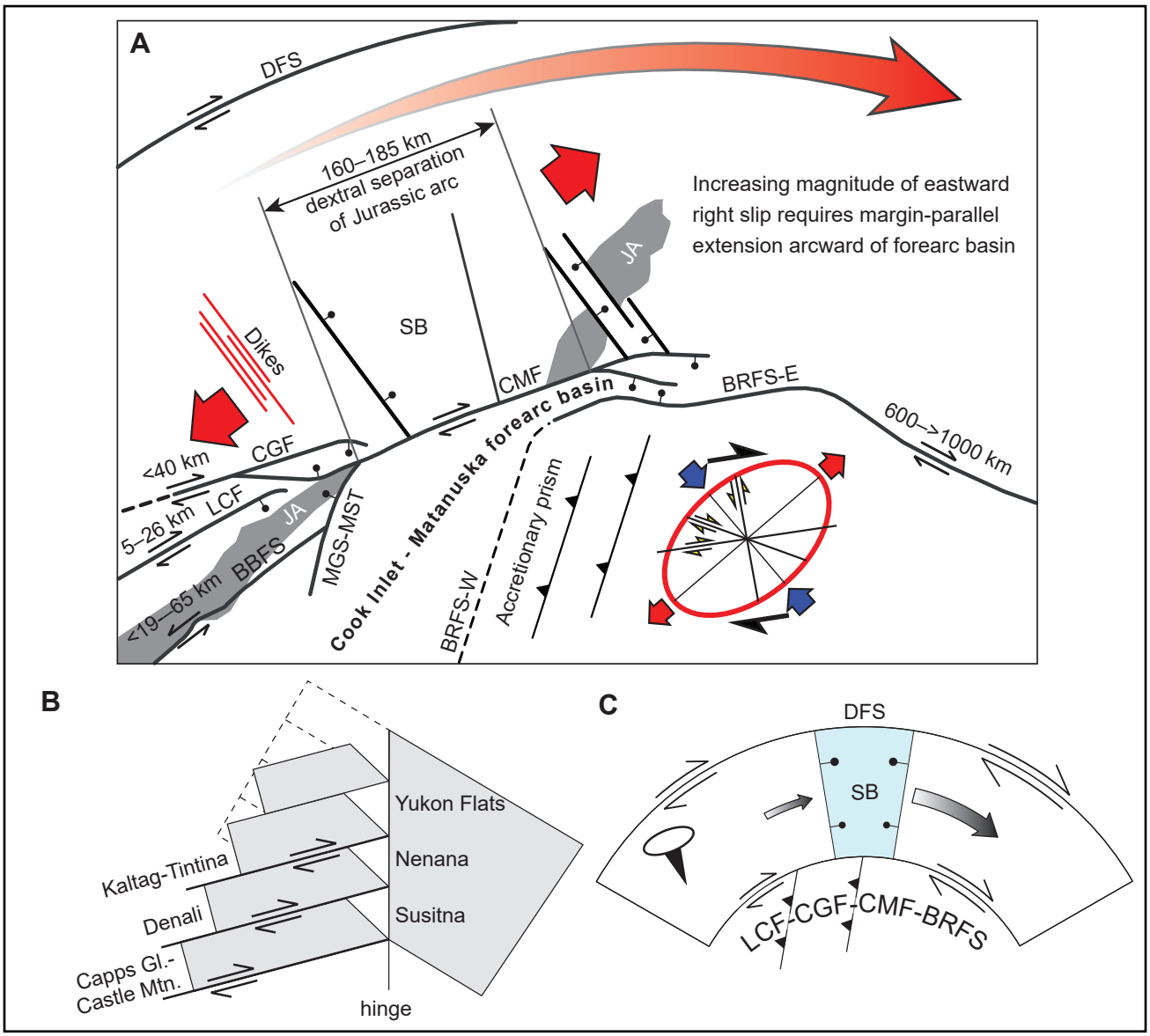


**Figure 23.** Mechanical model for coeval margin parallel strike-slip and crustal extension of the southern Alaska forearc region. **A.** The strain gradient imposed by a west to east increase in strike slip requires extension north of the fault system, contraction south of the fault system, or a combination of both to balance. Extensional features concentrated north of the Lake Clark, Capps Glacier, and Castle Mountain faults suggest some of the roughly 95–120 km of slip deficit along the system is accounted for by margin-parallel elongation of the crustal block to the north. The larger slip gradient between the Castle Mountain fault and the eastern strand of the Border Ranges fault system (>500 km) was likely partitioned by dextral slip along the western strand of the BRFS between the prism and the Cook Inlet forearc basin (CIB) prior to orthogonal bending of the fault system, followed by east-west shortening of the accretionary prism against the CIB after bending. Note that the present orientation of the western strand of the BRFS is incompatible with dextral strike-slip during northwest-directed subduction. CGF=Capps Glacier fault, LCF=Lake Clark fault, CMF=Castle Mountain fault, DFS=Denali fault system, BBFS=Bruin Bay fault system, MGS-MST=Middle Ground Shoal-Moquawkie structural trend, BRFS-W=Border Ranges fault system (western strand), BRFS-W=Border Ranges fault system (eastern strand), SB=Susitna basin. **B.** Conceptual megakink model for the Alaska orocline (Grantz, 1966; Glen, 2004) showing major strike-slip fault systems of western Alaska postulated to have facilitated bending of the lithosphere, and the location of Cenozoic sedimentary basins with respect to the oroclinal hinge that were a consequence of bending. **C.** Simple schematic diagram of a crustal block bent between two free surfaces (in this case, dextral strike-slip faults). The strain gradient that is manifested as fault slip decays to the west and forces boundary-parallel elongation (extension) of the block as it bends. DFS=Denali fault system, LCF-CGF-CMF-BRFS=the composite Lake Clark-Capps Glacier-Castle Mountain-Border Ranges fault system, SB=Susitna basin.

oriented at oblique angles to the south of the fault system in the CIB and also contribute to the westward decay in strike-slip motion (fig. 23C; Bruhn and Haeussler, 2006; Haeussler and Saltus, 2011). The large strain gradient between the CMF and BRFS was likely balanced by a component of strike-slip transferred onto the southwestern segment of the BRFS and by contraction of the accretionary prism to the south and east of the BRFS (Pavlis and Roeske, 2007). A kinematic analog for structure-parallel extension linked to an along-strike slip gradient in the Alaska forearc is the Karakoram–Gurla Mandhata–Humla fault system in southwestern Tibet and far western Nepal (Murphy and others, 2002). There, a large westward increase in strike-slip near the eastern terminus of the system is accommodated by arc-parallel extension along the Gurla Mandhata detachment.

## Implications for Ridge Subduction and Oroclinal Bending

Paleogene subduction of an active spreading ridge beneath the southern margin of Alaska is well expressed in an array of near-trench plutons that intrude the accretionary prism for ~1200 km from Sanak Island off the southern tip of the Alaska Peninsula to Baranof Island in southeast Alaska. The plutons vary systematically in age from west to east between 61 and 50 Ma, tracking the subduction direction of the ridge. However, there is considerable uncertainty about the position of the prism with respect to the continental backstop during that period. Geologic and paleomagnetic evidence suggests that the prism may have begun accreting to the margin 600–1000 km to the east prior to translation to its terminal position along the BRFS by about 50 Ma.

Predicted consequences of a ridge sweeping beneath the Alaska forearc include time transgressive 1) uplift and erosion, 2) resumption of subsidence and deposition following basin inversion, 3) a hiatus in arc magmatism with eruption of primitive volcanics and elevated heat flow in its absence, and 4) re-initiation of arc magmatism after normal subduction resumes. Each process should ideally track the position of the ridge as it sweeps from west to east along the Paleogene forearc (i.e., show an age progression that becomes younger to the east) at a rate and distance comparable to that recorded by near-trench plutonism in the prism.

Mechanical uplift above the positive topography of the migrating ridge is known to create a transient erosional welt in the forearc region and subsidence and sedimentation in its wake (Corrigan and others, 1990; Furlong and Schwartz, 2004), while a flatter subduction angle driven by progressively younger, buoyant crust toward the ridge crest temporarily extinguishes arc magmatism. The hydrated mantle wedge is also replaced by relatively hot, dry, sub-oceanic mantle welling up through the slab window formed between the subducting oceanic plates, which produces ephemeral positive dynamic topography, primitive volcanism, and high heat flow in the forearc (Thorkelson, 1996); a region otherwise characterized as a cool domain (Dumitru, 1988).

The regional angular unconformity recognized throughout much of the Alaska forearc basin, resumption of sedimentation after about 60 Ma, and subsequent waning of arc magmatism beginning at approximately 58 Ma are often held up as indirect evidence of a spreading ridge subducting beneath the continental plate (Trop and others, 2003; Trop and Ridgeway, 2007; Ridgway and others, 2012; Finzel and others, 2015, 2016). However, evidence for time-transgressive processes is generally absent continent-ward of the accretionary prism (e.g., Terhune and others, 2019). For instance, although the geologic record is incomplete and age constraints are sparse, available data suggest that resumption of forearc basin sedimentation in the Paleogene—and thus the age of the unconformity—was broadly synchronous for over 1000 km (lower Alaska Peninsula = late Paleocene–middle Eocene [Detterman and others, 1996; Finzel and Ridgway, 2017]; upper Cook Inlet = middle Eocene [this study]; Matanuska Valley/Talkeetna Mountains = late Paleocene–middle

Eocene [Triplehorn and others, 1984; Trop and others, 2003; Donaghy, 2012; Kortyna and others, 2013; Sunderlin and others, 2014].

We instead infer that shortening and erosion of the inboard forearc margin that resulted in the pre-middle Paleocene unconformity was driven by late-stage suturing of the WCT to the continental backstop, rather than by uplift and erosion above a transient ridge—at least in the upper CIB/Talkeetna–Matanuska region. $^{40}Ar/^{39}Ar$ cooling ages across the northwest side basin-bounding structures presented in this study suggest forearc transpression and exhumation began at about 67 Ma. Cooling immediately post-dated intrusion of collisional plutons into shortened Late Cretaceous backarc strata of the collapsing Kahiltna basin (Wallace and others, 1989). A compelling link between backarc and forearc deformation and sedimentation is recorded in the Cantwell basin on the continental side of the WCT suture in the central Alaska Range (CaB; fig. 21). Considered the translated remnants of a thrust-top basin (Ridgway and others, 1997), it shares a similar depositional and deformational history with the CIB positioned at the trailing edge of the colliding WCT. Upper Cretaceous strata of the lower Cantwell Formation were shortened and eroded after about 70 Ma and prior to deposition of the upper Cantwell Formation, which began at ca. 60 Ma (Cole and others, 1999). This relation is interpreted to reflect north-south shortening during terminal WCT collision with the continental backstop followed by reorganization of the suture zone as a dextral transpressional system (the Denali fault system) during northwest shortening (Ridgway and others, 1997; Cole and others, 1999). When the Denali fault is restored sinistrally using the modern-day slip rate of 5 mm/yr for the western segment of the fault (Haeussler and others, 2017), the Cantwell basin lays directly inboard of the upper CIB. Thus, contemporaneous Late Cretaceous shortening in the backarc and forearc regions, crustal thickening of the arc evidenced by collisional magmatism, followed by a structural reorganization of the backarc and forearc into transpressional domains in the Paleocene argue for a common tectonic mechanism.

The most compelling evidence for a ridge subduction event beneath the Alaska forearc are the eruption of depleted volcanic rocks during an approximately 10–12 m.y. lull in arc magmatism and coeval high upper crustal heat flow throughout much of the Eocene (Moll-Stalcup, 1994; Cole and others, 2006; Benowitz and others, 2012; Finzel and others, 2016; Terhune and others, 2019) that is consistent with disruption of the mantle wedge above a slab window. Primitive forearc magmatism that lacks arc chemical signatures corresponds with a precipitous drop in magmatic zircon production by ca. 50 Ma based on a compilation of nearly 4000 published detrital zircon dates from southern Alaska forearc basin and modern river sediments (fig. 22; Helmold and others, 2018). The chemistry of ca. 49.4–35.6 Ma CCVF rocks and, tentatively, dikes cutting the Tordrillo Mountains differ markedly from arc magmas sourced from a hydrated mantle wedge (Cole and others, 2006; Todd and Jones, 2017). Chemically, most of these rocks closely resemble slab-edge melts and primitive magmas with mid-ocean ridge basalt (N-MORB) signatures consistent with mantle upwelling through a window in the subducting slab (Cole and others, 2006). Thermochronologic data from south-central Alaska, including those presented here, support the expected presence of a regional thermal anomaly that produced an elevated Paleogene geothermal gradient of about 35 to 55°C/km (Benowitz and others, 2012; Finzel and others, 2016; Terhune and others, 2019). Although spreading ridge subduction is the most widely accepted model for the occurrence of slab window volcanics in south-central Alaska, any process that creates an opening to the asthenosphere beneath the mantle wedge is permissible; for example, tearing and foundering of the down-going slab as proposed for the area by Terhune and others (2019) or upwelling at a slab edge (Jadamec and Billen, 2010).

However, similar to the generally uniform age of the unconformity and resumption of sedimen-

tation in forearc basin depocenters beginning at about 60 Ma, little evidence exists for a west-to-east progression of primitive volcanism (Terhune and others, 2019). Rather, volcanic rocks with non-arc chemistries erupted during the magmatic lull are largely restricted to the Talkeetna–Matanuska region and parts of the central and western Alaska Range (e.g., the upper Cantwell Formation—ca. 59.8–55.5 Ma, Cole and others, 1999; Foraker Glacier volcanics—ca. 56.9–54.6 Ma, Cole and Layer, 2002; and the Jack Hills igneous field—ca. 56.0–49.5 Ma, Cole and others, 2007; fig 20). This informal volcanic province broadly lies within the north-south trending axis of the Alaska orocline (Carey, 1955). The position of the CCVF and Matanuska Valley dikes within the oroclinal axis led Cole and others (2006) to speculate that extensional structures that controlled fissure volcanism formed during oroclinal bending of Alaska. Their model accounts for localized adiabatic melting due to crustal thinning, elevated regional heat flow, and structural conduits that provide pathways for slab window magmas to erupt to the surface. Data and observations presented herein are consistent with an oroclinal bending model.

Oroclinal bending of Alaska has long been speculated (Carey, 1955), yet the processes by which it may have occurred are understudied and poorly understood. Reconnaissance paleomagnetic studies suggest up to 44˚of counterclockwise rotation of western Alaska between 66 and 44 Ma (Coe and others, 1989), ostensibly due to east-west convergence between North America and Eurasia (Grantz, 1966; Patton and Tailleur, 1977) or coastwise translation and buckling of narrow continental slivers during terrane accretion (Johnston, 2001). Mechanical and kinematic models vary for how Alaska's lithosphere might have bent, but buckling likely involved elements of megakinking (Grantz, 1966), "railroad car" or "luggage carousel" tectonics (Coe and others, 1989; Glenn, 2004), and westward crustal escape away from the oroclinal hinge (Redfield and others, 2007; Elliott and Freymueller, 2020). The megakink model, in particular, predicts characteristics that are observed inboard of the CGF-CMF-BRF system and further into interior Alaska where margin-parallel or oblique extension and formation of sedimentary basins are concentrated in the oroclinal hinge between strike-slip faults (fig. 23B; Bradley and others, 2003; Till and others, 2007).

Based on the results presented here, we broaden the footprint of crustal extension and volcanism that Cole and others, (2006) tentatively tie to oroclinal bending to encompass the approximately 40,000 km$^2$ region bounded to the west and east by the Tordrillo dike swarm and CCVF, and to the south and north by the dextral-slip CGF-CMF and Denali fault systems (including the Hines Creek fault), respectively (figs. 21 and 23A). Following Grantz (1966), we suggest that the initiation of upper CIB–Matanuska Valley dextral faults may have been a consequence of buckling of the continental margin. The BRFS separating the accretionary prism from the forearc basin has transported the Chugach terrane westward a minimum of 600–1000 km since the Late Cretaceous (Cowan, 2003; Roeske and others, 2003; Garver and Davidson, 2015), yet the segment southwest of the Matanuska Valley is at a nearly orthogonal orientation to the eastern segment (fig. 23A) and kinematically incompatible with dextral strike-slip driven by a northwestwardly subducting plate (see Doubrovine and Tarduno, 2008). This configuration suggests that the BRFS and the accretionary prism were bent after much of the strike-slip transport was complete (see also Pavlis and Roeske, 2007). However, the kinematic link between the BRFS and CMF indicates that up to 185 km of dextral slip were transferred from the accretionary prism across the forearc basin to the upper CIB dextral fault system starting at about 60 Ma— likely while bending was underway. The CIB–Matanuska faults' more linear and parallel orientation to the eastern segment of the BRFS (fig. 21) implies that it was mechanically more efficient to form new faults that radiate off the oroclinal hinge than to transport the prism around a tightening bend (fig.

21). More speculatively, similarities in structural style and timing of slip may suggest that the Denali fault evolved into an integrated continental-scale strike slip system as a consequence of oroclinal bending as well. Its curved trace parallels the CGF–CMF–BRF system (fig. 21), cutting from west to east across the Paleocene arc from the backarc to the forearc. The timing of inception of the Denali fault system is poorly resolved, but most of its approximately 400 km of dextral displacement has occurred since the Early Cenozoic; most likely after ca. 57 Ma (Nokleberg and others, 1985; Riccio and others, 2014). Together, the respective fault systems form free surfaces between which arc-parallel elongation is accommodated and may have reduced the amount of horizontal force required to bend the crust about a vertical axis (fig. 23C), analogous to how planes of weakness facilitate folding in stratified rocks. Coe and others (1989) speculated that terranes accreting northwestward against Alaska may have acted as indenters based on their observation that the curvature of the structural grain becomes tighter toward the continental margin. If so, then northwestward impingement of the Alaska promontory (the relatively narrow, weak, structurally dismembered crust west of the Canadian Shield) under east-west compression against Eurasia may have provided a mechanism for buckling, particularly if the lithosphere was thermally weakened by high heat flow from a stationary slab window (fig. 24).

Middle Eocene re-initiation of arc magmatism also appears to have been broadly coeval from about 46 to 44 Ma along a distance of over 2000 km, or may exhibit a weak younging trend to the northeast (Shew and Lanphere, 1992; Jicha and others, 2006; Amato and others, 2007). However, the oldest dated West Foreland rocks located within 300 km of the arc's northeastern limit produce abundant ca. 47 Ma zircons—likely derived from a nascent Eocene arc source (fig. 9). Transtension and struc-

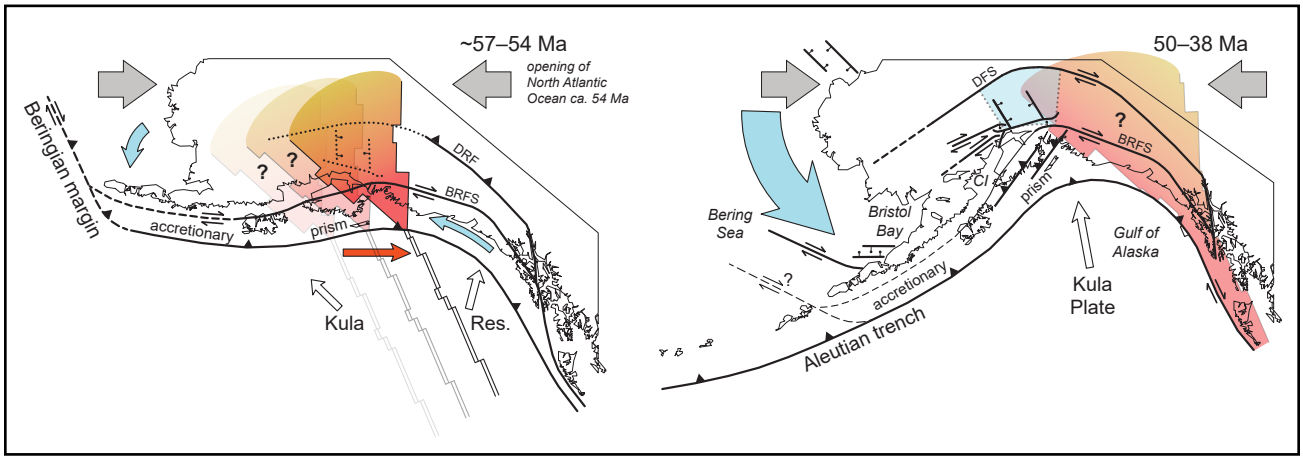


**Figure 24.** Paleocene–Eocene tectonic model for south-central Alaska in which a slab window (depicted here by as a widely-accepted west-to-east subducting spreading ridge) thermally weakened the continental lithosphere prior to formation of the Alaska orocline. Extension concentrated in the hinge of the orocline resulted from a space problem created by vertical axis rotation about a Euler pole located some distance outboard of the forearc basin. Extensional faults provided a conduit for chemically depleted volcanism sourced from sub-oceanic mantle that ascended through the slab window to erupt into the oroclinal hinge. Blue arrows depict direction of material transport. Red arrow shows migration direction of spreading ridge along the continental margin. Pale gray arrows depict convergence between the North American and Eurasian plates due to rapid opening of the North Atlantic Ocean at ca. 54 Ma (chron 24) (Rowley and Lottes,1988; Coe and others, 1989; Malinverno and others, 2020). Hollow arrows are schematic oceanic plate vectors. BRFS=Border Ranges fault system, DRF=Duke River fault, DFS=Denali fault system, Res.=Resurrection Plate, CI=Cook Inlet. **A.** Late Paleocene–early Eocene initiation of strike-slip and extensional faulting (dotted lines) during nascent buckling of the lithosphere as existing faults are progressively bent. **B.** Full development of strike-slip and extensional faulting in the hinge of the orocline by late Eocene time during major counter-clockwise rotation (44 ±11˚, Coe and others, 1989) of western Alaska.

tural subsidence continued along the upper Cook Inlet and Matanuska forearc margins until after ca. 38 Ma (youngest MDA of margin-proximal Twf). This relationship suggests that oblique subduction beneath a hydrated mantle wedge had resumed as dextral strike-slip and arc-parallel extension progressed (fig. 22B). Framework grains of West Foreland sandstones exhibit a strong volcanic signature (Helmold and others, 2018), and common intercalated tephras and lahar deposits reach thicknesses of 10–15 m, indicating close proximity to an active volcanic province no later than about ca. 42 Ma. Plutons composing the Eocene magmatic arc crop out roughly 55 km from tephra-bearing West Foreland outcrops. Although only sparsely dated, Paleogene granites that intrude parts of the Tordrillo Mountains and the arc region to the southwest overlap in age with upper West Foreland strata (e.g., the ca. 40.0–35.6 Ma Merrill Pass pluton, Reed and Lanphere, 1972; Wartes and others, 2017).

After the Eocene, transtension and subsidence at the basin margin markedly decreased. Interpretation of onshore subsurface data from northwestern upper Cook Inlet reveal that structural accommodation during Paleocene-Eocene ceased by the early to late Oligocene (Gillis and others, 2017). Directly southeast of the CMF, "un-named" Paleocene and West Foreland strata locally thicken across faults, but are overlain by a uniformly thin Hemlock Conglomerate (less than 200 m average, Hartman and others, 1974) in an apparent syn-extensional to post-extensional succession (Gillis and others, 2017). Deposition of thin, sheet-like Hemlock Conglomerate (Calderwood and Fackler, 1972) marks a reduction in basinwide sediment accumulation rates from 0.07–0.11 mm/yr to 0.02 mm/yr or less through the Oligocene during an apparent period of structural quiescence on the western side of the forearc basin. Changes in forearc basin subsidence track apparent magmatic arc productivity, which diminishes rapidly beginning at about 36 Ma and all but ceases by roughly 33 Ma (fig. 22; Finzel and others, 2011; Helmold and others, 2018). These changes indicate that plate-scale processes at the subduction margin—such as shallowing of the subduction angle soon after the Yakutat microplate enters the trench (Finzel and others, 2011; Helmold and others, 2018)—exerted a dominant control over forearc basin subsidence and composition during the Oligocene.

Sediment accumulation in the CIB increased substantially by about 15 Ma (the earliest robust geochronologic age for the Tyonek Formation), producing local accumulation rates of 0.14 mm/yr near the northwestern basin margin and 0.20 mm/yr near the basin axis (Finzel and others, 2016) that resulted in over 2,300 m of Neogene maximum stratigraphic thickness (LePain and others, 2013). These rates are an order of magnitude higher than during Hemlock deposition; however, the mechanism for middle Miocene subsidence remains speculative. As noted by Xie and Heller (2009), most sedimentary basin types have consistent subsidence mechanisms (e.g., crustal loading adjacent to foreland basins); however, forearc basin subsidence is often complex because it is dictated on a first order by a host of subduction-margin processes that vary in time and space. In the CIB, Neogene subsidence and deposition are hypothesized to be related to: a clastic wedge eroded from the uplifted upper plate above the shallowly subducting Yakutat microplate to the northeast (Finzel and others, 2011), mantle flow and related dynamic subsidence at its periphery (Haeussler and Saltus, 2011; Jadamec and others, 2013), or tectonic erosion and thinning of the forearc (Wartes and others, 2015). Additional work is required to test these hypotheses.

Sometime after the Oligocene, inherited Paleogene transtensional structures were reactivated as reverse faults (including the western segment of the CMF and Beluga River–Moquawkie fault system), likely with a component of dextral strike-slip (Bruhn and Haeussler, 2006). Contractional inversion of transtensional depocenters is best recognized in seismic profiles that show locally thick depositional packages of elevated Paleocene and Eocene strata folded in hangingwall anticlines that also deform the overlaying post-extensional

Oligocene Hemlock Conglomerate and middle to late Miocene Tyonek and Beluga formation strata (Gillis and others, 2017). We infer that late Paleogene or younger inversion of transtensional structures in the upper CIB record the onset of, or closely post-date Yakutat collision.

## CONCLUSIONS

New zircon U–Pb, multi-mineral $^{40}Ar/^{39}Ar$, and palynologic results presented in this report provide new constraints on the timing of arc activity, deformation at the basin margin, and basin subsidence in the upper Cook Inlet forearc region of southern Alaska. The results informed the following interpretations

1. Episodic arc magmatism along the forearc margin of upper Cook Inlet occurred at ca. 84–78 Ma, ca. 74–71 Ma, ca. 69–65 Ma, ca. 62–56 Ma, and ca. 47–38 Ma, and generally becomes more felsic with time. Mafic to intermediate volcanic rocks, some with within-plate geochemistries, erupted during a regional 10–12 m.y. hiatus in arc magmatism between ca. 57 and ca. 46 Ma that coincided with orogen-parallel extension of the arc region.

2. Multi-mineral $^{40}Ar/^{39}Ar$ cooling ages of granitic rocks sampled across the Lake Clark fault suggest a polyphase slip history with dextral transpression beginning at about 67 Ma, and subsequent dextral transtensional reactivation as early as 64 Ma until after 61 Ma. Latest Cretaceous–early Paleocene transpression at the arc–forearc boundary coincides with the development of a major regional angular unconformity in the forearc basin that is likely associated with regional uplift during terminal Wrangellia composite terrane collision.

3. Inception of the Capps glacier fault (CGF) as a dextral transtensional structure is bracketed between ca. 56 and 47 Ma by the age of the Capps granite and the oldest maximum depositional age (MDA) of syntectonic West Foreland Formation (Twf) cut by the fault. Whole rock $^{40}Ar/^{39}Ar$ dates of basalt and andesite dikes (<ca. 56 Ma) that intrude the Capps granite and synthetic Riedel shears to the CGF suggest that transtension began immediately after granitoid emplacement at ca. 56 Ma. Early transtension along the CGF coincides with ongoing transtension on the nearby LCF.

4. The Lake Clark, Capps Glacier, Castle Mountain, and Border Ranges faults formed a nearly 250-km-long system of soft-linked dextral transtensional structures from the late Paleocene through middle Eocene, creating local depocenters for coarse clastic sediment at extensional step-overs along the northwestern and northern margins of the forearc basin. An eastward increase in slip magnitude along the fault system resulted in orogen-parallel extension of the arc region from the Tordrillo to Talkeetna mountains. The extensional faults concentrated in the hinge of the Alaska orocline and formed conduits for magmas sourced from a depleted mantle reservoir above a slab window during a hiatus in arc magmatism.

5. Deposition of the West Foreland Formation (Twf) at the arc-forearc basin boundary was syntectonic and controlled by dextral-normal slip on the CGF, with MDAs ranging from ca. 47 to 38 Ma. Detrital zircon and conglomerate clast dates coupled with sediment composition and sedimentary facies associations indicate that proximal Twf was derived directly from the structurally uplifted margin. Twf and purported Paleocene conglomerates in the subsurface fill transtensional sub-basins concentrated at the northwestern margin of upper CIB.

6. Hemlock Conglomerate (Th) is locally as old as middle Eocene, but typically ranges from early Oligocene to possibly middle Miocene. Although its detrital zircon and quartzofeldspathic composition support a distant Yukon Tanana upland metamorphic source, distinctive volcanic conglomerate clasts known to only occur in the Eocene succession indicate that local volcanic sources were also important contributors at that time. This older, more

volcanilithic facies is partly contemporaneous with Twf deposition. The two units are interpreted to laterally inter-finger or gradationally transition away from the basin margin where alluvial fans emanating from the uplifted arc (Twf) mixed with an integrated regional axial fluvial system (Th).

7. Deposition of Hemlock Conglomerate records a protracted 18 m.y. period of extremely low sedimentation at approximately 0.016 mm/yr that reflects a time of tectonic quiescence in the forearc. The formation's high compositional and textural maturity and thin, sheet-like distribution across the entire basin suggests minimal subsidence and substantial sediment reworking during the Oligocene. This period of reduced tectonism accompanied by a hiatus in arc magmatism was a key factor in minimizing the feldspathic sediment flux from the basin margin and resulted in the deposition of the most prolific liquid hydrocarbon reservoir rock in the basin.

8. Late Paleocene to middle Eocene subsidence of the Susitna basin situated between the Tordrillo and Talkeetna mountains was likely driven by arc-parallel extension that also controlled the coeval Tordrillo dike swarm and Caribou Creek volcanic field. Although its subsidence was contemporaneous with Cook Inlet and Matanuska forearc deposition, the early Cenozoic Susitna basin cuts across the waning late Paleocene magmatic arc and is thus best defined as a distinct intra-arc or successor basin, rather than part of the forearc basin system.

## ACKNOWLEDGMENTS

Discussions with Ken Helmold, Richard Stanley, Bob Swenson, Kate Bull, Ron Cole, Ken Ridgway, Emily Finzel, Dick Reger, Jeff Trop, Jamey Jones, Erin Todd, Rick Levinson, Jake Mongrain, Richard Lease, Peter Haeussler, Richard Koehler, and Paul Betka improved our understanding of southern Alaska geology and refined our interpretations. Erin Todd kindly commented on our interpretation and discussion of the igneous geochemistry. David Doherty introduced us to the area prior to commencing field studies and provided valuable insights. Mark Schmitz kindly provided his spreadsheet for calculating maximum depositional dates. Samples were collected by Larry Freeman, David LePain, Bob Gillis, Brent Elliott, Marwan Wartes, Trystan Herriott, David Mauel, Emily Finzel, Jake Mongrain, and Ken Ridgway. University of Alaska, Fairbanks undergraduate interns Keane Richards and Kandace Krecji helped with sample logistics and data entry and provided assistance in the field. Pathfinder Aviation and pilots Merlin (Spanky) Handley, Marty Staufer, Chuck Redd, Ray Hodges, and Hightower Paxton, along with Tom (Rat) Ratledge of Yukon Helicopters, safely and skillfully transported us to every corner and creek in the field area. Jack Barber at Alaska Air Taxi flew personnel and gear to our field base camp. Bob Freeman at Three-Mile Camp kept us well fed and dry during the record-breaking 30 consecutive days of rain in the summer of 2010. Land access was kindly permitted by Cook Inlet Region, Inc. (CIRI) and Tyonek Native Corporation. This project was funded by State of Alaska Capital Improvement Project funds and the U.S. Geological Survey's National Cooperative Geologic Mapping Program STATEMAP component (award numbers G09AC00177 and G10AC00321). Reviews by Emily Finzel and James V. Jones III helped to substantially focus the manuscript and improve its contents.

## REFERENCES


Adkison, W.L., Kelley, J.S., and Newman, K.R., 1975a, Lithology and palynology of Tertiary rocks exposed near Capps Glacier and along the Chuitna River, Tyonek Quadrangle, southern Alaska: U.S. Geological Survey Open-File Report 75-21, 58 p., 1 sheet.

———1975b, Lithology and palynology of the Beluga and Sterling Formations exposed near Homer, Kenai Peninsula, Alaska: U.S. Geological Survey Open-File Report 75-383, 239 p., 1 sheet.

Ague, J.J. and Brimhall, G.H., 1988, Magmatic arc asymmetry and distribution of anomalous plutonic belts in the batholiths of California: Effects of assimilation, crustal thickness, and depth of crystallization, Geological Society of America Bulletin, v. 100, no. 6, p. 912–927.

Amato, J.M., Foley, C., Heizler, M., and Esser, R., 2007, $^{40}Ar/^{39}Ar$ and U-Pb geochronology, geochemistry, and tectonic setting of three episodes of Cretaceous–Eocene calc-alkaline magmatism in the Lake Clark Region, southwestern Alaska, Tectonic Growth of a Collisional Continental Margin, *in* Ridgway, K.D., Trop, J.M., Glen, J.M.G., and O'Neill, J.M., eds., Tectonic Growth of a Collisional Continental Margin: Crustal Evolution of Southern Alaska: Geological Society of America, Special Paper 431, p. 253–271.

Baldwin, S.L., and Lister, G.S., 1998, Thermochronology of the South Cyclades Shear Zone, Ios, Greece: Effects of ductile shear in the argon partial retention zone: Journal of Geophysical Research: Solid Earth, v. 103, no. B4, p. 7,315–7,336.

Barnes, F.F., 1966, Geology and coal resources of the Beluga–Yentna region, Alaska: U.S. Geological Survey Bulletin 1202-C., 54 p., 7 plates.

Bateman, P.C., and Dodge, F.W., 1970, Variations of major chemical constituents across the central Sierra Nevada batholith: Geological Society of America Bulletin, v. 81, no. 2, p. 409–420.

Benjamin, M.T., Johnson, N.M., and Naeser, C.W., 1987, Recent rapid uplift in the Bolivian Andes: Evidence from fission-track dating: Geology, v. 15, no. 7, p. 680–683.

Benowitz, J.A., Haeussler, P.J., Layer, P.W., O'Sullivan, P.B., Wallace, W.K., and Gillis, R.J., 2012, Cenozoic tectonothermal history of the Tordrillo Mountains, Alaska: Paleocene–Eocene ridge subduction, decreasing relief, and late Neogene faulting: Geochemistry, Geophysics, Geosystems, v. 13, no. 4. doi.org/10.1029/2011GC003951

Benowitz, J.A., Layer, P.W., and Vanlaningham, S., 2014, Persistent long-term (c. 24 Ma) exhumation in the eastern Alaska Range constrained by stacked thermochronology: Geological Society of London, Special Publication 378, no. 1, p. 225–243.

Berger, A.L., Spotila, J.A., Chapman, J.B., Pavlis, T.L., Enkelmann, E., Ruppert, N.A., and Buscher, J.T., 2008, Architecture, kinematics, and exhumation of a convergent orogenic wedge: A thermochronological investigation of tectonic–climatic interactions within the central St. Elias orogen, Alaska: Earth and Planetary Science Letters, v. 270, no. 1–2, p. 13–24.

Betka, P.M., Gillis, R.J., and Benowitz, J.A., 2017, Cenozoic sinistral transpression and polyphase slip within the Bruin Bay fault system, Iniskin–Tuxedni region, Cook Inlet, Alaska: Geosphere, v. 13, no. 6, p. 1–28. doi.org/10.1130/GES01464.1

Black, L.P., and Gulson, B.L., 1978, The age of the Mud Tank carbonatite, Strangways Range, Northern Territory: BMR Journal Australian Geology and Geophysics, v. 3, p. 227–232.

Black, L.P., Kamo, S.L., Allen, C.M., Davis, D.W., Aleinikoff, J.N., Valley, J.W., Mundil, R., Campbell, I.H., Korsch, R.J., Williams, I.S., and Foudoulis, C., 2004, Improved 206Pb/238U microprobe geochronology by the monitoring of trace-element-related matrix effect; SHRIMP, ID-TIMS, ELA-ICP-MS and oxygen isotope documentation for a series of zircon standards: Chemical Geology, v. 205, p. 15–140

Boss, R.F., Lennon, R.B., and Wilson, B.W., 1976, Middle Ground Shoal oil field, Alaska, *in* Braunstein, J., ed., North American oil and gas fields: American Association of Petroleum Geologists Memoir 24, p. 1–22.

Bowring, S.A., and Schmitz, M.D., 2003, High-precision U-Pb zircon geochronology and the stratigraphic record: Reviews in Mineralogy and Geochemistry, v. 53, no. 1, p. 305–326.

Box, S.E., Karl, S.M., Jones, J.V. III, Bradley, D.C., Haeussler, P.J., and O'Sullivan, P.B., 2019, Detrital zircon geochronology along a structural transect across the Kahiltna assemblage in the western Alaska Range: Implications for emplacement of the Alexander-Wrangellia-Peninsular terrane against North America: Geosphere, v. 15, no. 6, p. 1,774–1,808.

Bradley, D.C., Kusky, T.M., Haeussler, P.J., Goldfarb, R., Miller, M., Dumoulin, J., Nelson, S.W., and Karl, S.M., 2003, Geologic signature of early Tertiary ridge subduction in Alaska, *in* Sisson, V.B., Roeske, S.M., and Pavlis, T.L., eds., Geology of a transpressional orogeny developed during ridge-trench interaction along the North Pacific margin, Geological Society of America Special Paper 371, p. 19–49.

Bruhn, R.L., 1978, Holocene displacements measured by trenching the Castle Mountain Fault near Houston, Alaska, Short Notes on Alaskan Geology - 1978: Alaska Division of Geological & Geophysical Surveys Geologic Report 61, p. 1–4. doi.org/10.14509/407

Bruhn, R.L., and Haeussler, P.J., 2006, Deformation driven by subduction and microplate collision; geodynamics of Cook Inlet Basin, Alaska: Geological Society of America Bulletin, v. 118, p. 289–303.

Bruhn, R.L., and Pavlis, T.L., 1981, Late Cenozoic deformation in the Matanuska Valley, Alaska: Three-dimensional strain in a forearc region: Geological Society of America Bulletin, v. 92, p. 282–293. doi.org/10.1130/0016-7606(1981)92,282:LCDITM.2.0.CO;2

Burg, J.P., Davy, P., Nievergelt, P., Oberli, F., Seward, D., Diao, Z., and Meier, M., 1997, Exhumation during crustal folding in the Namche-Barwa syntaxis: Terra Nova, v. 9, no. 2, p. 53–56.

Caine, J.S., Todd, E., Lease, R.O, and Jones, J.V. III, 2017, Transpression and transtension along the Lake Clark fault in south-central Alaska: new views on its formation, characteristics, damage, kinematics, exhumation, and evolution: Geological Society of America Abstracts with Programs, v. 49, no. 6.

Calderwood, K.W., and W.C. Fackler, 1972, Proposed stratigraphic nomenclature for Kenai Group, Cook Inlet Basin, Alaska: American Association of Petroleum Geologists Bulletin, v. 56, p. 739–754.

Campbell, I.H., Ballard, J.R., Palin, J.M., Allen, C., and Faunes, A., 2006, U-Pb zircon geochronology of granitic rocks from the Chuquicamata–El Abra porphyry copper belt of northern Chile: Excimer laser ablation ICP-MS analysis: Economic Geology, v. 101, no. 7, p. 1,327–1,344.

Candela, P.A., 1997, A Review of Shallow, Ore-related Granites: Textures, Volatiles, and Ore Metals: Journal of Petrology, v. 38, no. 12, p. 1,619–1,633. doi.org/10.1093/petroj/38.12.1619

Carey, S.W., 1955, The orocline concept in geotectonics-Part I: Papers and proceedings of the Royal Society of Tasmania, v. 89, p. 255–288.

Chang, Z., Vervoort, J.D., McClelland, W.C., and Knaack, C., 2006, U-Pb dating of zircon by LA-ICP-MS: Geochemistry, Geophysics, Geosystems, v. 7, no. 5.

Charlier, B.L.A., Wilson, C.J.N., Lowenstern, J.B., Blake, S., Van Calsteren, P.W., and Davidson, J.P., 2005, Magma generation at a large, hyperactive silicic volcano (Taupo, New Zealand) revealed by U-Th and U-Pb systematics in zircons, Journal of Petrology, v. 46, no. 1, p. 3–32.

Chen, J.H., and Moore, J.G., 1982, Uranium-lead isotopic ages from the Sierra Nevada batholith, California: Journal of Geophysical Research: Solid Earth, v. 87, no. B6, p. 4,761–4,784.

Christie-Blick, N., and Biddle, K.T., 1985, Deformation and basin formation along strike-slip faults, *in* Biddle, K.T., and Christie-Blick, N., eds., 1985, Strike-slip Deformation, Basin Formation, and Sedimentation: Society of Sedimentary Geology Special Publication 37, p. 1–34.

Claypool, G.E., Threlkeld, C.N., and Magoon, L.B., 1980, Biogenic and thermogenic origins of natural gas in Cook Inlet Basin, Alaska: American Association of Petroleum Geologists Bulletin, v. 64, p. 1,131–1,139.

Cohen, K.M., Finney, S.C., Gibbard, P.L., and Fan, J.X., 2013; updated, The ICS International Chronostratigraphic Chart: Episodes 36: p. 199–204.

Coe, R.S., Globerman, B.R., and Thrupp, G.A., 1989, Rotation of central and southern Alaska in the early Tertiary: Oroclinal bending by megakinking?, *in* Kissel, C., and Laj, C., eds., Paleomagnetic rotations and continental deformation: Springer, Dordrecht, p. 327–342.

Cole, R.B., and Chung, S., 2013, Late Cretaceous to Eocene progression of arc and collisional magmatism in south-central Alaska: Abstracts and Programs, v. 45, no. 7, p.165, Geological Society of America Annual Meeting, Denver, CO, Oct. 27–30.

Cole, R.B., and Layer, P.W., 2002, Stratigraphy, age, and geochemistry of Tertiary volcanic rocks and associated synorogenic deposits, Mount McKinley Quadrangle, Alaska, *in* Wilson, F.H., and Galloway, J.P., eds., Studies by the U.S. Geological Survey in Alaska, 2000: U.S. Geological Survey Professional Paper 1662, p. 19–43.

Cole, R.B., Layer, P.W., Hooks, B., Cyr, A., and Turner, J., 2007, Magmatism and deformation in a terrane suture zone south of the Denali fault, northern Talkeetna Mountains, Alaska, *in* Ridgway, K.D., Trop, J.M., Glen, J.M.G., and O'Neill, J.M., eds., Tectonic Growth of a Collisional Continental Margin: Crustal Evolution of Southern Alaska: Geological Society of America Special Paper 431, p. 477–506. doi.org/10.1130/2007.2431(19)

Cole, R.B., Ridgway, K.D., Layer, P.L., and Drake, J., 1999, Kinematics of basin development during the transition from terrane accretion to strike-slip tectonics, Late Cretaceous-early Tertiary Cantwell Formation, south-central Alaska: Tectonics, v. 18, no. 6, p. 1,224–1,244.

Cole, R.B., Nelson, S.W., Layer, P.W., and Oswald, P.J., 2006, Eocene volcanism above a depleted mantle slab window in southern Alaska: Geological Society of America Bulletin, v. 118, no. 1–2, p. 140–158.

Coleman, D.S., Gray, W., and Glazner, A.F., 2004, Rethinking the emplacement and evolution of zoned plutons: Geochronologic evidence for incremental assembly of the Tuolumne Intrusive suite, California: Geology, v. 32, no. 5; p. 433–436. doi.org/10.1130/G20220.1

Corrigan, J., Mann, P., and Ingle, J.C., 1990, Forearc response to subduction of the Cocos Ridge, Panama-Costa Rica: Geological Society of America Bulletin, v. 102, p. 628–652.

Coutts, D.S., Matthews, W.A., and Hubbard, S.M., 2019, Assessment of widely used methods to derive depositional ages from detrital zircon populations: Geoscience Frontiers, v. 10, p. 1421–1435. doi.org/10.1016/ j.gsf.2018.11.002

Cowan, D.S., 2003, Revisiting the Baranof–Leech River hypothesis for early Tertiary coastwise transport of the Chugach–Prince William terrane: Earth and Planetary Science Letters, v. 213, no. 3–4, p. 463–475.

Dadson, S.J., Hovius, N., Chen, H., Dade, W.B., Hsieh, M.L., Willett, S.D., Hu, J.C., Horng, M.J., Chen, M.C., Stark, C.P., and Lague, D., 2003, Links between erosion, runoff variability and seismicity in the Taiwan orogeny: Nature, v. 426, no. 6967, p. 648.

Dallegge, T.A., and Layer, P.W., 2004, Revised chronostratigraphy of the Kenai Group from $^{40}Ar/^{39}Ar$ dating of low potassium bearing minerals, Cook Inlet Basin, Alaska: Canadian Journal of Earth Science, v. 41, p. 1159–1179.

Davis, J.W., 2010, Thermochronology and cooling histories of plutons: Implications for incremental pluton assembly: Ph.D. dissertation, University of North Carolina at Chapel Hill, 132 p.

Davis, J.W., Coleman, D.S., Gracely, J.T., Gaschnig, R., and Stearns, M., 2012, Magma accumulation rates and thermal histories of plutons of the Sierra Nevada batholith, CA: Contributions to Mineralogy and Petrology, v. 163, no. 3, p. 449–465.

DeGraaff-Surpless, K., Graham, S.A., Wooden, J.L., and McWilliams, M.O., 2002, Detrital zircon provenance analysis of the Great Valley Group, California: Evolution of an arc-forearc system: Geological Society of America Bulletin: v. 114 no. 12, p. 1,564–1,580. doi.org/10.1130/0016-7606(2002)114<1564:DZPAOT>2.0.CO;2

Delaney, P.T., Pollard, D.D., Ziony, J.I., and McKee, E.H., 1986, Field relations between dikes and joints: emplacement processes and paleostress analysis: Journal of Geophysical Research: Solid Earth, v. 91, no B5, p. 4,920–4,938.

Detterman, R.L., Case, J.E., Miller, J.W., Wilson, F.H., and Yount, M.E., 1996, Stratigraphic framework of the Alaska Peninsula: U.S. Geological Survey Bulletin 1969-A, 74 p.

Detterman, R.L., and Hartsock J.K., 1966, Geology of the Iniskin–Tuxedni Peninsula region, Alaska: U.S. Geological Survey Professional Paper 512, 78 p., 7 plates.

Detterman, R.L., Hudson, T., Plafker, G., Tysdal, R.G., and Hoare, J.M., 1976a, Reconnaissance geologic map along Bruin Bay and Lake Clark faults in Kenai and Tyonek Quadrangles, Alaska: U.S. Geological Survey Open-file Map 76-477, scale 1:250,000.

Detterman, R.L., Plafker, G., Hudson, T., Tysdal, R.G., and Pavoni, N., 1974, Surface geology and Holocene breaks along the Susitna segment of the Castle Mountain fault, Alaska: U.S. Geological Survey Map MF-618, scale 1:24,000.

Detterman, R.L., Plafker, G., Tysdal, R.G., and Hudson, T., 1976b, Geology and surface features along part of the Talkeetna segment of the Castle Mountain-Caribou fault system, Alaska: U.S. Geological Survey Miscellaneous Field Studies Map 738, 1 sheet, scale 1:63,360.

Detterman, R.L., and Reed, B.L., 1980, Stratigraphy, structure, and economic geology of the Iliamna Quadrangle, Alaska: U.S. Geological Survey Bulletin 1368-B, 86 p., scale 1:250,000, 1 plate.

Dickinson, W.R., 1985, Interpreting provenance relations from detrital modes of sandstones, *in* Zuffa, G.G., ed., Provenance of Arenites: NATO Advanced Science Institutes Series C: Mathematical and Physical Sciences, v. 148, D. Reidel Publishing Co., p. 333–361.

———1995, Forearc basins, *in* Busby, C.J., and Ingersoll, R. V., eds., Tectonics of sedimentary basins, Cambridge, Massachussetts, USA, Blackwell Science, p. 221–261.

Dickinson, W.R., and Gehrels, G.E., 2009, Use of U-Pb ages of detrital zircons to infer maximum depositional ages of strata: a test against a Colorado Plateau Mesozoic database: Earth and Planetary Science Letters, v. 288, p. 115–125.

Dodson, M.H., 1973, Closure temperature in cooling geochronological and petrological systems: Contributions to Mineralogy and Petrology, v. 40, no. 3, p.259–274.

Donaghy, 2012, Sedimentology, depositional age, and provenance of sedimentary and volcanic rocks exposed along Willow Creek, eastern Susitna basin, south-central Alaska: Implications for modification of a forearc basin by spreading ridge subduction: B.S. Honors thesis, Bucknell University, 134 p.

Donelick, R.A., O'Sullivan, P.B., and Donelick, M.B., 2009, A discordia-based method of zircon U-Pb dating from LA-ICP-MS analysis of single spots: Proceedings of the 10th Biennial Meeting of the Society for Geology Applied to Mineral Deposits, Townsville, Australia, August 17–20, 2009, p. 276–278.

Donelick, R.A, O'Sullivan, P.B., and Ketcham, R.A., 2005, Apatite fission-track analysis: Reviews in Mineralogy and Geochemistry, Mineralogical Society of America, v. 58, p. 49–94.

Dorsey, R.J., Housen, B.A., Janecke, S.U., Fanning, C.M., and Spears, A.L., 2011, Stratigraphic record of basin development within the San Andreas fault system: Late Cenozoic Fish Creek–Vallecito basin, southern California: Geological Society of America Bulletin, v. 123, no. 5–6, p. 771–793.

Doubrovine, P. V., and Tarduno, J.A., 2008, A revised kinematic model for the relative motion between Pacific oceanic plates and North America since the Late Cretaceous: Journal of Geophysical Research, v. 113, no. B12101. doi.org/10.1029/2008JB005585

Dumitru, T.A., 1988, Subnormal geothermal gradients in the Great Valley forearc basin, California, during Franciscan subduction: A fission track study: Tectonics, v. 7, no. 6, p. 1,201–1,221.

Dusel-Bacon, C., Aleinikoff, J.N., Day, W.C., and Mortensen, J.K., 2015, Mesozoic magmatism and timing of epigenetic Pb-Zn-Ag mineralization in the western Fortymile mining district, east-central Alaska: Zircon U-Pb geochronology, whole-rock geochemistry, and Pb isotopes, Geosphere, v. 11, no. 3, p. 786–822.

Dusel-Bacon, C., Holm-Denoma, C.S., Jones, J.V., Aleinikoff, J.N., and Mortensen, J.K., 2017, Detrital zircon geochronology of quartzose metasedimentary rocks from parautochthonous North America, east-central Alaska: Lithosphere, v. 9, no. 6, p. 927–952.

Ehlers, T.A., 2005, Crustal thermal processes and the interpretation of thermochronometer data: Reviews in Mineralogy and Geochemistry, v. 58, no. 1, p. 315–350.

Elliott, Julie, and Freymueller, J.T., 2020, A Block Model of Present-Day Kinematics of Alaska and Western Canada: Journal of Geophysical Research, v. 125, no. 7, p.e2019JB018378.

Engebretson, D. C., Cox, A., and Gordon, R.G., 1985, Relative motions between oceanic and continental plates in the Pacific basin: Geological Society of America Special Paper 206, 59 p.

Enkelmann, E., Sanchez Lohff, S.K., and Finzel, E.S., 2019, Detrital zircon double-dating of forearc basin strata reveals magmatic, exhumational, and thermal history of sediment source areas: Geological Society of America Bulletin, v. 131, no. 7–8, p. 1,364–1,384.

Finzel, E.S., and Enkelmann, E., 2017, Miocene-Recent sediment flux in the south-central Alaskan fore-arc basin governed by flat-slab subduction: Geochemistry, Geophysics, Geosystems, v. 18, no. 4, p. 1,739–1,760. doi.org/10.1002/2016GC006783

Finzel, E.S., Enkelmann, E., Falkowski, S., and Hedeen, T., 2016, Long-term fore-arc basin evolution in response to changing subduction styles in southern Alaska: Tectonics, v. 35, p. 1,735–1,759. doi.org/10.1002/2016TC004171

Finzel, E.S., and Ridgway, K.D., 2017, Links between sedimentary basin development and Pacific basin plate kinematics recorded in Jurassic to Miocene strata on the western Alaska Peninsula: Lithosphere, v. 9, no. 1, p. 58–77.

Finzel, E.S., Ridgway, K.D., and Trop, J.M., 2015, Provenance of the Cook Inlet forearc basin, southern Alaska: investigating the effects of Cenozoic spreading-ridge and flat-slab subduction on sediment transport along convergent margins: Geosphere, v. 11, no. 3. doi.org/L10.1130/GES0129.1

Finzel, E.S., Trop, J.M., Ridgway, K.D., and Enkelmann, E., 2011, Upper-plate proxies for flat-slab subduction processes in southern Alaska: Earth and Planetary Sciences Letters, v. 303, p. 348–360.

Fleck, R.J., Sutter, J.F., and Elliot, D.H., 1977, Interpretation of discordant $^{40}Ar/^{39}Ar$ age-spectra of Mesozoic tholeiites from Antarctica: Geochimica et Cosmochimica Acta, v. 41, no. 1, p. 15–32.

Flores, R.M., Stricker, G.D., and Roberts, S.B., 1994, Miocene coal-bearing strata of the Tyonek Formation: Braided stream deposits in the Chuit Creek–Chuitna River drainage basin, southern Alaska, *in* Till, A.B., and Moore, T.E., eds., Geologic studies in Alaska by the U.S. Geological Survey Bulletin 2107, p. 95–114.

Foland, K.A., 1974, Ar40 diffusion in homogenous orthoclase and an interpretation of Ar diffusion in K-feldspars: Geochimica et Cosmochimica Acta, v. 38, no. 1, p.151–166.

Foster, D.A., and Fanning, C.M., 1997, Geochronology of the northern Idaho batholith and the Bitterroot metamorphic core complex: Magmatism preceding and contemporaneous with extension: Geological Society of America Bulletin: v. 109, no. 4, p. 379–394. doi.org/10.1130/0016-7606(1997)109<0379:GOTNIB>2.3.CO;2

Freeman, L.K., Gillis, R.J., Elliott, B.A., and Wypych, Alicja, 2016, Major-oxide and trace-element geochemical data from rocks collected in 2010 in the Tyonek Quadrangle, Alaska: Alaska Division of Geological & Geophysical Surveys Raw Data File 2016-5, 2 p. doi.org/10.14509/29651

Frost, R.B., Barnes, C.G, Collins, W.J., Arculus, R.J., Ellis, D.J., and Frost, C.D., 2001, A geochemical classification for granitic rocks: Journal of Petrology, v. 42, no. 11, p. 2,033–2,048. doi.org/10.1093/petrology/42.11.2033

Fuchs, W.A., 1980, Tertiary tectonic history of the Castle Mountain Fault System in the Talkeetna Mountains, Ph.D. dissertation: University of Utah, Salt Lake City, Utah, 152 p.

———Geologic map of the Castle Mountain–Caribou fault system, Talkeetna Mountains, Alaska: Alaska Division of Geological & Geophysical Surveys Preliminary Interpretive Report 2017-2, 57 p., 2 sheets, scale 1:24,000. doi.org/10.14509/29715

Furlong, K.P., and Schwartz, S.Y., 2004, Influence of the Mendocino triple junction on the tectonics of coastal California: Annual Review of Earth and Planetary Science, v. 32, p. 403–433.

Garver, J.I., and Davidson, C.M., 2015, Southwestern Laurentian zircons in upper Cretaceous flysch of the Chugach–Prince William terrane in Alaska: American Journal of Science, v. 315, no. 6, p. 537–556.

Giletti, B.J., 1974, Studies in diffusion I: Argon in phlogopite mica, *in* Hoffmann, A.W., Giletti, B.J., Yoder, H.S. Jr., and Yund, R.A., eds., Geochemical Transport and Kinetics: Carnegie Institute of Washington Publications, 634, p. 107–115.

Gillis, R.J., LePain, D.L., Herriott, T. M., Wartes, M. A., Benowitz, J.A., and O'Sullivan, P.B., 2017, Results of 1:63,360-scale geologic mapping and related field studies in the south-central Tyonek Quadrangle, south-central Alaska: Late Paleocene(?)–middle Eocene transtension and post-Oligocene inversion on the northwest periphery of the Cook Inlet forearc basin: Pacific Section American Association of Petroleum Geologists Annual Conference, Anchorage, Alaska, May 21–24.

Gillis, R.J., LePain, D.L., Ridgway, K.D., and Finzel, E.S., 2009, A reconnaissance view of an unnamed fault near Capps Glacier, northwestern Cook Inlet basin, and its potential as a regional-scale, basin-controlling structure: Alaska Division of Geological & Geophysical Surveys Preliminary Interpretive Report 2009-3, 9 p. doi.org/10.14509/19503

Gillis, R. J., Shellenbaum, D.P., Herriott, T. M., Wartes, M. A., Mauel, D., Decker, P.L., Fair, H.S, LePain, D. L., and Gregersen, L.S., in preparation, 1:63,360-scale interpretive bedrock geologic map and report of the south-central Tyonek Quadrangle, Alaska: Late Paleocene(?)-middle Eocene transtension and post-Oligocene inversion on the northwest periphery of the Cook Inlet forearc basin: Alaska Division of Geological & Geophysical Surveys Report of Investigation.

Glazner, A.F., Bartley, J.M., Coleman, D.S., Gray, W., and Taylor, R.Z., 2004, Are all plutons assembled over millions of years by amalgamation from small magma chambers?: Geological Society of America Today, v. 14; no. 4/5, p. 4–12. doi.org/10.1130/1052-5173(2004)014<0004:APAOMO>2.0.CO;2

Graham, G.E., Goldfarb, R.J., Miller, M.L., Gibler, K., and Roberts, M., 2013, Tectonic evolution and Cretaceous gold metallogenesis of southwestern Alaska: Society of Economic Geologists Special Publication, v. 17, p. 169–200.

Grantz, A., 1960, Generalized geologic map of the Nelchina area, Alaska, showing igneous rocks and larger faults: U.S. Geological Survey Miscellaneous Geologic Investigations Map 312, 1 sheet, scale 1:96,000.

———1965, Geologic map and cross-sections of the Nelchina area, south-central Alaska: U.S. Geological Survey Open-File Report 65-65, scale 1:63,360, 4 sheets.

———1966, Strike-slip faults in Alaska: U.S. Geological Survey Open-file Report 66-53, 82 p.

Gregersen, L.S., and Shellenbaum, D.P., 2016, Top Mesozoic unconformity subcrop map, Cook Inlet basin, Alaska: Alaska Division of Geological & Geophysical Surveys Report of Investigation 2016-4, 1 sheet, scale 1:500,000. doi.org/10.14509/29658

Grove, M., and Harrison, T.M., 1996, 40Ar* diffusion in Fe-rich biotite: American Mineralogist, v. 81, p. 940–951.

Hackett, S.W., 1976, Regional gravity survey of Beluga basin and adjacent area, Cook Inlet region, south-central Alaska: Alaska Open-file Report 100, 38 p.

Haeussler, P.J., Best, T.C., and Waythomas, C.F., 2002, Paleoseismology at high latitudes: Seismic disturbance of upper Quaternary deposits along the Castle Mountain fault near Houston, Alaska: GSA Bulletin, v. 114, p. 1,296–1,310.

Haeussler, P.J., Bradley, D.C. and Goldfarb, R.J., 2003, Brittle deformation along the Gulf of Alaska margin in response to Paleocene-Eocene triple junction migration: Geological Society of America Special Papers, p. 119–140.

Haeussler, P. J., Bradley, D.C., Ayuso, R., Layer, P.W., Friedman, R., O'Sullivan, P., Karl, S.M., Jones, J.V. III, and Todd, E., 2013, Magmatic history of the Tordrillo Mountains and western Alaska Range and tectonic implications: Geological Society of America Abstracts with Programs, v. 48, n. 7, Geological Society of America Annual Meeting, Denver, CO, Oct. 27–30.

Haeussler, P. J., Bradley, D., Ayuso, R. Layer, P.W., Friedman, R., O'Sullivan, P., Miller, M., and Karl, S., 2009, The new U.S. Geological Survey Western Alaska Range Project and precursory results from the Tyonek Quadrangle: paper presented at Annual Convention, Alaska Miners Assoc., Anchorage.

Haeussler, P.J., Bruhn, R.L., and Pratt, T.L., 2000, Potential seismic hazards and tectonics of the upper Cook Inlet basin, Alaska, based on analysis of Pliocene and younger deformation: Geological Society of America Bulletin, v. 112, p.1,414–1,429. doi.org/10.1130/0016-7606(2000)112,1414:PSHATO.2.0.CO;2

Haeussler, P.J., Matmon, A., Schwartz, D.P., and Seitz, G.G., 2017, Neotectonics of interior Alaska and the late Quaternary slip rate along the Denali fault system: Geosphere, v. 13, no. 5, p. 1,445–1,463. doi.org/10.1130/GES01 447.1

Haeussler, P.J., O'Sullivan, Paul, Berger, A., and Spotila, J., 2008, Neogene exhumation of the Tordrillo Mountains, Alaska, and correlations with Denali (Mount McKinley), *in* Freymueller, J.T., Haeussler, P.J., Wesson, R.L., and Ekström, Göran, eds., Active Tectonics and Seismic Potential of Alaska: Geophysical Monograph Series, v. 179, Washington D.C., American Geophysical Union, p. 269–285. doi.org/10.1029/179GM15

Haeussler, P.J., and Saltus, R.W., 2005, 26 km of offset on the Lake Clark fault since late Eocene time: *in* Haeussler, P.J. and J.P. Galloway, eds., Studies by the U.S. Geological Survey in Alaska: U.S. Geological Survey Professional Paper 1709-A, 4 p.

———2011, Location and extent of Tertiary structures in Cook Inlet Basin, Alaska, and mantle dynamics that focus deformation and subsidence: U.S. Geological Survey Professional Paper 1776-D, 26 p.

Hampton, B.A., Ridgway, K.D., and Gehrels, G.E., 2010, A detrital record of Mesozoic island arc accretion and exhumation in the North American Cordillera: U-Pb geochronology of the Kahiltna basin, southern Alaska: Tectonics, v. 29, p. 4.

Harlan, S.S., Vielreicher, R.M., Mortensen, J.M., Bradley, D.C., Goldfarb, R.J., Snee, L.W. and Till, A.B., 2017, Geology and Timing of Ore Formation in the Willow Creek Gold District, Talkeetna Mountains, Southern Alaska: Economic Geology, v. 112, no. 5, p. 1,177–1,204.

Harrison, T.M., 1981, Diffusion of 40Ar in hornblende: Contributions to Mineralogy and Petrology, v. 78, p. 324–331.

Harrison, T.M., Duncan, Ian, and McDougall, Ian, 1985, Diffusion of 40Ar in biotite: Temperature, pressure, and compositional effects: Geochimica et Cosmochimica Acta, v. 49, p. 2,461–2,468.

Hart, C.J.R., Goldfarb, R.J., Lewis, L.L. and Mair, J.L., 2004, The Northern Cordilleran Mid-Cretaceous Plutonic Province: Ilmenite/Magnetite-series Granitoids and Intrusion-related Mineralisation: Resource Geology, v. 54, no. 3, p. 253–280.

Harrison, T.M., and McDougall, I., 1981, Excess $^{40}Ar$ in metamorphic rocks from Broken Hill, New South Wales: implications for $^{40}Ar/^{39}Ar$ age spectra and the thermal history of the region: Earth and Planet Science Letters, v. 55, p. 123–149.

Hartman, D.C., Pessel, G.H., and McGee, D.L., 1974, Stratigraphy of the Kenai group, Cook Inlet: Alaska Division of Geological & Geophysical Surveys Open-File Report 49, 7 p., 11 sheets. doi.org/10.14509/149

Heizler, M.T., and Harrison, T.M., 1988, Multiple trapped argon isotope components revealed by $^{40}Ar^{39}Ar$ isochron analysis: Geochimica et Cosmochimica Acta, v. 52, no. 5, p.1295–1303.

Heller, P.L., Angevine, C.L., Winslow, N.S., and Paola, C., 1988, Two-phase stratigraphic model of foreland-basin sequences: Geology, v. 16, n. 6, p.501–504.

Helmold, K.P., Wartes, M.A., Gillis, R.J., LePain, D.L., Herriott, T.M., Stanley, R.G., and Wilson, M.D., 2018, Secular changes in Cenozoic arc magmatism recorded by trends in forearc basin sandstone composition, Cook Inlet, southern Alaska: in Tectonics, Sedimentary Basins, and Provenance: A Celebration of William R. Dickinson's Career: Geological Society of America Special Paper 540, p. 591–615.

Herriott, T.M., Crowley, J.L., Schmitz, M.D., Wartes, M.A., and Gillis, R.J., 2019, Exploring the law of detrital zircon: LA-ICP-MS and CA-TIMS geochronology of Jurassic forearc strata, Cook Inlet, Alaska, USA: Geology, v. 47, no. 11, p.1,044–1,048.

Herriott, T.M., Wartes, M.A., Stanley, R.G., Decker, P.L., Helmold, K.P., and Harun, N.T., 2018, Sequence-stratigraphic framework of the Middle Jurassic Chinitna Formation, Cook Inlet forearc basin, south-central Alaska (presentation): Alaska Geological Society, 20 March 2018, Anchorage, Alaska: Alaska Division of Geological & Geophysical Surveys, 77 p. doi.org/10.14509/30031

Hildreth, Wes, 2001, A critical overview of silicic magmatism: in Penrose Conference on Longevity and Dynamics of Rhyolitic Magma Systems, Mammoth, CA, p. 6–12.

Hillhouse, J.W., and Coe, R.S., 1994, Paleomagnetic data from Alaska, *in* Plafker, G., and Berg, H.C., eds., The geology of Alaska: Boulder, Colorado, Geological Society of America, The Geology of North America, v. G-1, p. 797–812.

Horowitz, Aharon, 1989, Palynological evidence for the Quaternary rates of accumulation along the Dead Sea Rift, and structural implications: Tectonophysics, v. 164, no. 1, p. 63–71.

Horstwood, M.S., Košler, J., Gehrels, G., Jackson, S.E., McLean, N.M., Paton, C., Pearson, N.J., Sircombe, K., Sylvester, P., Vermeesch, P., and Bowring, J.F., 2016, Community-derived standards for LA-ICP-MS U-(Th-) Pb geochronology–Uncertainty propagation, age interpretation and data reporting: Geostandards and Geoanalytical Research, v. 40, no. 3, p. 311–332.

Horton, B.K., Constenius, K.N. and DeCelles, P.G., 2004, Tectonic control on coarse-grained foreland-basin sequences: An example from the Cordilleran foreland basin, Utah: Geology, v. 32, no. 7, p. 637–640.

Hudson, T.L., 1986, Plutonism and provenance—implications for sandstone compositions, *in* Magoon, L. B., ed., Geologic studies of the Lower Cook Inlet COST no. 1 well, Alaska Outer Continental Shelf: U.S. Geological Survey Bulletin, 1596, p. 55–60.

Hults, C.P., Wilson, F.H., Donelick, R.A., and O'Sullivan, P.B., 2013, Two flysch belts having distinctly different provenance suggest no stratigraphic link between the Wrangellia composite terrane and the paleo-Alaskan margin: Lithosphere, v. 5, no. 6, p. 575–594. doi.org/10.1130/L310.1

Huntington, K.W., Ehlers, T.A., Hodges, K.V., and Whipp, D.M., 2007, Topography, exhumation pathway, age uncertainties, and the interpretation of thermochronometer data: Tectonics, v. 26, no. 4.

Ivanhoe, L.F., 1962, Right-lateral strike-slip movement along the Lake Clark fault, Alaska: Geological Society of America Bulletin, v.73, p. 911–912, 1 sheet.

Jadamec, M.A., and Billen, M.I., 2010, Reconciling surface plate motions with rapid three-dimensional mantle flow around a slab edge: Nature, v. 465, no. 7296, p. 338–341.

Jadamec, M.A., Billen, M.I., and Roeske, S.M., 2013, Three-dimensional numerical models of flat slab subduction and the Denali fault driving deformation in south-central Alaska: Earth and Planetary Science Letters, v. 376, p. 29–42.

Jicha, B.R., Scholl, D.W., Singer, B.S., Yogodzinski, G.M., and Kay, S.M., 2006, Revised age of Aleutian Island Arc formation implies high rate of magma production: Geology, v. 34, no. 8, p. 661–664.

Johnston, S.T., 2001, The Great Alaskan Terrane Wreck: reconciliation of paleomagnetic and geological data in the northern Cordillera: Earth and Planetary Science Letters, v. 193, no. 3–4, p.259–272.

Johnson, S.Y., 1985, Eocene strike-slip faulting and nonmarine basin formation in Washington: *in* Biddle, K.T., and Christie-Blick, N., eds., 1985, Strike-slip Deformation, Basin Formation, and Sedimentation, Society of Sedimentary Geology Special Publication 37, p. 283–302.

Jones, J.V. III, Box, S.E., and Bradley, D.C., 2013, Cretaceous to Paleogene tectonic evolution of the western Alaska Range: new insights from shrimp U-Pb geochronology: Geological Society of America Abstracts with Programs, v. 48, no. 7, Geological Society of America Annual Meeting, Denver, CO, Oct. 27–30.

Jones, J.V., III, Todd, Erin, Box, S.E., Haeussler, P.J., Holm-Denoma, C.S., Karl, S.M., Graham, G.E., Bradley, D.C., Kylander-Clark, A.R.C., Friedman, R.M., and Layer, P.W., 2020, Cretaceous to Oligocene magmatic and tectonic evolution of the western Alaska Range: Insights from U-Pb and $^{40}Ar/^{39}Ar$ geochronology: Geosphere, v. 17, 36 p. doi.org/10.1130/GES02303.1

Kay, R.W., and Kay, S.M., 1993, Delamination and delamination magmatism: Tectonophysics, v. 219, no. 1-3, p.177–189.

Kirschner, C.E., and Lyon, C.A., 1973, Stratigraphic and tectonic development of Cook Inlet petroleum province, *in* Pitcher, M. G., ed., Arctic geology: American Association of Petroleum Geologists Memoir 19, p. 396–407.

Koehler, R.D., and Reger, R.D., 2011, Reconnaissance evaluation of the Lake Clark fault, Tyonek area, Alaska: Alaska Division of Geological & Geophysical Surveys Preliminary Interpretive Report 2011-1, 8 p. doi.org/10.14509/22221

Koehler, R.D., Reger, R.D., and Frohman, R.A., 2012, The Castle Mountain fault, south-central Alaska: New lidar-based observations on the sense of slip: Eos Trans. AGU, Fall Meet. Suppl., Abstract #S53D-2530: Alaska Division of Geological & Geophysical Surveys, 1 p., 1 sheet. doi.org/10.14509/24724

Kortyna, C., Donaghy, E., Trop, J.M., and Idleman, B., 2013, Provenance signature of a forearc basin modified by spreading ridge subduction: detrital zircon geochronology and detrital modes from the Paleogene Arkose Ridge Formation, southern Alaska: Basin Research, v. 25, p. 1–25. doi.org/10.1111/bre.12033

Kryza, R., Crowley, Q.G., Larionov, A., Pin, C., Oberc-Dziedzic, T., and Mochnacka, K., 2012, Chemical abrasion applied to SHRIMP zircon geochronology: an example from the Variscan Karkonosze Granite (Sudetes, SW Poland): Gondwana Research, v. 21, no. 4, p.757–767.

Kuiper, K.F., Deino, A., Hilgen, P.J., Krijgsman, W., Renne, P.R., and Wijbrans, J.R., 2008, Synchronizing rock clocks of Earth history: Science, v. 320, p. 500–504.

Lanphere, M.A., and Baadsraard, H., 2001, Precise K-Ar, $^{40}Ar/^{39}Ar$, Rb-Sr and U-Pb mineral ages from the 27.5 Ma Fish Canyon Tuff reference standard: Chemical Geology, v. 175, p. 653–671.

Layer, P.W., Hall, C.M., and York, D., 1987, The derivation of $^{40}Ar/^{39}Ar$ age spectra of single grains of hornblende and biotite by laser step-heating: Geophysical Research Letters, v. 14, no. 7, p. 757–760.

LeBas, M.J., Le Maitre, R.W., and Streckeisen, A., 1986, A chemical classification of volcanic rocks based on the total alkali-silica diagram: Journal of Petrology, v. 27, no. 3, p. 745–750.

LePain, D.L., Stanley, R.G., Helmold, K.P., and Shellenbaum, D.P., 2013, Geologic framework and petroleum systems of Cook Inlet Basin, South-Central Alaska, *in* Stone, D.M., and Hite, D.M., eds., Oil and gas fields of the Cook Inlet Basin, Alaska: American Association of Petroleum Geologists Memoir 104, p. 37–116.

Link, M.H., and Osborne, R.H., 1982, Sedimentary facies of Ridge Basin, southern California, *in* Crowell, J.C., and Link, M.H., eds., 1982, Geologic history of Ridge Basin, southern California: Pacific Section, Society of Economic Paleontologists and Mineralogists, p. 99–104.

Lipman, P.W., Prostka, H.J., and Christiansen, R.L., 1971, Evolving subduction zones in the western United States, as interpreted from igneous rocks: Science, v. 174, no. 4011, p. 821–825.

Little, T.A., 1990, Kinematics of wrench and divergent-wrench deformation along a central part of the Border Ranges Fault System, Northern Chugach Mountains, Alaska: Tectonics, v. 9, no. 4, p. 585–611.

———1992, Development of wrench folds along the Border Ranges fault system, southern Alaska, U.S.A.: Journal of Structural Geology, v. 14, no. 3, p. 343–359.

Little, T.A., and Naeser, C.W., 1989, Tertiary tectonics of the Border Ranges fault system: Chugach Mountains, Alaska: Deformation and uplift in a forearc setting: Journal of Geophysical Research, v. 94, p. 4,333–4,359.

Lonsdale, P., 1988, Paleogene history of the Kula plate: Offshore evidence and onshore implications: Geological Society of America Bulletin, v. 100, p. 733–754.

Lovera, O.M., Grove, Marty, Harrison, T.M., and Mahon, K.I., 1997, Systematic analysis of K-feldspar $^{40}Ar/^{39}Ar$ step heating results: I. Significance of activation energy determinations: Geochimica et Cosmochimica Acta, v. 61, no. 15, p. 3,171–3,192.

Lovera, O.M., Harrison, T.M., and Heizler, M.T., 1993, Argon diffusion domains in K-feldspar II: Kinetic properties of MH-10: Contributions to Mineralogy and Petrology, v. 113, p. 381–393.

Lovera, O.M., Richter, F.M., and Harrison, T.M., 1989, The $^{40}Ar/^{39}Ar$ themochronometry for slowly cooled samples having a distribution of diffusion domain sizes: Journal of Geophysical Research, v. 94, p. 17,917–17,935.

———1991, Diffusion domains determined by 39Ar released during step heating: Journal of Geophysical Research: Solid Earth, v. 96, no. B2, p. 2,057–2,069.

Magoon, L.B., Adkison, W.L., and Egbert, R.M., 1976, Map showing geology, wildcat wells, Tertiary plant fossil localities, K-Ar age dates, and petroleum operations, Cook Inlet area, Alaska: U.S. Geological Survey Miscellaneous Investigations Series, Map I-1019, scale 1:250,000, 3 sheets.

Magoon, L.B., and Claypool, G.E., 1981, Petroleum geology of Cook Inlet Basin—an exploration model: American Association of Petroleum Geologists Bulletin, v. 65, p. 1,043–1,061.

Magoon, L.B., Griesbach, F.B., and Egbert, R.M., 1980, Nonmarine Upper Cretaceous rocks, Cook Inlet, Alaska: American Association of Petroleum Geologists Bulletin, v. 64, no. 8, p. 1,259–1,266.

Malinverno, Alberto, Quigley, K.W., Staro, A. and Dyment, J., 2020, A Late Cretaceous-Eocene geomagnetic polarity timescale (MQSD20) that steadies spreading rates on multiple mid-ocean ridge flanks: Journal of Geophysical Research, v. 125, no. 8. doi.org/10.1029/2020JB020034

McDougall, Ian, and Harrison, T.M., 1999, Geochronology and thermochronology by the $^{40}Ar/^{39}Ar$ method, 2nd edition: New York, Oxford University Press, 269 p.

Miall, A.D., 1978, Tectonic setting and syndepositional deformation of Molasse and other nonmarine-paralic sedimentary basins, Canadian Journal of Earth Sciences, v. 15, p. 1,613–1,632.

———2016, Stratigraphy: A modern synthesis: Switzerland, Springer International Publishing, 463 p. doi.org/10.1007/978-3-319-24304-7

Miller, M.L., Bradley, D.C., Bundtzen, T.K., and McClelland, W., 2002, Late Cretaceous through Cenozoic strike-slip tectonics of southwestern Alaska: The Journal of Geology, v. 110, no. 3, p. 247–270.

Miller, J.S., Matzel, J.E.P., Miller, C.F., Burgess, S.D., and Miller, R.B., 2007, Zircon growth and recycling during the assembly of large, composite arc plutons: Journal of Volcanology and Geothermal Research, v. 167, p. 282–299.

Moll-Stalcup, E.J., 1994, Latest Cretaceous and Cenozoic magmatism in mainland Alaska, *in* Plafker, George, and Berg, H.C., eds., The Geology of Alaska: Geological Society of America, p. 589–618.

Mongrain, J.R., 2012, Depositional systems, paleoclimate, and provenance of the late Miocene to Pliocene Beluga and Sterling Formations, Cook Inlet forearc basin, Alaska: Ph.D. thesis University of Alaska Fairbanks, 101 p.

Moore, M.A., and England, P.C., 2001, On the inference of denudation rates from cooling ages of minerals: Earth and Planetary Science Letters, v. 185, no. 3-4, p. 265–284.

Murphy, M.A., Yin, An, Kapp, P., Harrison, T.M., Manning, C.E., Rhyerson, F.J., Lin, Ding, and Jinghui, Guo, 2002, Structural evolution of the Gurla Mandhata detachment system, southwest Tibet: Implications for eastward extent of the Karakoram system: Geological Society of America Bulletin, v. 114, no. 4, p. 428–447.

Nokleberg, W.J., Jones, D.L., and Silberling, N.J., 1985, Origin and tectonic evolution of the Maclaren and Wrangellia terranes, eastern Alaska Range, Alaska: Geological Society of America Bulletin, v. 96, no. 10, p. 1251–1270. doi.org/10.1130/0016-7606(1985)96<1251:OATEO T>2.0.CO;2

O'Sullivan, P.B., and Wallace, W.K., 2002, Out-of-sequence, basement-involved structures in the Sadlerochit Mountains region of the Arctic National Wildlife Refuge, Alaska: Evidence and implications from fission-track thermochronology: Geological Society of America Bulletin, v. 114 no. 11, p. 1,356–1,378. doi.org/10.1130/0016-7606(2002)114<1356:OOSBIS>2.0.CO;2

Oswald, Peter, 2006, Eocene volcanic rocks of the southern Talkeetna Mountains, Alaska—Anomalous forearc volcanism in an extensional setting: M.Sc. thesis, University of Idaho, Moscow, 40 p.

Paces, J.B., and Miller, J.D., 1993, Precise U-Pb ages of Duluth Complex and related mafic intrusions, northeastern Minnesota: Geochronological insights to physical, petrogenic, paleomagnetic, and tectonomagmatic processes associated with the 1.1 Ga Midcontinent Rift System: Journal of Geophysical Research, v. 98, no. B8, p. 13,997–14,013.

Patton, W.W. Jr, and Tailleur, I.L., 1977, Evidence in the Bering Strait region for differential movement between North America and Eurasia: Geological Society of America Bulletin, v. 88, no. 9, p. 1,298–1,304.

Pavlis, T.L., 1982, Origin and age of the Border Ranges fault of southern Alaska and its bearing on the late Mesozoic tectonic evolution of Alaska, Tectonics, v. 1, p. 343–368.

Pavlis, T.L., and Roeske, S.M., 2007, The Border Ranges fault system, southern Alaska, *in* Ridgway, K.D., Trop, J.M., Glen, J.M.G., and O'Neill, J.M., eds., Tectonic growth of a collisional continental margin: Crustal evolution of southern Alaska: Geological Society of America Special Paper 431, p. 95–127.

Pearce, J.A., Harris, N.B., and Tindle, A.G., 1984, Trace element discrimination diagrams for the tectonic interpretation of granitic rocks: Journal of Petrology, v. 25, no. 4, p. 956–983.

Peccerillo, A., and Taylor, S.R., 1976, Geochemistry of Eocene calc-alkaline volcanic rocks from the Kastamonu area, northern Turkey: Contributions to Mineralogy and Petrology, v. 58, no. 1, p. 63–81.

Pe-Piper, Georgia, Piper, D.J., Koukouvelas, I., Dolansky, L.M., and Kokkalas, S., 2009, Postorogenic shoshonitic rocks and their origin by melting underplated basalts: The Miocene of Limnos, Greece: Geological Society of America Bulletin, v. 121, no. 1–2, p. 39–54.

Piwinskii, A.J., 1968, Experimental studies of igneous rock series central Sierra Nevada batholith, California: The Journal of Geology, v. 76, no. 5, p. 548–570.

Plafker, George, Detterman, R.L., and Hudson, Travis, 1975, New data on the displacement history of the Lake Clark fault: U. S. Geological Survey Circular 722, *in* M.E. Yount, ed., p. 44–45.

Pullen, Alex, Ibáñez-Mejía, Mauricio, Gehrels, G.E., Ibáñez-Mejía, J.C., and Pecha, Mark, 2014, What happens when n=1000? Creating large-n geochronological datasets with LA-ICP-MS for geologic investigations: Journal of Analytical Atomic Spectrometry, v. 29, no. 6, p. 971–980.

Quidelleur, Xavier, Grove, Marty, Lovera, O.M., Harrison, T.M., Yin, An, and Ryerson, F.J., 1997, The thermal evolution and slip history of the Renbu Zedong Thrust, southeastern Tibet: Journal of Geophysical Research, v. 102, p. 2,659–2,679.

Rawlinson, S.E, 1984, Environments of deposition, paleocurrents, and provenance of Tertiary deposits along Kachemak Bay, Kenai Peninsula, Alaska: Sedimentary Geology, v. 38, p. 421–442.

Redfield, T.F., Scholl, D.W., Fitzgerald, P.G. and Beck, M.E. Jr., 2007, Escape tectonics and the extrusion of Alaska: Past, present, and future: Geology, v. 35, no. 11, p. 1,039–1,042.

Reed, B.L., and Lanphere, M.A., 1969, Age and chemistry of Mesozoic and Tertiary plutonic rocks in south-central Alaska: Geological Society of America Bulletin, v. 80, no. 1, p. 23–44.

———1972, Generalized geologic map of the Alaska-Aleutian Range batholith showing potassium-argon ages of the plutonic rocks: U.S. Geological Survey Miscellaneous Field Studies Map 372, 2 sheets.

———1973, Alaska-Aleutian Range batholith: Geochronology, chemistry, and relation to circum-Pacific Plutonism: Geological Society of America Bulletin, v. 84, p. 2,583–2,610.

Reger, R.D., 2009, Reinterpretation of the Kaloa deposits near Granite Point, northwestern Cook Inlet, Alaska: Alaska Division of Geological & Geophysical Surveys Preliminary Interpretive Report 2009-2, 8 p. doi.org/10.14509/18241

Reiners, P.W., and Brandon, M.T., 2006, Using thermochronology to understand orogenic erosion: Annu. Rev. Earth Planet. Sci., v. 34, p. 419–466.

Reinink-Smith, L.M., and Leopold, E.B., 2005, Warm climate in the late Miocene of the south coast of Alaska and the occurrence of Podocarpaceae pollen: Palynology, v. 29, no. 1, p. 205–262.

Renne, P.R., Deino, A.L., Walter, R.C., Turrin, B.D., Swisher, C.C., Becker, T.A., Curtis, G.H., Sharp, W.D., and Jaouni, A.R., 1994, Intercalibration of astronomical and radioisotopic time: Geology, v. 22, no. 9, p. 783–786. doi.org/10.1130/0091-7613(1994)022<0783:IOAART>2.3.CO;2

Renne, P.R., Mundil, Roland, Balco, Greg, Min, Kyoungwon, and Ludwig, K.R., 2010, Joint determination of 40K decay constants and $^{40}Ar/^{40}K$ for the Fish Canyon sanidine standard, and improved accuracy for $^{40}Ar/^{39}Ar$ geochronology: Geochimica et Cosmochimica Acta, v. 74, no. 18, p. 5,349–5,367.

Renne, P.R., Swisher, C.C., Deino, A.L., Karner, D.B., Owens, T.L., and DePaolo, D.J., 1998, Intercalibration of standards, absolute ages and uncertainties in $^{40}Ar/^{39}Ar$ dating: Chemical Geology, v. 45, p. 117–152.

Riccio, S.J., Fitzgerald, P.G., Benowitz, J.A., and Roeske, S.M., 2014, The role of thrust faulting in the formation of the eastern Alaska Range: Thermochronological constraints from the Susitna Glacier thrust fault region of the intracontinental strike-slip Denali fault system: Tectonics, v. 3, no. 11, p. 2,195–2,217. doi.org/10.1002/2014T C003646

Ridgway, K.D., Trop, J.M., and Finzel, E.S., 2012, Modification of continental forearc basins by flat-slab subduction processes: a case study from southern Alaska, *in* Busby, B., and Azor, A., eds., Tectonics of Sedimentary Basins: Recent Advances, First Edition: Blackwell Publishing Ltd., p. 327–346.

Ridgway, K.D., Trop, J.M., Nokleberg, W., and Davidson, C.M., 2002, Mesozoic and Cenozoic tectonics of the eastern and central Alaska Range: Progressive basin development and deformation in a suture zone: Geological Society of America Bulletin, v. 12, p. 1,480–1,504.

Ridgway, K.D., Trop, J.M., and Sweet, A.R., 1997, Thrust-top basin formation along a suture zone, Cantwell basin, Alaska Range: Implications for development of the Denali fault system: Geological Society of America Bulletin, v. 109, p. doi.org/10.1130/0016-7606(1997)109%3C0505:TTBFAA%3E2.3.CO;2

Roden, M.K., Parrish, R.R., and Miller, D.S., 1990, The absolute age of the Eifelian Tioga ash bed: Journal of Geology, v. 98, p. 282–285.

Roeske, S.M., Snee, L.W., and Pavlis, T.L., 2003, Dextral-slip reactivation of an arc-forearc boundary during Late Cretaceous-Early Eocene oblique convergence in the northern Cordillera, *in* Sisson, V.B., Roeske, S.M., and Pavlis, T.L., eds., Geology of a transpressional orogeny developed during ridge-trench interaction along the North Pacific margin: Geological Society of America Special Paper 371.

Rosenthal, J.L., Betka, P.M., Nadin, E.S., Gillis, R.J., and Benowitz, J.A., 2017, Vein formation during progressive Paleogene faulting and folding within the lower Cook Inlet basin, Alaska: Geosphere, v. 14, no. 1, p. 23–49. doi.org/10.1130/GES01435.1

Rowley, D.B. and Lottes, A.L., 1988, Plate-kinematic reconstructions of the North Atlantic and Arctic: Late Jurassic to present: Tectonophysics, v. 155, no. 1–4, p. 73–120.

Saltus, R.W., Stanley, R.G., Haeussler, P.J., Jones, J.V. III, Potter, C.J., and Lewis, K.A., 2016, Late Oligocene to present contractional structure in and around the Susitna basin, Alaska—Geophysical evidence and geological implications: Geosphere, v. 12, no. 5, p. 1,378–1,390.

Samson, S.D., and Alexander, E.C., 1987, Calibration of the interlaboratory $^{40}Ar/^{39}Ar$ dating standard, MMhb-1: Chemical Geology, Isotope Geoscience Section, v. 66, n. 1-2, p. 27–34.

Savitzky, Abraham, and Golay, M.J., 1964, Smoothing and differentiation of data by simplified least squares procedures: Analytical Chemistry, v. 36, no. 8, p. 1,627–1,639.

Schmoll, H.R., and Yehle, L.A., 1987, Surficial geologic map of the northwestern quarter of the Tyonek A-4 Quadrangle, south-central Alaska: U.S. Geological Survey Miscellaneous Field Studies Map 1934, 1 sheet, scale 1:31,680.

Schmoll, H.R., Yehle, L.A., Gardner, C.A., and Odum, J.K., 1984, Guide to surficial geology and glacial stratigraphy in the upper Cook Inlet basin: Anchorage: Alaska Geological Society guidebook, 89 p.

Schoene, Blair, 2014, U-Th-Pb geochronology, *in* Rudnick, R.L., ed., Treatise on Geochemistry (second edition), Volume 4: The Crust: Oxford, UK, Elsevier, p. 341–378. doi.org/10.1016/B978-0-08-095975-7.00310-7

Shah, A.K., Phillips, J.D., Lewis, K.A., Stanley, R.G., Haeussler, P.J., and Potter, C.J., 2020, Three-dimensional shape and structure of the Susitna basin, south-central Alaska, from geophysical data, Geosphere, v. 16.

Sharman, G.R., and Malkowski, M.A., 2020, Needles in a haystack: Detrital zircon UPb ages and the maximum depositional age of modern global sediment: Earth-Science Reviews, v. 203, article 103109.

Shellenbaum, D.P., Gregersen, L.S., and Delaney, P.R., 2010, Top Mesozoic unconformity depth map of the Cook Inlet basin, Alaska: Alaska Division of Geological & Geophysical Surveys Report of Investigation 2010-2, 1 sheet, scale 1:500,000. doi.org/10.14509/21961

Shew, Nora, and Lanphere, M.A., 1992, Map showing potassium-argon ages from the Mount Katmai and adjacent parts of the Naknek and Afognak quadrangles, Alaska Peninsula, Alaska: U.S. Geological Survey Miscellaneous Field Studies Map 2021-E, 1 sheet, scale 1:250,000.

Siegel, Coralie, Bryan, S.E., Allen, C.M., and Gust, D.A., 2018, Use and abuse of zircon-based thermometers: A critical review and a recommended approach to identify antecrystic zircons: Earth-Science Reviews, v. 176, p. 87–116.

Silberman, M.L., and Grantz, A., 1984, Paleogene volcanic rocks of the Matanuska Valley area and the displacement history of the Castle Mountain fault, *in* Conrad, W.L., and Elliott, R.L., eds., The United States Geological Survey in Alaska; accomplishments during 1981: U.S. Geological Survey Circular 868, p. 82–85.

Smith, G.A., and Lowe, D.R., 1991, Lahars: Volcano Hydrologic-Events and Deposition in the Debris Flow—Hyperconcentrated Flow Continuum: Society for Sedimentary Geology Special Publication 45.

Spencer, C.J., Kirkland, C.L., and Taylor, R.J., 2016, Strategies towards statistically robust interpretations of in situ U–Pb zircon geochronology: Geoscience Frontiers, v. 7, no. 4, p. 581–589.

Stanley, R.G., Haeussler, P.J., Benowitz, J.A., Goodman, D.K., Ravn, R.L., Shellenbaum, D.P., Saltus, R.W., Lewis, K.A., and Potter, C.J., 2013, New stratigraphic revelations in the subsurface Susitna basin, south-central Alaska, from geochronology and biostratigraphy [poster]: Geological Society of America Cordilleran Section Meeting, Fresno, CA, May 22, 2013: Alaska Division of Geological & Geophysical Surveys, 1 sheet. doi.org/10.14509/26887

Stanley, R.G., Haeussler, P.J., Benowitz, J.A., Lewis, K.A., Shellenbaum, D.P., Saltus, R.W., Shah, A.K., Phillips, J.D., and Potter, C.J., 2014, Tectonic implications of new geological and geophysical results from the Susitna basin, south-central Alaska: Geological Society of America Abstracts and Programs, Cordilleran Section Annual Meeting, Bakersfield, CA.

Stanley, R.G., Pierce, B.S., and Houseknecht, D.W., 2011, U.S. Geological Survey 2011 assessment of undiscovered oil and gas resources of the Cook Inlet region, south-central Alaska: U.S. Geological Survey Open-File Report 2011-1137, 37 p. pubs.usgs.gov/of/2011/1237/

Stockli, D.F., Dumitru, T.A., McWilliams, M.O. and Farley, K.A., 2003, Cenozoic tectonic evolution of the White Mountains, California and Nevada: Geological Society of America Bulletin, v. 115, no. 7, p. 788–816.

Sunderlin, David, Trop, J.M., Idleman, B.D., Brannick, Alexandria, White, J.G., and Grande, Lance, 2014, Paleoenvironment and paleoecology of a late Paleocene high-latitude terrestrial succession, Arkose Ridge Formation at Box Canyon, southern Talkeetna Mountains, Alaska: Palaeogeography, Palaeoclimatology, Palaeoecology, v. 401, p. 57–80.

Swenson, R.F., 2001, Introduction to Tertiary tectonics and sedimentation in the Cook Inlet basin, *in* Dallegge, T.A., comp., 2003, 2001 Guide to the Petroleum Geology and Shallow Gas Potential of the Kenai Peninsula, Alaska—A Field Trip Guidebook: Alaska Division of Geological & Geophysical Surveys Miscellaneous Publication 128, p. 10–19.

Tchalenko, J.S., 1970, Similarities between shear zones of different magnitudes: Geological Society of America Bulletin, 81, no.6, p. 1,625–1,640.

Terhune, P.J., Benowitz, J.A., Trop, J.M, O'Sullivan, Paul, Gillis, R.J., and Freymueller, J.T., 2019, Cenozoic tectono-thermal history of the southern Talkeetna Mountains, Alaska: Multiple topographic development drivers through time: Geosphere, v. 15, no. 5, p. 1,539–1,576.

Thorkelson, D.J., 1996, Subduction of diverging plates and the principles of slab window formation: Tectonophysics, v. 255, p. 47–63.

Till, A.B., Roeske, S.M., Bradley, D.C., Friedman, Richard, and Layer, P.W., 2007, Early Tertiary transtension-related deformation and magmatism along the Tintina fault system: Alaska, Geological Society of America Special Paper 434, p. 233–264.

Todd, Erin, and Jones, J.V., 2017, Distinct magmatic stages associated with cretaceous through Paleogene crustal formation and evolution of the southern Alaska margin: Geological Society of America Abstracts with Programs, Vol. 49, No. 6, Geological Society of America Annual Meeting, Seattle, WA, Oct. 22–25. doi.org/10.1130/abs/2017AM-304280

Todd, Erin, Jones, J.V. III, Karl, S., Ayuso, R.A., Bradley, D.C., Box, S.E., and Haeussler, P.J., 2014, Magmatic responses to Late Cretaceous through Oligocene tectonic evolution of the western Alaska Range: American Geophysical Union Annual Meeting Abstracts, V32B-06, San Francisco, CA Dec. 15–19.

Todd, Erin, Jones, J.V. III, and Kylander-Clark, A., 2016, Zircon ages and compositions constrain changes in melt sources during and after progressive accretion of the Wrangellia composite terrane to the southern Alaska margin: Geological Society of America Abstracts with Programs, v. 48, no. 7, Geological Society of America Annual Meeting, Denver, CO, Sept. 25–28.

Triplehorn, D.M., Turner, D.L., and Naeser, C.W., 1977, K-Ar and fission-track dating of ash partings in coal beds from the Kenai Peninsula, Alaska: A revised age for the Homerian stage–Clamgulchian stage boundary, Geological Society of America Bulletin, v. 88, p. 1,156–1,160.

———1984, Radiometric age of the Chickaloon Formation of south-central Alaska: Location of the Paleocene-Eocene boundary: Geological Society of America Bulletin, v. 95, no. 6, p. 740–742.

Trop, J.M., 2008, Latest Cretaceous forearc basin development along an accretionary convergent margin: south-central Alaska: Geological Society of America Bulletin, v. 120, p. 207–224. doi.org/10.1130/B26215.1

Trop, J.M., and Ridgway, K.D., 1999, Sedimentology and provenance of the Paleocene–Eocene Arkose Ridge Formation, Cook Inlet–Matanuska Valley forearc basin, southern Alaska, *in* Pinney, D.S., and Davis, P.K., eds., Short Notes on Alaska Geology 1999: Alaska Division of Geological & Geophysical Surveys Professional Report, v. 119, p. 129–144.

———2007, Mesozoic and Cenozoic tectonic growth of southern Alaska: a sedimentary basin perspective, *in* Ridgway, K.D., Trop, J.M., Glen, J.M.G., and O'Neill, J.M., eds., Tectonic Growth of a Collisional Continental Margin: Crustal Evolution of Southern Alaska: Geological Society of America, Special Paper 431, p. 55–94.

Trop, J.M., Ridgway, K.D., and Spell, T.L., 2003, Sedimentary record of transpressional tectonics and ridge subduction in the Tertiary Matanuska Valley–Talkeetna Mountains forearc basin, southern Alaska, *in* Sisson, V.B., Roeske, S.M., and Pavlis, T.L., eds., Geology of a transpressional orogen developed during ridge-trench interaction along the north Pacific margin: Geological Society of America, Special Paper 371, p. 89–118.

Trop, J.M., Szuch, D.A., Rioux, M., and Blodgett, R.B., 2005, Sedimentology and provenance of the Upper Jurassic Naknek Formation, Talkeetna Mountains, Alaska: Bearings on the accretionary tectonic history of the Wrangellia composite terrane: Geological Society of America Bulletin, v. 117, p. 570–588.

Turner, D.L., Triplehorn, D.M., Naeser, C.W., and Wolfe, J.A., 1980, Radiometric dating of ash partings in Alaskan coal beds and upper Tertiary paleobotanical stages: Geology, v. 8, p. 92–96.

Turner, R.F., 1986, Paleontology and biostratigraphy of the COST No. 1 well, *in* Magoon, L.B., ed., Geologic studies of the lower Cook Inlet COST No. 1 well, Alaska outer continental shelf: U.S. Geological Survey Bulletin 1596, p. 29–31.

Vermeesch, Pieter, 2004, How many grains are needed for a provenance study?: Earth and Planetary Science Letters, v. 224, no. 3–4, p. 441–451.

Vermeesch, Pieter, 2018, IsoplotR: a free and open toolbox for geochronology: Geoscience Frontiers, v. 9, p. 1,479–1,493. doi.org/10.1016/j.gsf.2018.04.001

Wallace, W.K., Hanks, C.L., and Rogers, J.F., 1989, The southern Kahiltna terrane: Implications for the tectonic evolution of southwestern Alaska: Geological Society of America Bulletin, v. 101, no. 11, p. 1,389–1,407.

Walsh, J.J., and Watterson, Juan, 1991, Geometric and kinematic coherence and scale effects in normal fault systems: Geological of Society, London, Special Publications, v. 56, no. 1, p. 193–203.

Wartes, M.A., Helmold, K.P., Gillis, R.J., LePain, D.L., Herriott, T.M., Stanley, R.G., Finzel, E.S., and Jones, J.V., 2015, Secular changes in Cenozoic arc magmatism and its influence on forearc basin sandstone composition and reservoir quality in Cook Inlet, southern Alaska: Geological Society of America Cordilleran Section Meeting, Anchorage, Alaska, May 11–13.

Wartes, M.A., Herriott, T.M., Decker, P.L., Stanley, R.G., Gillis, R.J., and Helmold, K.P., 2014, Enigmatic Late Cretaceous tectonic subsidence of the Cook Inlet forearc basin during major subduction accretion, southern Alaska: Geological Society of America Abstracts with Programs. v. 46, no. 6, p. 375, Geological society of America Annual Meeting, Vancouver, BC, October 19–22.

Weidenbeck, M., Alle, P., Corfu, F., Griffin, W.L., Meier, M., Oberli, F., Vonquandt, A., Roddick, J.C., and Speigel, W., 1995, Three natural zircon standards for U-Th-Pb, Lu-Hf, trace-element and REE analyses: Geostandards Newsletter, v. 19, p. 1–23.

Whalen, J.B., Currie, K.L., and Chappell, B.W., 1987, A-type granites: geochemical characteristics, discrimination and petrogenesis: Contributions to Mineralogy and Petrology, v. 95, no. 4, p. 407–419. doi.org/10.1007/BF00402202

Whittington, A.G., 1996. Exhumation overrated at Nanga Parbat, northern Pakistan: Tectonophysics, v. 260, no. 1–3, p. 215–226.

Willis, J.B., Haeussler, P.H., Bruhn, R.L., and Willis, G.C., 2007, Holocene Slip Rate for the Western Segment of the Castle Mountain Fault, Alaska: Bulletin of the Seismological Society of America, v. 97, no. 3, p. 1,019–1,024. doi.org/10.1785/0120060109

Wilson, F.H., Hults, C.P., Schmoll, H.R., Haeussler, P.J., Schmidt, J.M., Yehle, L.A., and Labay, K.A., comps., 2012, Geologic map of the Cook Inlet region, Alaska, including parts of the Talkeetna, Talkeetna Mountains, Tyonek, Anchorage, Lake Clark, Kenai, Seward, Iliamna, Seldovia, Mount Katmai, and Afognak 1:250,000-scale quadrangles: U.S. Geological Survey Scientific Investigations Map 3153, 76 p., 2 sheets, scale 1:250,000.

Wilson, M., ed., 1989, Igneous petrogenesis: London, Springer Netherlands, 466 p.

Winkler, G.R., 1992, Geologic map and summary geochronology of the Anchorage 1° × 3° quadrangle, southern Alaska: U.S. Geological Survey Miscellaneous Investigations Series Map I-2283, scale: 1:250,000.

Wolfe, J.A., Hopkins, D.M., and Leopold, E.B., 1966, Tertiary stratigraphy and paleobotany of the Cook Inlet region, Alaska: U.S. Geological Survey Professional Paper 398-A, 29 p., 1 plate.

Wolfe, J.A., and Tanai, Toshimasa, 1980, The Miocene Seldovia Point flora from the Kenai Group, Alaska: U.S. Geological Survey Professional Paper 1105, 52 p., 25 plates.

Woodcock, N.H., 2004, Life span and fate of basins: Geology, v. 32, no. 8, p.685–688.

Xie, Xiangyang, and Heller, P.L., 2009, Plate tectonics and basin subsidence history: Geological Society of America Bulletin, v. 121, no. 1–2, p. 55–64.

Yeats, R.S., 1978, Neogene acceleration of subsidence rates in southern California: Geology, v. 6, no. 8, p. 456–460.

York, Derek, Hall, C.M., Yanase, Yotaro, Hanes, J.A., and Kenyon, W.J., 1981, $^{40}Ar/^{39}Ar$ dating of terrestrial minerals with a continuous laser: Geophysical Research Letters, v. 8, no. 11, p. 1,136–1,138.

Yuan, H.L., Gao, Shan, Dai, M.N., Zong, C.L., Günther, Detlef, Fontaine, G.H., Liu, X.M., and Diwu, ChunRong, 2008, Simultaneous determinations of U-Pb age, Hf isotopes and trace element compositions of zircon by excimer laser-ablation quadrapole and multiple-collector ICP-MS: Chemical Geology, v. 247, p. 100–118.

Ziony, J.I., and Yerkes, R.F., 1985, Evaluating earthquake and surface-faulting potential, *in* Ziony, J.I., ed., Evaluating earthquake hazards in the Los Angeles region: U.S. Geological Survey Professional Paper 1360, p. 43–91.

Zippi, P.A., Gillis, R.J., Montayne, Simone, and Loveland, A.M., 2021, Palynological and thermal maturity analysis of 267 outcrop samples from the Kenai, Seldovia, and Tyonek quadrangles, Cook Inlet region, Alaska: Alaska Division of Geological & Geophysical Surveys Raw Data File 2021-8. doi.org/10.14509/30660

Zippi, P.A., and Loveland, A.M., 2012, Palynological analysis of 228 outcrop samples from the Kenai, Seldovia, and Tyonek quadrangles, Cook Inlet region, Alaska: Alaska Division of Geological & Geophysical Surveys Raw Data File 2012-1, 10 p. doi.org/10.14509/23723